5-14-2024

Development, Numerical Simulation and Turbulence Modeling of a Sustainable Transonic Truss-Braced Wing Aircraft using Liquid Hydrogen Fuel and Active Flow Control

Bryce Zachary Thomas
Washington University – McKelvey School of Engineering

WASHINGTON UNIVERSITY IN ST. LOUIS

McKelvey School of Engineering
Department of Mechanical Engineering and Materials Science

Dissertation Examination Committee:
Ramesh Agarwal, Chair
Rajan Chakrabarty
Mark Jakiela
Swami Karunamoorthy
David Peters
Christian Rice

Development, Numerical Simulation and Turbulence Modeling of a Sustainable Transonic Truss-Braced Wing Aircraft using Liquid Hydrogen Fuel and Active Flow Control

by

Bryce Thomas

A dissertation presented to
the McKelvey School of Engineering
of Washington University in
partial fulfillment of the
requirements for the degree
of Doctor of Philosophy

May 2024
St. Louis, Missouri

Table of Contents

List of Figures

List of Tables

Acknowledgments

I would like to thank Dr. Ramesh Agarwal for his guidance, advice, and encouragement throughout this research. His belief in me is what made this research possible. I am very grateful to him for allowing me to explore and grow my passion for aerodynamics and green aviation.

I would like to thank my committee members for their time and effort in being part of my dissertation.

I would like to thank Christian Rice and Mark Holly (retired from Boeing-St. Louis) for their support, advice, and effort in collaborating with me to improve my understanding of aircraft design.

I would like to thank my colleagues in the CFD lab for the collaboration and support that encouraged my passion for research.

Finally, I would like to thank my family for their support and encouragement that pushed me to pursue my goals and grow both as a student and a person.

I am grateful for the financial support provided by the NASA-Missouri Space Grant.

Bryce Thomas

Washington University in St Louis

May 2024

ABSTRACT OF THE DISSERTATION

Development, Numerical Simulation and Turbulence Modeling of a Sustainable Transonic Truss-Braced Wing Aircraft using Liquid Hydrogen Fuel and Active Flow Control

by

Bryce Thomas

Doctor of Philosophy in Aerospace Engineering

Washington University in St. Louis, 2024

Professor Ramesh Agarwal, Chair

There is pressing need for emissions reduction and an increase in efficiency for the next generation of commercial aircraft in order to reduce the environmental impact of the aviation sector and combat global climate change. The implementation of alternative fuels as well as new engine and wing designs are actively being explored as methods to reduce emissions. This thesis analyzes the implementation of hydrogen fuel, a transonic truss braced wing and active flow controls as means to improve the performance of a medium range commercial airliner. The widespread adoption of cryogenic liquid hydrogen (LH2) fuel as a green alternative to Jet A has the potential to drastically reduce the environmental impact of aviation. Although liquid hydrogen has higher energy density than jet fuel, high volume cryogenic tanks are necessary requiring a reevaluation of traditional aircraft design. A high aspect ratio transonic truss braced wing (TTBW) has inherent aerodynamic benefits, improved lift-to-drag ratio, in comparison to traditional cantilever wings. Active flow controls in the form of co-flow jets (CFJ) are evaluated as a method to further improve the performance of the transonic truss braced wing. Initial design starts with the fuel tank configuration design and drag optimization of external liquid hydrogen fuel tanks using a MATLAB code. A matrix of configurations is considered with varying volume fuel tanks and fuselage designs. The

tradeoff between internal and external fuels tanks is evaluated for efficient hydrogen fuel storage. The aircraft design and analysis tool RDSWin is used to assess aircraft performance in conjunction with aerodynamics, propulsion, and weight estimation methods. The aircraft performance analysis shows the drag reduction of internal tanks in comparison to external stores. The transonic truss braced wing is shown to reduce aircraft fuel burn in comparison to a cantilever wing with similar airfoils. The B767 fuselage with TTBW and internal LH2 tanks is found to have the best potential for a future zero carbon emission liquid hydrogen powered aircraft. Next, the accuracy of numerical methods and turbulence models necessary for further analysis and improvements in aerodynamic performance are examined. Computational fluid dynamics (CFD) is performed using ANSYS Fluent on the NASA juncture flow aircraft model and the ONERA M6 transonic wing model to evaluate the performance of turbulence models in calculating complex flows with separation and shock. This research also analyzes the accuracy of various turbulence models with nonlinear quadratic constitutive relation (QCR) for eddy viscosity in comparison to the linear Boussinesq assumption. The final phase focuses on the integration of the CFJ into a TTBW. Parametric setups are created to sweep through varying angles of attack and jet momentum coefficients. The RAE2822 transonic airfoil is simulated in 2D with and without CFJ in comparison to published data for validation of numerical methods, boundary conditions and grid techniques. The airfoil with and without CFJ is then scaled to the crank chord of the TTBW and simulated at cruise conditions. Large scale 3D simulations are run on the TTBW with and without CFJ to analyze the effect of the truss and active flow controls on aerodynamic performance. It is determined that CFJ can further improve aerodynamic efficiency during cruise for a TTBW.

Chapter 1: Introduction

1.1 Motivation

The increasing concentration of greenhouse gases (GHG) such as carbon dioxide (CO_2) in the troposphere contributes to climate change and increase in warming of the earth that are already having and increasingly will have a multitude of adverse effects on human life and environment. The aviation industry is a significant contributor to CO_2 emissions due to burning of Jet A fuel in the gas turbine engines. Other aviation emissions such as soot, nitrogen oxide and contrail formation also contribute to the climate change [1]. The warming of the Earth's surface will result in ocean's rise resulting in coastal flooding and saltwater intrusion as well as extreme weather events ranging from hurricanes to wildfires that pose a threat to the global ecosystem, human lives and property [2]. In recent decades (1960-2018), CO_2 emissions from the aviation sector grew primarily because of increased passenger demands for travel from 109 to 8269 billion km/year [1]. In order to reduce the environmental impact of the aviation industry, there is need for reduction in emissions and an increase in efficiency for the next generation commercial passenger aircraft. This can be achieved through the use of sustainable fuels, increase in the aerodynamic and propulsive efficiency as well as the structural and material developments to reduce the aircraft weight. This is reflected in the Breguet range equation which is a key equation used in the design of aircraft.

$$Range = \frac{h_f}{g}\frac{L}{D}\eta_{overall}\ln\left(\frac{W_{initial}}{W_{final}}\right) \tag{1.1}$$

According to Eq. (1), the energy density (h_f) of the fuel carried and burned in the propulsion system of the aircraft is the dominant factor in determining the aircraft range. However, increase in aerodynamic efficiency by improvement in lift generation and minimization of drag can also

contribute to greater aircraft range. In addition, the propulsive efficiency can also be improved through reductions in the thrust-specific fuel consumption (TSFC). Lastly the weight of the aircraft has an impact on the efficiency in terms of achievable range for a given fuel load. Many studies into advance composite materials are being conducted to reduce the weight of the aircraft structures. The focus of this study is to develop a single aisle mid-range aircraft using sustainable fuel and improve the aerodynamic efficiency through emerging new wing designs and active flow control technologies.

1.2 Alternative Fuel

Compared to Jet A fuel as the current industry standard which is responsible for carbon and other emissions from a gas turbine engine, alternative fuels such as Sustainable Aviation Fuels (SAF), hydrogen and ammonia have the real potential to reduce the GHG emissions from aviation, especially the net carbon emissions. Although SAF does not directly eliminate the carbon emissions, it indirectly reduces the carbon emissions since it is produced from agriculture crops (non-edible). It is also a drop-in fuel for existing aircraft engines. However, it does not provide long term solution for zero-emission aviation. It can therefore be considered as a transitional fuel before zero emissions goal is achieved. In the meantime, the aviation industry is also exploring the potential and technological challenges of alternative fuels such as liquid hydrogen (LH_2), Ammonia (NH_3) and Ammonia-Borane (BH_3NH_3). This dissertation examines the potential of LH_2. The combustion of hydrogen gas yields an exhaust of water vapor and has heat of combustion of ~ 142 MJ/kg.

$$2H_2(g) + O_2(g) \rightarrow 2H_2O(g) \qquad (1.2)$$

Implementation of liquid hydrogen fuel in an aircraft is ideal from green aviation perspective; however, it poses multiple aircraft design challenges. A comparison of the properties of various types of fuels is shown in Table 1.1.

Table 1.1 Comparison of properties of various fuel types

	Jet A	SAF	Liquid Hydrogen	Ammonia
Density (lbs./ft^3)	~ 48.38-52.44	---	4.432	42.57
Energy Density (Btu/ft^3)	1,009,870.13	---	214,714	48,900
Heat of Combustion (MJ/kg)	42-46	42-46	141.8	22.5
Boiling Point (F)	~ 349	---	- 432.2	- 28.01

It can be noted from Table 1.1 that liquid hydrogen has significantly higher energy density and heat of combustion in comparison to Jet A, SAF and Ammonia. The higher energy density per unit mass is beneficial to the range and efficiency of the aircraft. Figure 1.1 shows the payload and range comparison for the Boeing 737-800 without winglets during long range cruise [3]. It can be noted that for a heavy weight configuration with a maximum take-off gross weight (TOGW) of 174,200 lbs. and an operating empty weight (OEW) of 91,300 lbs. Jet A fuel load of 46,063 lbs. is required to achieve a range of 2840 nmi. Based on the heat of combustion, the 46,063 lbs. of Jet A in B737-800 aircraft can be replaced by 14,293 lbs. of hydrogen or 90,079 lbs. of ammonia. Figure 1.1 shows the payload and range comparison for a B737-800 aircraft [3]

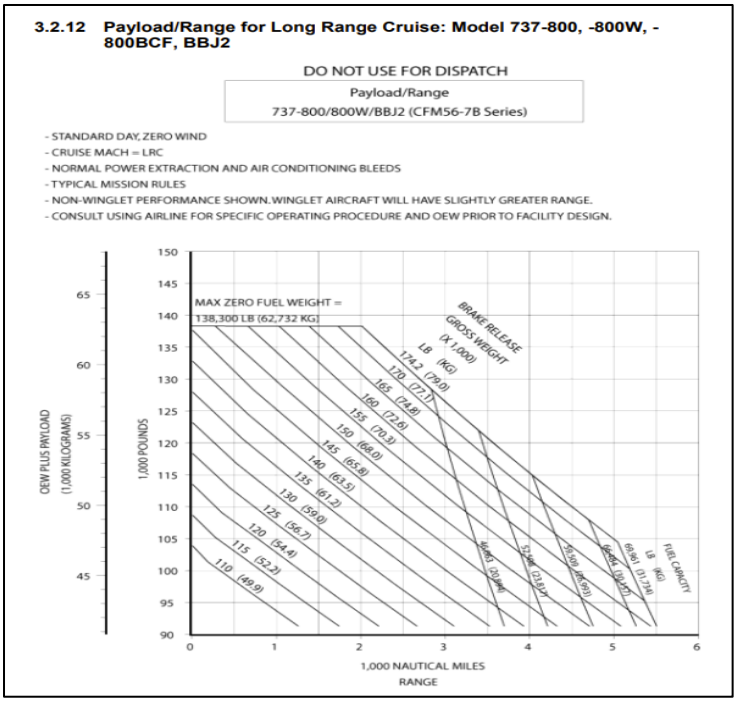

Figure 1.1 Payload and range comparison for a 737-800 aircraft [3]

Liquid hydrogen has nearly four times lower the volumetric energy density in comparison to Jet A. This presents a significant problem for aircraft designers since the standard space in airliner wing boxes for fuel storage is not sufficient to accommodate the volume of liquid hydrogen with equivalent energy to that of traditional Jet A. A variety of solutions are being proposed by various research groups to design aircraft with large cryogenic pressurized hydrogen fuel tanks. For example, the Airbus ZeroE turbofan concept has a liquid hydrogen storage system behind the pressure bulkhead in the rear of the aircraft. The present study investigates the aerodynamic effects of the location of the fuel tank – inside or outside the fuselage. Several configurations are analyzed using internal tanks, external wing mounted tanks, and a combination of the two. External wing mounted tanks increase the overall drag of the vehicle and require design changes for possible wheels up landing conditions.

1.3 Transonic Truss-Braced Wing

The first phase of the Subsonic Ultra-Green Aircraft Research (SUGAR) study began in 2009 in which NASA and Boeing analyzed concepts for aircraft that would fly in the 2030-2035 timeframe [4]. Through phases I and II of the program, the potential of the transonic truss braced (TTBW) wing concept to reduce the fuel consumption was highlighted. The TTBW is a high aspect ratio wing that requires a truss to support the large span. The high wing design is beneficial since it allows for future integration of the efficient large diameter fans and open rotor propulsion systems such as the GE's RISE engine concept. The TTBW was developed to improve the aircraft performance achieving a lift-drag-ratio of ~26. This feature along with the weight reduction in comparison to a cantilever wing reduces the fuel burn. Further studies have been conducted to ensure that the aeroelastic effects of the TTBW are predictable and manageable. Phase III and IV of the programs focused on the analysis of high speed aerodynamics and further development of the wing and truss geometry. Notably, in Phase IV the cruise condition was extended to Mach 0.8 and the truss was decoupled from the wing resulting in improved aerodynamic performance [5]. The unstacking of the wing and the truss reduced the compressibility drag. SUGAR IV has been chosen in this dissertation as the baseline for the development of a sustainable mid-range aircraft using liquid hydrogen. Figure 1.2 shows a planform view comparison of the SUGAR III and IV design concepts.

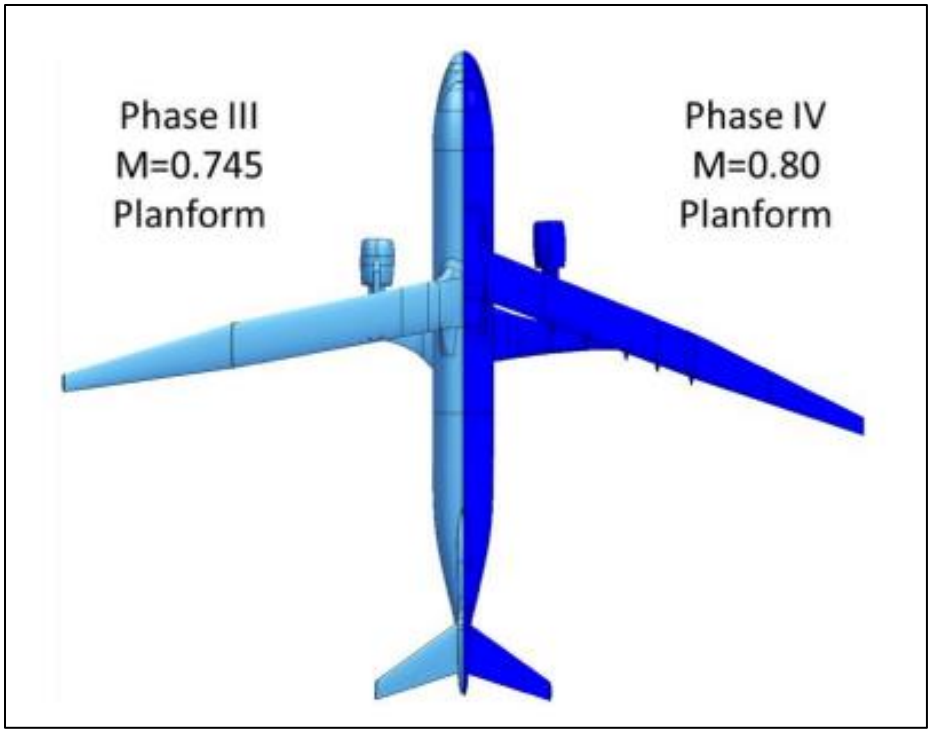

Figure 1.2 Comparison of the SUGAR phase III and IV planforms [5]

1.4 Active Flow Control

Decades of airfoil design in both the military and commercial sectors has produced highly optimized airfoils for a range of flow regimes. Research has largely shifted to development of active-flow control (AFC) to further improve the airfoil performance. A variety of AFC techniques such as circulation-control airfoils, synthetic jets and plasma actuators have been shown to improve the maximum lift coefficient by delaying flow separation [6]. Flow separation can be delayed by energizing the boundary layer allowing it to overcome the adverse pressure gradients. Most active flow control methods are unable to improve the aerodynamic efficiency of supercritical airfoils at transonic cruise conditions at lower angles of attack. Further research into cruise AFC techniques is necessary to improve the aircraft performance over a mid-range mission profile. One potential solution is the co-flow jet (CFJ) airfoil.

The co-flow jet (CFJ) airfoil is a zero-net mass flux active flow control airfoil developed by Zha et al. that has been shown to improve the performance of supercritical airfoils at transonic cruise conditions [7]. The active flow control mechanism is actuated by a micro-compressor pumping system within the airfoil. Air is withdrawn into a suction slot near the trailing edge of the airfoil pressurized by the pump and injected near the leading-edge tangent to the flow direction as shown in Fig. 1.3. The wall boundary-layer is energized by turbulent mixing via large vortex structures between the jet and the main flow. The energized boundary layer increases the circulation and lift and reduces the total drag by filling the wake velocity deficit. The CFJ has been shown to improve the transonic airfoil performance at low angles of attack. This means that unlike many active flow control techniques, CFJ can improve the airfoil performance during cruise condition which is the most important phase of flight to reduce fuel consumption. The CFJ also improves the low speed takeoff and landing performance with the benefit of being a self-contained system without additional flaps. It has been shown to improve the stall margin with flow remaining attached up to angles of attack as high as 70°. The CFJ has the potential to create compact high lift geometries without the weight of complex support structures required for many high lift devices. Although the co-flow jet has been shown to improve airfoil performance in the transonic regime, much of the current research is focused on the development of short-range eV/STOL vehicles. More research is necessary to scale and optimize this active flow control technology to a single isle airliner. The objective is to maximize the lift-to-drag ratio with respect to a limit on the power consumption of the CFJ pump system. The power consumption can be determined by the change in enthalpy and the mass flow rate of the jet as follows [7]:

$$P = \dot{m}(H_{01} - H_{02}) \tag{1.3}$$

where H_{01} and H_{02} are the total enthalpies of the injection and suction slots respectively. This can also be expressed as

$$P = \frac{\dot{m}C_P T_{02}}{\eta}(\Gamma^{\frac{\gamma-1}{\gamma}} - 1) \tag{1.4}$$

where η is the pump efficiency, Γ is the pump total pressure ratio and γ is the specific heat ratio of air. The power coefficient is then normalized as a power coefficient as follows.

$$P_C = \frac{P}{\frac{1}{2}\rho_\infty V_\infty^3 S} \tag{1.5}$$

The power of the active flow controls needs to be limited such that the horsepower extraction is below 15% of the total thrust. This is especially important during the takeoff portion of the flight envelope. Since most commercial aircraft have nacelles straight inlets with blunt tips, a large amount of power can be extracted reducing the risk of reaching the stability margin.

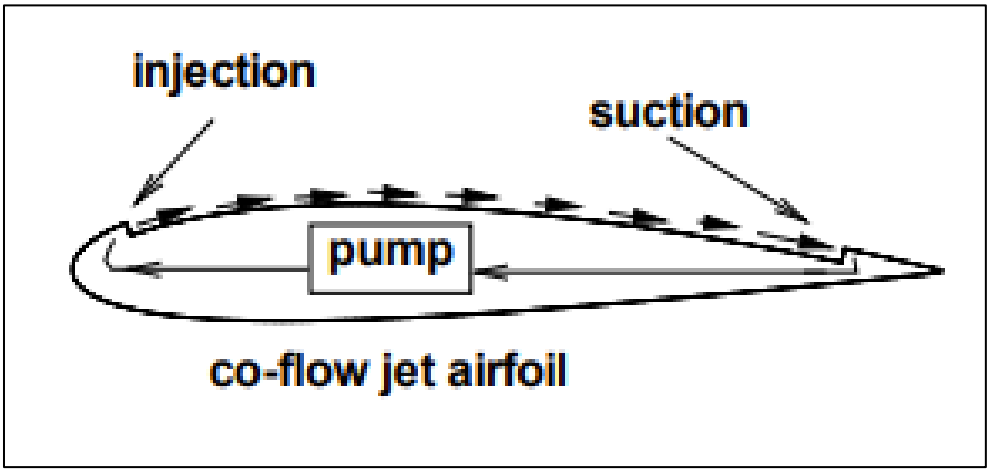

Figure 1.3 Schematic of Co-Flow Jet (CFJ) [7]

A physical wind tunnel model of the CFJ-RAE 2822 is shown in Figure 1.4. The straight wing is divided into spanwise sections each corresponding to a micro compressor as shown in Figure 1.5. A similar technique could be used to implement CFJ into a larger commercial airliner wing; however, the addition of sweep, taper and twist could increase complexity and vary the

effectiveness of the CFJ in comparison to a straight wing. Furthermore, the CFJ slots would have to be designed in consideration with wing structures.

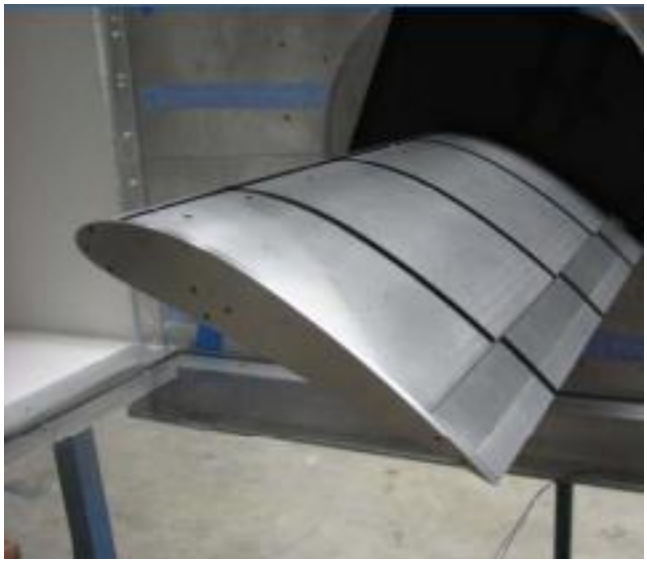

Figure 1.4 CFJ-RAE 2822 wind tunnel model [8]

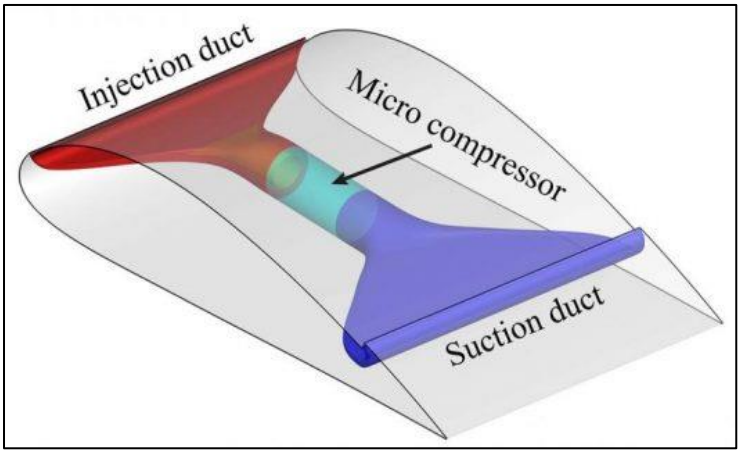

Figure 1.5 CFJ-RAE 2822 internal micro compressor cavity [9]

Chapter 2 Review of Turbulence Models

This chapter describes the various turbulence models and numerical methods used in this research.

2.1 k-ω SST Model

The $k-\omega$ SST (Shear-Stress Transport) model utilizes two transport equations representing the turbulent kinetic energy and the specific dissipation. The $k-\omega$ SST model differs from the baseline (BSL) k-omega model by a modification of the eddy viscosity definition to account for the turbulent shear stress [10]. The transport equations for k and ω in Menter's k-omega shear stress transport model can be written as [10]:

$$\frac{\partial}{\partial t}(\rho k)+\frac{\partial}{\partial x_i}(\rho k u_i)=\frac{\partial}{\partial x_j}\left(\Gamma_k \frac{\partial k}{\partial x_j}\right)+G_k-Y_k+S_k \tag{2.1}$$

$$\frac{\partial}{\partial t}(\rho \omega)+\frac{\partial}{\partial x_i}(\rho \omega u_i)=\frac{\partial}{\partial x_j}\left(\Gamma_\omega \frac{\partial \omega}{\partial x_j}\right)+G_\omega-Y_\omega+D_\omega+S_\omega \tag{2.2}$$

The details of the model can be found in Ref. [10].

2.2 Spalart-Allmaras (SA) Model

The Spalart-Allmaras turbulence model consists of a single transport equation for the turbulent kinematic viscosity. In comparison to commonly used two equation models, the SA model does not calculate the turbulent kinetic energy and therefore does not factor this into the Reynolds stresses [11,12]. The Spalart-Allmaras model has been proven to yield consistent results for boundary layer flows with large pressure gradients; however, it can have difficulties in accurately simulating flows that shift between free shear and wall-bounded-flow due to length scale changes. The equation for turbulent kinematic viscosity υ in Spalart-Allmaras (SA) model can be written as follows [11]. The details of the model can be found in Ref. [10].

$$\frac{\partial}{\partial t}(\rho v) + \frac{\partial}{\partial x_i}(\rho v u_i) = G_v + \frac{1}{\sigma_v}\left[\frac{\partial}{\partial x_j}\left\{(\mu + \rho v)\frac{\partial v}{\partial x_j}\right\} + C_{b2}\rho\left(\frac{\partial v}{\partial x_j}\right)^2\right] - Y_v + S_v \quad (2.3)$$

2.3 Wray-Agarwal (WA) Model

The Wray-Agarwal turbulence model also utilizes a single transport equation derived from k-omega SST closure [13]. A switching function in the equation allows the model to act as either a one equation version of the $k-\omega$ or $k-\varepsilon$ models. The WA turbulence model is applied as a user-defined function (UDF) in ANSYS fluent. The modified wall distance free WA2018 model has shown improved accuracy over the SA model in many flow simulations and has been found to be competitive in accuracy with two-equation k-omega SST model for many flows. The R (= k/ω) equation of the WA2018 model can be written as follows [13]. The details of the model can be found in Ref. [13].

$$\frac{\partial R}{\partial t} + \frac{\partial u_j R}{\partial x_j} = \frac{\partial}{\partial x_j}\left[(\sigma_R R + v)\frac{\partial R}{\partial x_j}\right] + C_1 RS + f_1 C_{2k\omega}\frac{R}{S}\frac{\partial R}{\partial x_j}\frac{\partial S}{\partial x_j} - (1 - f_1)min\left[C_{2k\epsilon}\left(\frac{\frac{\partial S}{\partial x_j}\frac{\partial S}{\partial x_j}}{S^2}\right), C_m\frac{\partial R}{\partial x_j}\frac{\partial R}{\partial x_j}\right] \quad (2.4)$$

2.4 Quadratic Constitutive Relation

The three turbulence models described above employ the linear Boussinesq assumption for modeling the Reynolds stresses in the RANS equations. The Boussinesq assumption states that the Reynolds stress tensor is proportional to the mean strain rate tensor and can be written as:

$$\tau_{ij} = 2\mu_t(S_{ij} - \frac{\partial u_k}{\partial x_k}\delta_{ij}) - \frac{2}{3}\rho\kappa\delta_{ij} \quad (2.5)$$

where μ_t denotes the turbulent eddy viscosity.

The quadratic constitutive relation postulated by Spalart et al. [14] modifies the Bousinesq assumption by introducing a nonlinear relationship between the stress and strain. The QCR2000 modification can be written as:

$$\tau_{ijQCR} = \tau_{ij} - C_{cr1}[O_{ik}\tau_{jk} + O_{jk}\tau_{ik}] \tag{2.6}$$

$$O_{ik} = \frac{2W_{ik}}{\sqrt{\frac{\partial u_m}{\partial x_n}\frac{\partial u_m}{\partial x_n}}} \tag{2.7}$$

$$W_{ik} = \frac{1}{2}\left(\frac{\partial u_i}{\partial x_k} - \frac{\partial u_k}{\partial x_i}\right) \tag{2.8}$$

where O_{ik} is an antisymmetric normalized rotation tensor and $C_{icr1} = 0.3$. Employing Eqs. (2.6-2.8), QCR version of SA, WA and *k*-ω SST was developed and implemented in Fluent using a UDF.

Chapter 3: LH2 Fuel Tank Design Study

The aerodynamic design of the external tanks was done using a MATLAB code to optimize the tank shape for drag reduction. The code finds the minimum of a constrained nonlinear multivariable function; in the present case Hoerner's empirical correlation for the drag coefficient of bodies of revolution is employed [15].

$$C_{DV} = Re^{-\frac{1}{6}} * \left\{ 0.172 * \left(\frac{Length}{Diameter}\right)^{\frac{1}{3}} + 0.252 * \left(\frac{Diameter}{Length}\right)^{\frac{6}{5}} + 1.032 * \left(\frac{Diameter}{Length}\right)^{\frac{27}{10}} \right\} \quad (3.1)$$

A series of variables is used to define the geometry of the tank in a two-dimensional coordinate system. The length, diameter, volume, location of maximum diameter, nose and tail curvature and prismatic coefficient are set as variables with a combination of linear and nonlinear inequality constraints [16]. The leading edge radius is limited in order to mitigate risk of damage due to bird strike by improving probability of a glancing blow. The tanks are optimized for the cruise conditions of an aircraft flying at Mach 0.8 at an altitude of 35,000 ft. The curves generated by the code, shown in Figure 3.1, can then be used as output and included in a CAD package to create the three-dimensional tank geometries to be implemented in RDSWin aircraft design software. Figure 3.1 shows the tank geometries generated by the optimization code for three different fuel loads. The MATLAB code also has a function to account for the addition of internal tanks that could be potentially used in future designs to reduce external tank volume in a hybrid configuration. Figure 3.2 shows the correlation between the external tank volume and the parasite drag. A linear trend is seen in the data points with an increase in drag with higher volume of external fuel tanks. Interference drag between the external tanks and the wing is later accounted for using RDSWin with an assumed interference factor of 1.5. The code is also used to calculate

the weight of the fuel tank structures assuming an aluminum outer skin with a thickness of 0.05 in, inner skin with a thickness of 0.07 in and an EPS insulation layer of 4.5 in thickness. Due to its low boiling point, liquid hydrogen must be maintained in a cryogenic state with sufficient insulation to mitigate boiloff (evaporation) resulting in pressure buildup and eventually damage to the tank structures including the possibility of rupture. Approximately 4.5 inches of EPS foam is sufficient to minimize boiloff in the external hydrogen tanks. The structural weight is calculated from the volume of the materials and their respective densities. Furthermore, the MATLAB code accounts for the weight of longerons and bulkheads within the external fuel tanks. The external tanks pylons are assumed to have 20% weight of the external fuel tank structural weight. Figure 3.3 shows the total external fuel tank weights (fuel, structural weight, and pylons) in relation to the total volume of the tank. A number of tanks with different volumes were tested and three cases were then implemented into RDSwin to evaluate the influence of the tanks on aircraft performance. The fuel tank properties for the three chosen tanks are shown in Table 3.1.

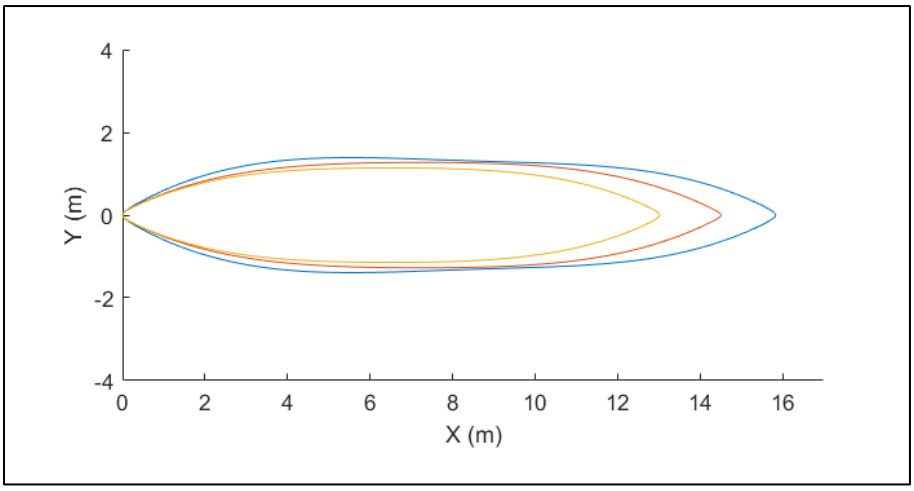

Figure 3.1 External fuel tanks cross-sections generated by the MATLAB optimization code

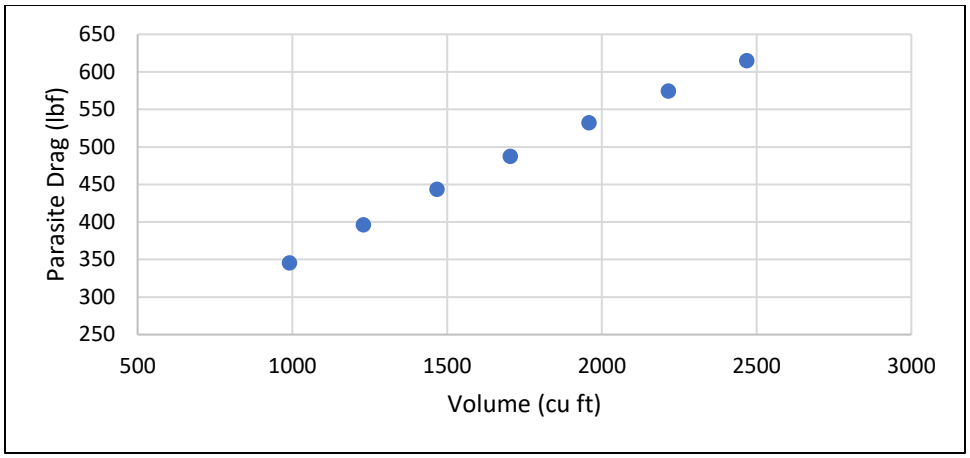

Figure 3.2 Parasite drag of optimized external fuel tanks of varying volumes

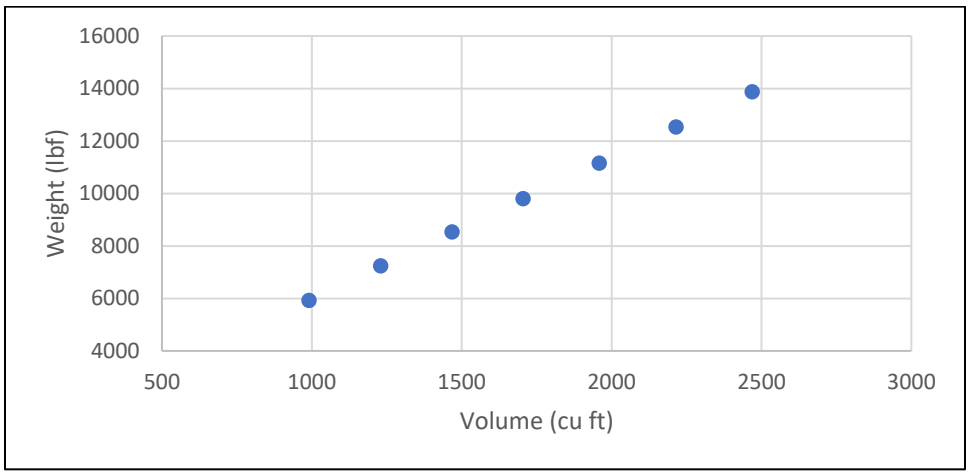

Figure 3.3 Total weight of optimized external fuel tanks of varying volumes

Table 3.1 Fuel tank properties for selected tank volumes

Fuel Tank	Length (ft)	Effective Diameter (ft.)	Volume (cu ft.)	Fuel Weight (lbf.)	Structural Weight (lbf.)	Parasite Drag (lbf.)
1	51.95	9.14	2215.38	9818.56	2930.61	574.50
2	47.61	8.38	1704.53	7554.49	2462.34	487.42
3	42.72	7.5	1229.83	5450.60	2002.09	396.40

Chapter 4: Aircraft Design Trade-Off Study

This chapter presents the analysis of aircraft models with varying wing, fuselage, and fuel tanks designs in RDSwin.

4.1 Aircraft Models

In this study, the most widely used B737- 800 was chosen as the baseline aircraft as an example of a single isle mid-range aircraft. Figure 4.1 shows a model of the B737-800 recreated using the RDSwin software with a cantilever wing and wing mounted engines. This is compared to a configuration with the same B737-800 fuselage and wings converted to use external hydrogen tanks rather than Jet A stored in the wing boxes. The hydrogen powered configuration shown in Figure 4.2. has external tanks mounted on the wings. For each case with wing mounted fuel tanks, the engines were shifted to the aft portion of the aircraft fuselage. This is beneficial because it reduces wing loading and improves the overall safety of the aircraft by minimizing the risk of damage to the fuel tanks caused by the engine failure. A T-tail was also created for the hydrogen powered 737-800 to account for the shift in engine position.

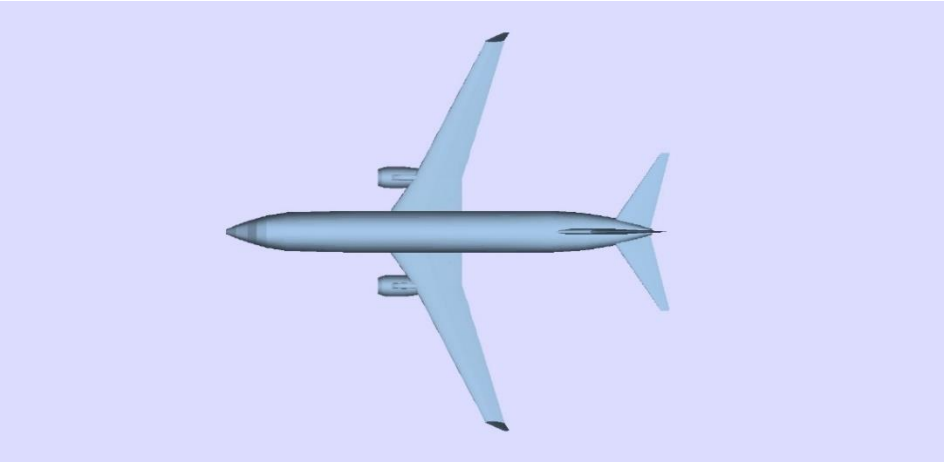

Figure 4.1 RDSWin designed model of the B737-800

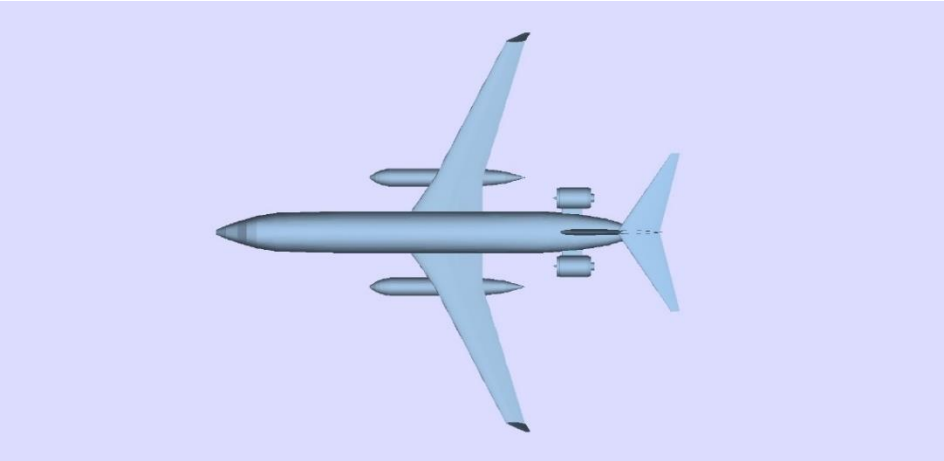

Figure 4.2 RDSWin designed model of the hydrogen powered B737-800 with external fuel tanks

The other two configurations investigated swap the traditional cantilever wing for a truss braced wing. Boeing and NASA have been studying the truss braced wing concept as part of the Subsonic Ultra Green Aircraft Research (SUGAR) program aimed at reducing noise and emissions while improving aircraft performance. In Phase IV of the project, a transonic truss braced wing (TTBW) concept was investigated with a cruise Mach number of 0.80 [5]. The TTBW has high aspect ratio (~19.23) and span of 170 ft and can improve lift and vehicle performance in comparison to standard cantilever wings. This large span is supported by a truss and requires a wing fold similar to that of a Boeing 777X to improve the airport gate accessibility. In this study, multiple aircraft configurations are investigated using a TTBW based on the SUGAR IV concept with varying fuselage and fuel tank designs. The hydrogen powered 737-800 configuration was modified by replacing the wing with the truss braced concept as shown in Fig. 4.3. Three different external tanks sizes were tested on both external tank configurations. The last model shown in Fig. 4.4 also uses the truss braced wing but has a larger fuselage comparable to a B767 to incorporate internal fuel tanks. The main capped cylinder tank is located at the rear of the aircraft behind the bulkhead while subsidiary smaller fuel tanks are located in the ceiling of the aircraft; the two models are

further evaluated to compare the aerodynamic efficiency of internal vs. external fuel tanks. Table 4.1 shows the approximate dimensions of the TTBW in comparison to those of a B737-800.

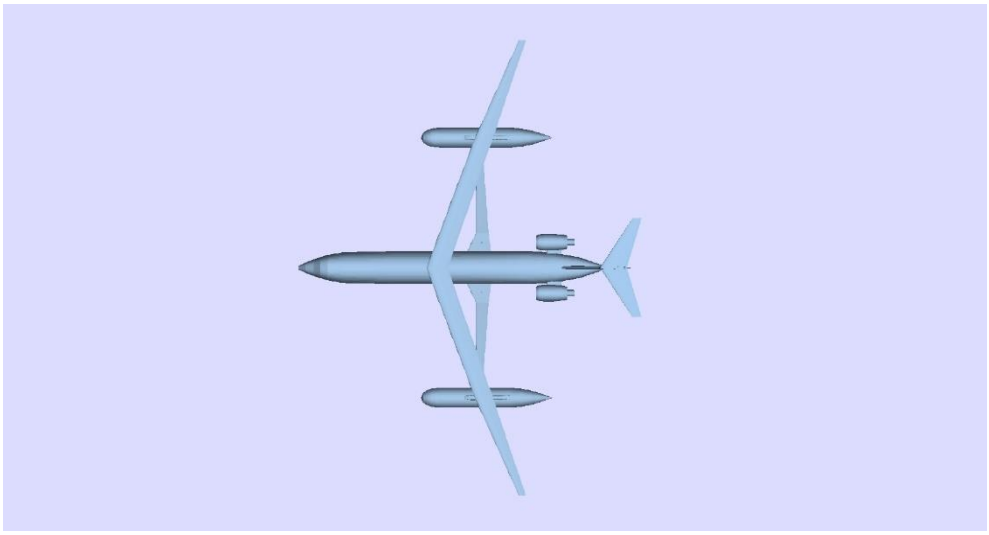

Figure 4.3 RDSWin designed model of the hydrogen powered TTBW aircraft with external fuel tanks

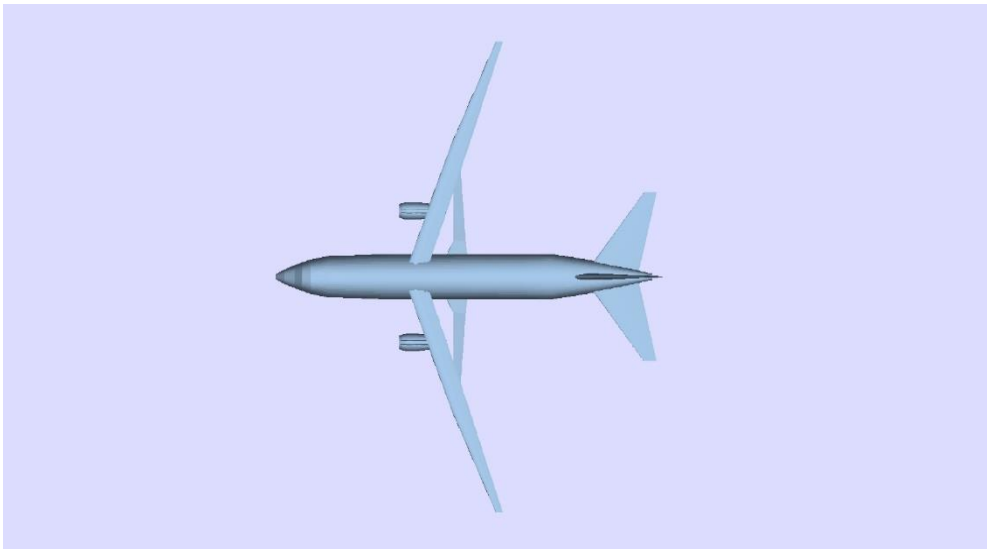

Figure 4.4 RDSWin designed model of the hydrogen powered B767 - TTBW aircraft with internal fuel tanks

Table 4.1 Comparison of aerodynamic component dimensions of Boeing B37-800 and RDSwin B737-TTBW

	Boeing 737-800	**737 - TTBW**
Wing		
Span (ft)	113.0	170
Aspect Ratio	9.45	19.23
Taper Ratio	0.159	0.330
Root Chord	20.549	10.77
Tip Chord	3.267	3.267
LE Sweepback Angle	28.52	28.52
Planform Area (ft^2)	1340	1477 (including truss)
MAC (ft)	13.998	7.7667
Horizontal Tail		
Span (ft)	46.61	36.919
Aspect Ratio	6.16	5.047
Taper Ratio	0.203	0.341
Root Chord	12.58	10.909
Tip Chord	2.55	3.72
LE Sweepback Angle	34.4	35.66
Area (ft^2)	352	270.069
MAC (ft)	8.675	7.904
Vertical Fin		
Span (ft)	26.154	16.04
Aspect Ratio	1.94	1.072
Taper Ratio	0.271	0.868
Root Chord	21.214	16.02
Tip Chord	5.749	13.901
LE Sweepback Angle	40.299	44.13
Area (ft^2)	352.6	239.93
MAC (ft)	14.96	14.987

The initial design phase uses the aircraft design and analysis tool RDSWin to evaluate the aerodynamics, propulsion, weights, and sizing to a mission profile and performance. The weight estimation method of Daniel Raymer [17], Jan Roskam [18], Egbert Torenbeek [19] and the NASA Flight Optimization System [20] were used to get a weight average of the empty weight of the various aircraft configurations. These weight calculation methods account for the propulsion system, structures and subsystem components like landing gear and controls systems. An estimation of a CFM56-7B24 engine deck is implemented assuming similar thrust by Jet A and

liquid hydrogen. The thrust specific fuel consumption for a hydrogen burning engine is obtained from the Jet A using the difference in heat content. Figure 4.5 shows a schematic of the mission profile utilized in RDSwin along with the fuel reserve requirements implemented across all four configurations [21].

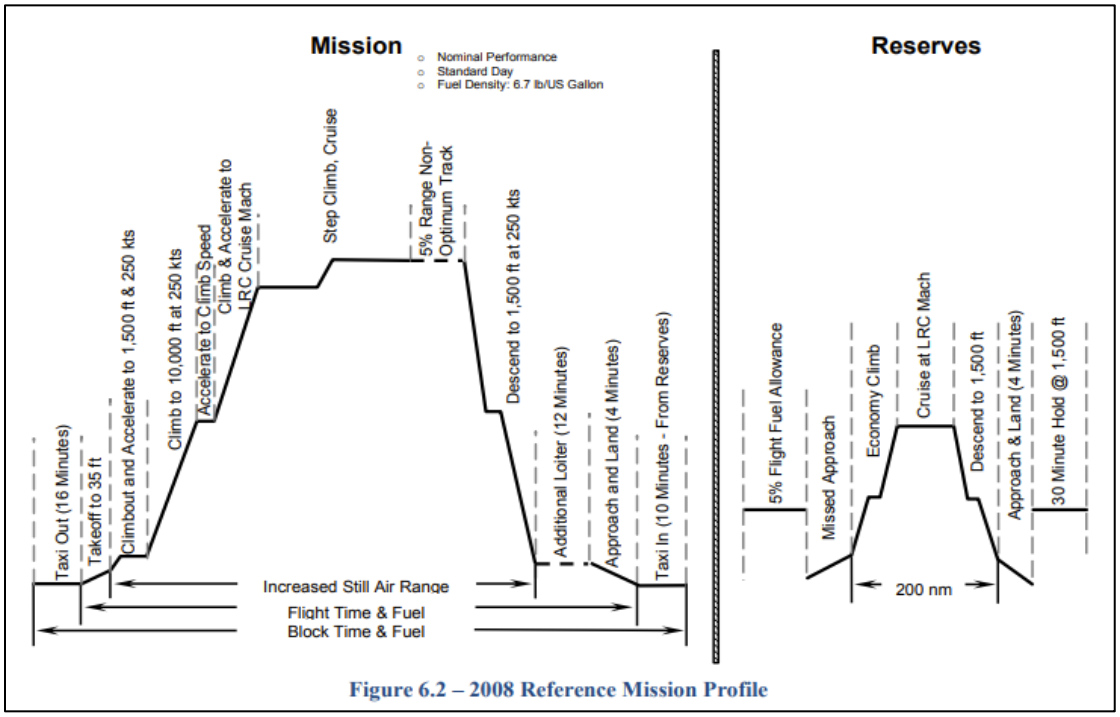

Figure 4.5 Mid-range single isle aircraft 2008 reference mission profile [21]

4.2 Results and Discussion

A summary of the aircraft performance results generated in RDSwin is shown in Table 4.2. The baseline B737-800 configuration was used for validation by matching the payload and range comparison chart shown in Fig. 1.1. The hydrogen configurations show a drastic decrease in the fuel weight required to travel a similar range as the B737-800 using Jet A. This is however partially offset by an increase in drag due to greater volume and surface area required for tanks. Due to the minimal increase in structural weight of the tank with the increase in tank volume for the three

different external tank designs, the long range cases with greater fuel volume have better specific ranges for the hydrogen powered B737-800 and hydrogen powered B737-800 with TTBW. With similar fuel volumes used, it can be seen that the increased span and aspect ratio of the TTBW as well as the weight savings improve the performance of the aircraft. Current work most likely underpredicts the effectiveness of the TTBW concept as the B737-800 airfoil is implemented across all four designs. Design and optimization of an airfoil for the TTBW configurations would show further increase in its range capabilities. As a results of the reduce drag, the hydrogen powered TTBW 767 configuration performed best across all three test cases. The B767 has the best potential to be improved in the future work by modification and optimization of the fuselage in conjunction with the internal tank shapes to reduce drag and weight.

Table 4.2 Range comparison of RDSwin models using varying fuel weights

	737-800 Jet A	**737-800 LH2**			**737-800 TTBW LH2**			**767 TTBW LH2**		
Fuel Weight (lb)	46067.8	10901	15109	19637.1	10901	15109	19637.1	10901	15109	19637.1
Range (NM)	2836.9	1477.5	2145.1	2934	1488.3	2349.7	3304.3	1585.9	2485.9	3426.1

Further analysis was done by evaluating the flight envelopes and specific ranges of the four aircraft. This was done for the Jet A B737-800 as well as the three hydrogen powered aircraft for the 15109 lb. fuel weight case. Figure 4.6 shows the flight envelope for the Jet A B737-800 with the expected flight ceiling approaching 41,000 ft. The increased drag caused by the external tanks reduces the service ceiling due to the 300 fpm rate of climb limitation at the service ceiling as shown in Figs. 4.7 and 4.8. The flight envelope of the B767 provided in Fig. 4.9 shows its potential to reach a similar service ceiling to that of the baseline Jet A B737-800.

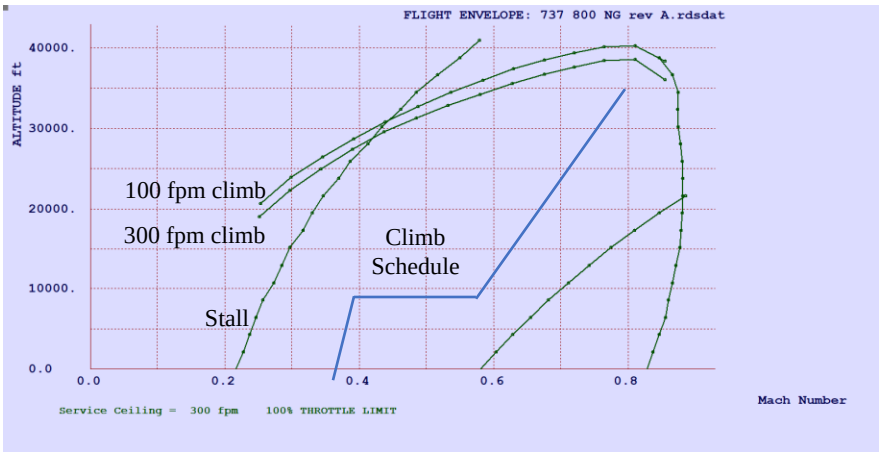

Figure 4.6 B737-800 Jet A flight envelope

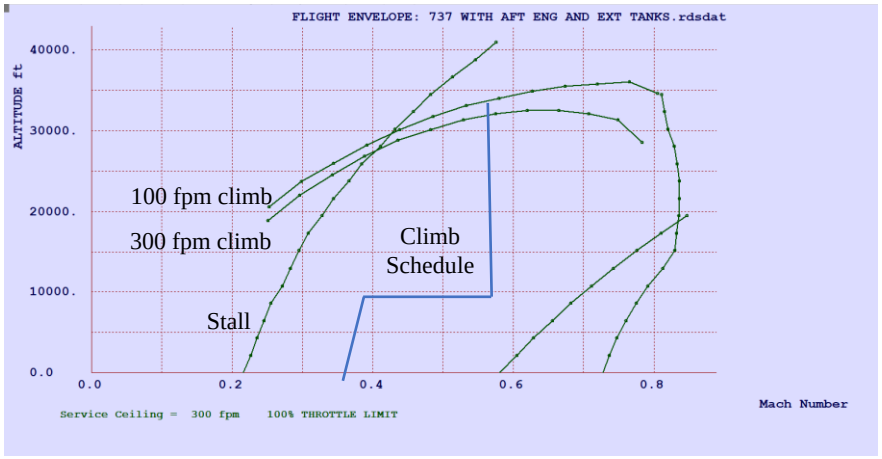

Figure 4.7 B737-800 LH2 flight envelope

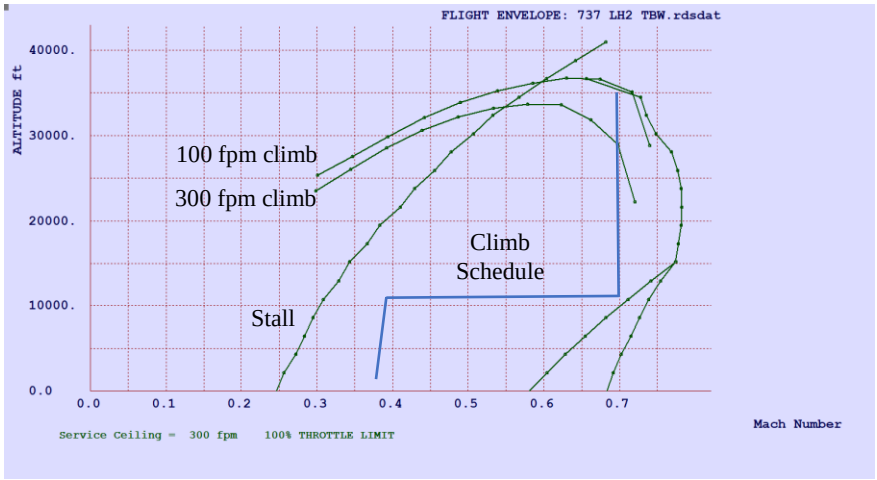

Figure 4.8 B737-800 LH2 TTBW flight envelope

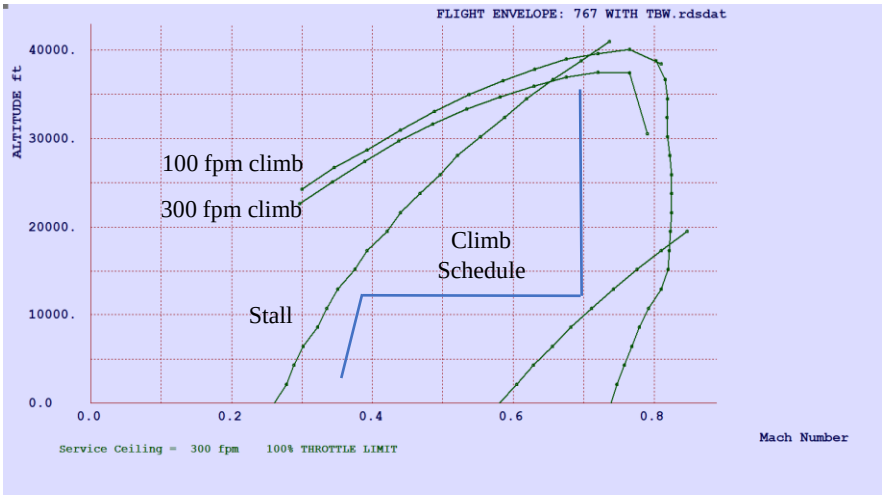

Figure 4.9 B767 TTBW LH2 flight envelope.

The cruise speed calculated by RDSwin is shown in Table 4.3. Due to variations in lift and drag caused by aerodynamic components and external tanks, the flight envelope and cruise speed varies across the design configurations. The cruise speed is limited for the 737-800 with LH2 external tanks due to the high drag relative to the engine thrust. These values are important for interpreting the plots of specific range. Figures 4.10-4.13 show the plots of specific range with respect to velocity for the four aircraft. For each case the specific fuel consumption was calculated at the cruise condition using the ratio of the aircraft weight after climb to the TOGW. The Jet A B737-800 aircraft is shown to have a significantly higher specific fuel consumption. The truss braced wing (TTBW) aircraft is shown to improve the specific fuel consumption in comparison to the traditional cantilever wing for the hydrogen powered case. The B767 configuration with all internal tanks yielded the best specific fuel consumption among all four concepts.

Table 4.3 RDSwin aircraft model cruise speeds

	737-800 Jet A	**737-800 LH2**	**737-800 TTBW LH2**	**767 TTBW LH2**
Cruise Speed (kts)	461.1	322.6	405.2	401.7

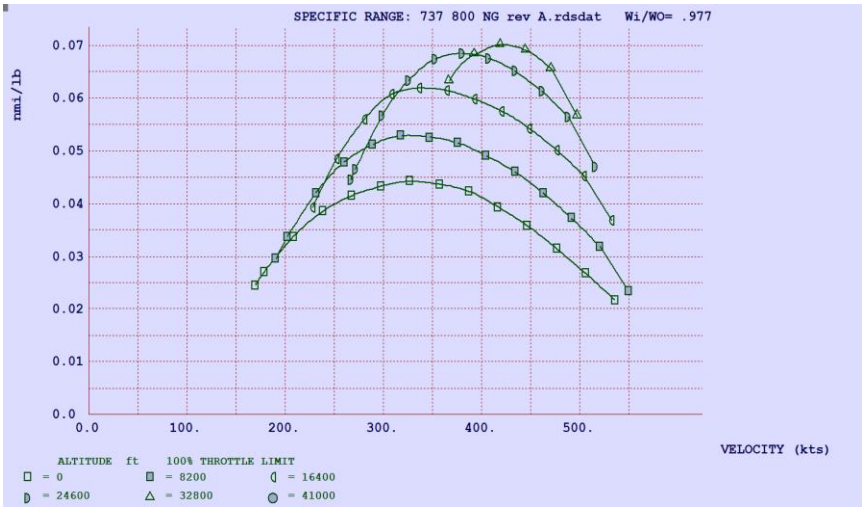

Figure 4.10 B737-800 jet A aircraft specific range

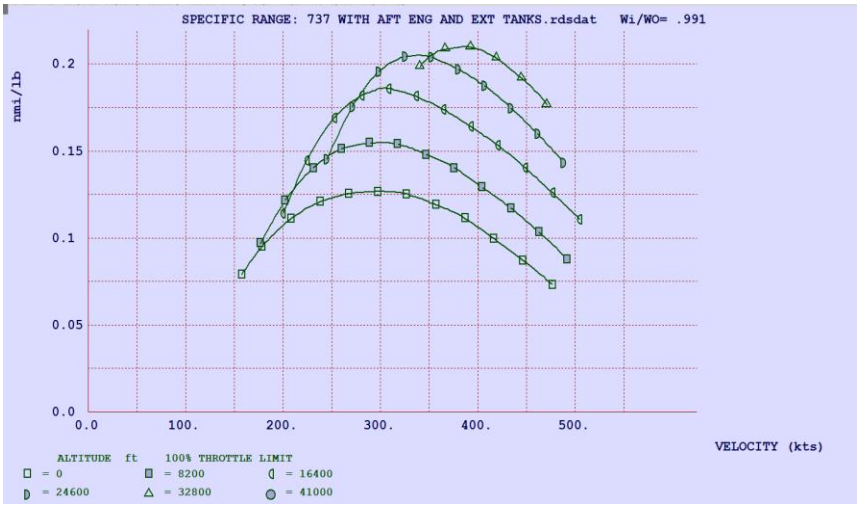

Figure 4.11 B737-800 LH2 aircraft specific range

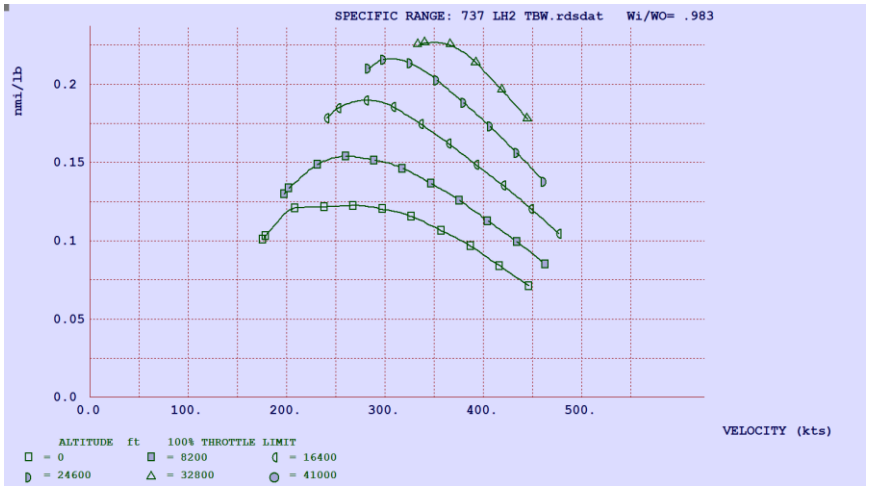

Figure 4.12 B737-800 LH2 TTBW specific range

Figure 4.13 B767 TTBW LH2 specific range

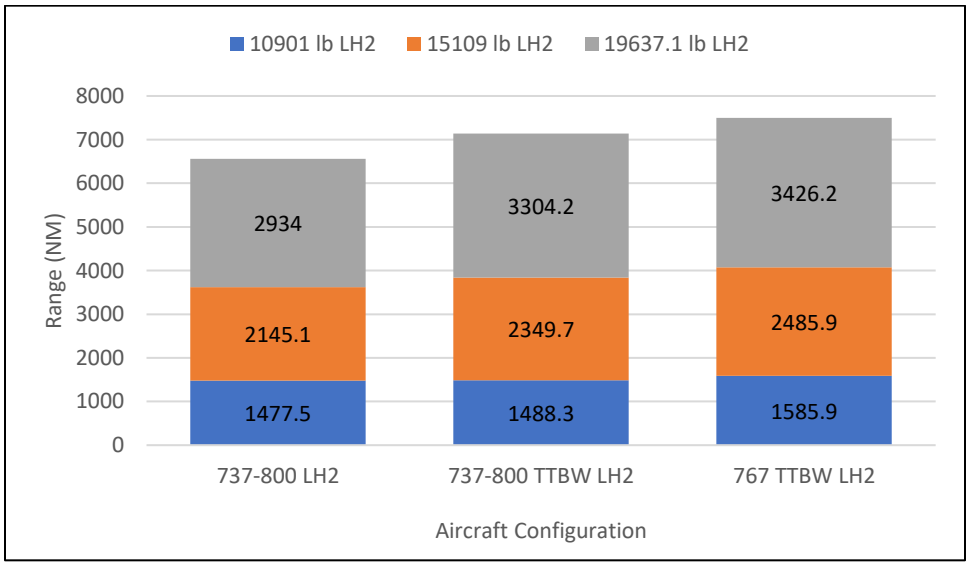

Figure 4.14 Range comparisons of liquid hydrogen aircraft configurations with varying fuel volumes

4.3 Conclusions

The analysis presented in this chapter provides the groundwork for further development of a hydrogen powered aircraft configuration based on a transonic truss braced wing (TTBW). It is shown that the internal LH2 tanks provide the best aerodynamic performance in comparison to external LH2 tanks mounted on the wing considering the specific range. The TTBW can also provide the necessary ground clearance for future N+3 and N+4 engines and open fan concepts

that can further bolster the aircraft performance. The B767 fuselage with TTBW and internal LH2 tanks appears to have the best potential for a future zero carbon emission liquid hydrogen powered aircraft.

Chapter 5: Turbulence Modeling of Wing and Wing-Body Juncture Flows

This chapter describes the numerical simulation and turbulence modeling of the ONERA M6 wing and wing-body Juncture Flow (JF) model.

5.1 CFD Solver

In this research, ANSYS Fluent is used to simulate a variety of fluid flows. ANSYS Fluent is a highly developed CFD solver that has been used to evaluate a wide array of fluid flows, heat and mass transfer and other challenges in both industry and academia. The parameterization feature is used to iterate through different test conditions. User Defined Functions (UDF) are implemented to incorporate the Wray-Agarwal turbulence model and the Quadratic Constitutive Relation.

5.2 Wing-Body Juncture Flow

5.2.1 Physical Model

In spite of several decades of major technology developments, accurate prediction of complex 3D turbulent flows still remains a challenging task. The accuracy of CFD results depends on the accurate implementation of its various building blocks namely the geometry modeling, mesh generation, numerical algorithms and turbulence models. Of these, turbulence models used in simulations with Reynolds-Averaged Navier-Stokes (RANS) equations remain a pacing item. There is general consensus in the scientific community that research is needed in development of more accurate and efficient turbulence models especially for 3D wall bounded separated flows encountered in many mechanical engineering and aerospace applications. The goal of this chapter is to evaluate the performance and accuracy of a relatively new one-equation turbulence model known as the Wray-Agarwal (WA) model for computing the wing-body juncture flows at various

angles of attack. Prediction of the flow characteristics of wing-body juncture flow using RANS equations has been a subject of several CFD investigations in recent years since the availability of NASA generated detailed experimental data [22] for benchmarking the CFD calculations. One of the important features of this flow is the separation bubble near the trailing edge region of the wing-body juncture whose prediction provides a challenge to CFD researchers using RANS modeling. Flow physics of wing-body juncture flow is complex due to the interaction of horseshoe, corner, and stress-induced vortices. Accurate modeling of the Reynolds stresses is necessary to predict the growth of the stress-induced vortex that delays corner separation. NASA began its first phase of juncture flow wind tunnel tests in 2017 to analyze the flow field characteristics of the wing-body junction region of an aircraft configuration. The experiments were conducted on a DLR F6-based wing -body with a horn/leading edge extension at various angles of attack in NASA Langley 14 by 22 foot subsonic wind tunnel. With the availability of a variety of commercial and open source CFD codes, CFD researchers are using these codes to investigate the influence of mesh, numerical algorithms, and turbulence models on the accuracy of computed flow field solutions; in particular the influence of various RANS turbulence models has been investigated. Previous CFD computations include the use of NASA FUN3D [23] and Overflow codes for simulating the F6-based wing body configuration for NASA 14x22 wind tunnel flow conditions [24]. In this chapter, the flow fields are computed using ANSYS Fluent [27] with free stream flow conditions and boundary conditions used by Rumsey et al. [23] with notable differences in the turbulence models implemented and mesh/grid generation methodology. The main objective of research reported in this chapter is to analyze the trailing-edge corner separation region using the Spalart-Allmaras (SA) [12], the Wray-Agarwal (WA) [13] and Menter's $k - \omega$ SST [10] turbulence models and to evaluate the effect of including the nonlinear Quadratic Constitutive

Relation (QCR) of Spalart [14] in place of Boussinesq approximation for eddy viscosity in these models by comparing the computations with wind tunnel data. The models with the inclusion of QCR are designated as SA-QCR, WA-QCR and $k-\omega$ SST – QCR. The WA model with a QCR modification developed by Nagapetyan in 2018 [25] has the potential to increase accuracy since QCR has been shown to improve results for several turbulence models [26].

The Juncture Flow Model (JFM) is an 8% scale model of the NASA Common Research Model with DLR-F6 wing with a wingspan of 3397.250 mm, a fuselage length of 4839.233 and a crank chord length of 557.17 mm [23]. Although tests were also run on a similar model without the leading-edge extension, the "with horn" configuration mitigates the influence of the horseshoe vortex making computation in the juncture region simpler. The effects of the wind tunnel wall and sting/mast mounting system are neglected in the calculations. A symmetry plane (x-z) is employed to reduce computational time for the simulations. A rectangular computational domain with a far field extent of 55,880 mm is employed in all simulations. Incident angles of 0, -2.5, 5 and 7.5 degree are chosen to test the accuracy of the SA, WA and $k-\omega$ SST and SA-QCR, WA-QCR and $k-\omega$ SST-QCR models in capturing the three-dimensional separation. The geometry of the computational model is shown in Fig. 5.1.

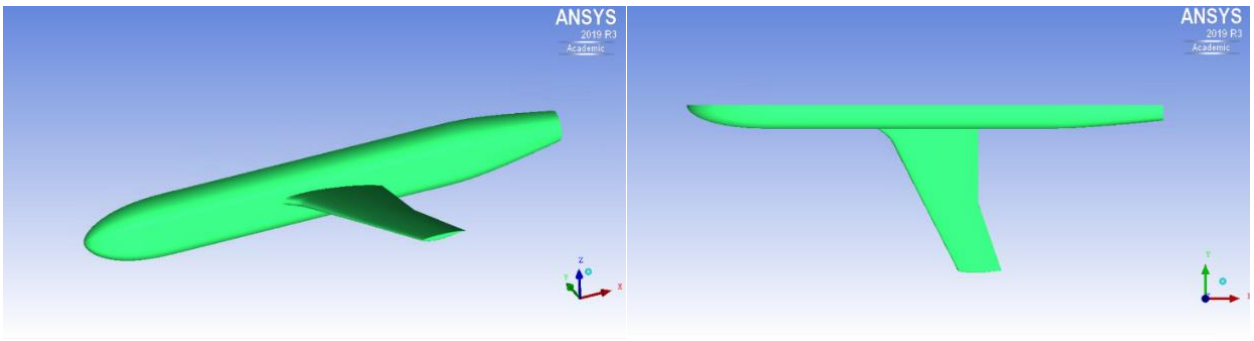

Figure 5.1 Wing-body juncture flow model geometry based on DLR F6 wing

5.2.2 Numerical Methods

ICEM CFD in the ANSYS software package was used for mesh generation. A structured mesh was preferred over an unstructured mesh due to its ability to provide higher control of node locations in the viscous region and the use of inflation layer growth algorithms. Structured mesh methods are also favored to reduce cell count without reducing accuracy, thereby decreasing simulation run time and computational memory requirements. The inflation layers are utilized to calculate flow parameters in the near wall region. The near-wall modeling approach requires a mesh resolved down to a $y+ < 1$ for the first grid point nearest to the wall. This was achieved by setting a first layer height of $5.7 * 10^{-6}$ m based on Reynolds number of 2.4 million calculated at the wing crank chord. This first layer height corresponds to the thickness of the initial layer of the O-grid used to capture the near wall region. The layer growth rate from the JFM surface was set geometrically with a growth rate of 1.2. Mesh refinement focused on the juncture region as well as the tip of the plane and leading-edge horn that affect downstream flow field features such as the trailing edge separation. The structured mesh employed is shown in Fig. 5.2; it is composed of approximately 19 million hex cells primarily with some quad cells.

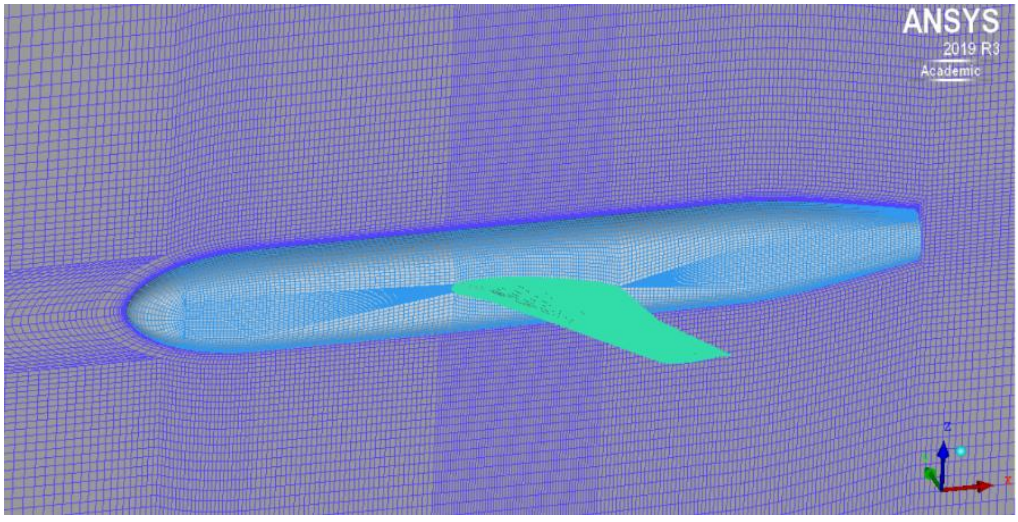

Figure 5.2 Structured mesh around the juncture flow model

One of the difficulties in simulating juncture flow arises from the viscous effects in the near wall region. Multitudes of methods have been developed to accurately capture the near wall region of turbulent boundary layer. The low Reynolds number modeling or wall functions are applied with several turbulence models in ANSYS Fluent depending upon the grid and $y+$ [25]. In all the simulations reported here, grid independence of the solution study was performed. First, calculations were performed using the Spalart-Allmaras (SA) one equation turbulence model to compare the computations with those of Rumsey et al. [23] who used FUN3D with SA model. Then WA and $k-\omega$ SST turbulence models were used to conduct the simulations which are compared with those of Rumsey et al. [23] and experimental data. Each model resolved the flow field all the way to the wall region and therefore log-law based wall functions are not needed for accurate simulations. Curvature correction was also implemented for each turbulence model.

Boundary conditions in the simulations were set so that they closely match the flow conditions in the wind tunnel. A median Mach number of 0.189 was used corresponding to an inlet velocity of 64.827 m/s. Turbulent inflow values were used to match those tested in the 14x22 wind tunnel [28]. It should be noted that although boundary conditions in simulations provide inflow conditions same as in the wind tunnel, they do not fully simulate the tripped flow in the experiment since fully turbulent conditions were utilized in the simulations. The common practice of setting boundary condition for R in the Wray-Agarwal (WA) model at inflow is the median value of the suggested range of $3\upsilon\infty$ to $5\upsilon\infty$ [13]. Simulations were run with a range of inflow R values which showed minimal variation in results. No-slip boundary conditions were used for the fuselage and wing walls of the model where R was set to 0.

5.2.3 Results and Discussion

The computations were performed using the Spalart-Allmaras (SA), Wray-Agarwal (WA), and $k - \omega$ SST turbulence models at 0, -2.5 5 and 7.5 degree angles of attack using a 19 million element mesh. Convergence was determined by monitoring the residuals of the flow field and turbulence variables. Monitors were also set to follow the variation in drag and lift coefficients. The solution was considered converged when the residuals decreased by 5 orders of magnitude. The post processing of simulations focused on predicting the size of the separation bubble which forms at the trailing edge of the juncture region, the surface pressure coefficient plots on various span-wise locations on the wing as well as the velocity and Reynolds stress profiles. Table 5.1 shows the predicted length and width of the separation region for each simulation and its comparison with wind tunnel results [22, 23]. At all four angles of attack, the Spalart-Allmaras turbulence model without a quadratic constitutive relation (QCR) modification over predicted the separation size. The WA model predicted a slightly larger separation size at each angle of attack in comparison to the SA model. At all four angles of attack the $k - \omega$ SST model similarly over-predicts the separation size but to a lesser degree than the other models.

Table 5.1 Comparison of separation bubble size predictions using different turbulence models

Separation Size [mm]	Angle of Attack	Spalart-Allmaras	Wray-Agarwal	$k-\omega$ SST	Wind Tunnel [23]
Length	-2.5°	191.8	193.1	181.1	68.7
Width	-2.5°	42.4	44.8	36.4	21.4
Length	0°	206.1	211.49	193.0	84.9
Width	0°	45.8	50.6	39.7	29.1
Length	5°	242.5	247.7	231.0	110.6
Width	5°	49.0	55.4	43.0	40.3
Length	7.5°	266.7	273.8	260.9	124.9
Width	7.5°	52.9	59.5	50.1	47.3

Table 5.2 shows separation size predictions with the use of the QCR modification. It can be seen that for all three models, QCR yields a significant improvement in the separation length prediction and a small improvement in the separation width prediction. These results show that the WA and WA-QCR models can predict flow separation regions for complex flow cases comparable to other one and two equation models. Overall, the $k-\omega$ SST-QCR model achieves the closest prediction to the experimental data.

Table 5.1 Comparison of separation bubble size predictions using QCR turbulence models

Separation Size [mm]	Angle of Attack	SA-QCR2000	WA-QCR2000	$k-\omega$ SST QCR2000	Wind Tunnel [23]
Length	$-2.5°$	134.8	140.7	123.0	68.7
Width	$-2.5°$	34.2	35.8	31.0	21.4
Length	5°	157.6	162.7	155.50	110.6
Width	5°	47.4	50.7	41.39	40.3

Drag and lift coefficients were also calculated for the juncture flow model for the 5 degree angle of attack case. Although the wind tunnel data to date does not include lift and drag results, these are still valuable parameters for comparisons of results using different grids and flow solvers. The drag and lift coefficients used for comparison are the preliminary results from the High-Fidelity CFD Workshop 2021 [29]. Table 5.3 presents the drag and lift coefficient data obtained with the six turbulence models as well as NASA's preliminary CFD results. Each turbulence model correlates closely with the drag coefficient calculated by NASA. The SA and $k-\omega$ SST model also show good agreement for the lift coefficient.

Table 5.3 Juncture flow drag and lift coefficient predictions for the 5 degree angle of attack case

	Drag Coefficient	Lift Coefficient
High-Fidelity CFD Workshop: Preliminary Results [29]	0.07	0.85
Spalart-Allmaras	0.0693	0.854
Wray-Agarwal	0.0713	0.831
$k-\omega\ SST$	0.0697	0.857
Spalart-Allmaras-QCR2000	0.0690	0.849
Wray-Agarwal-QCR2000	0.0698	0.832
$k-\omega\ SST$-QCR2000	0.0688	0.851

Surface streamlines were generated in order to qualitatively compare the computations with the wind tunnel oil flow photographs. The separation region flow comparisons are shown in Figs. 5.3-5.6. It can be seen from these figures that the WA model yields good agreement with the wind tunnel oil flow images across the four angles of attack. Pressure distributions were computed for each angle of attack along the wing and fuselage. Figures 5.7-5.10 show the pressure profiles taken at y-planes relative to the center of the aircraft. Both SA and WA one-equation models show good agreement with the experimental pressure coefficient profiles. Additionally, the $k-\omega$ SST model shows good results for the pressure profiles on the wing of the juncture flow model compared to the wind tunnel data. Both the SA and WA model accurately predict the pressure coefficient profiles at x-planes of the wing shown in Fig. 5.11 and y-planes of the fuselage shown in Fig. 5.12. The upstream x-plane fuselage pressure distributions shown in Figs. 5.13-5.14 reflect a slight under-prediction of pressure for all three turbulence models compared to the experimental data. Overall, all three turbulence models accurately predict the pressure distribution on the juncture flow model. The addition of the QCR modification had minimal effect as the linear formulations already accurately predicted the pressure distribution.

Further analysis focused on evaluating the velocity and Reynolds stress profiles near the separation point and comparing them with the experimental data for the -2.5 and 5 degree angle of attack cases. A location upstream of the wing on the fuselage was also evaluated and compared to the

experimental laser Doppler velocimetry data (LDV). The velocity profiles in Fig. 5.15 demonstrate the ability of both WA and WA-QCR turbulence models to predict the upstream velocity profiles on the fuselage with acceptable accuracy. The $k-\omega$ SST model yields results similar to the SA model for the 5 degree angle of attack case for both locations. The WA model more accurately predicts the velocity profile near the separation point for the 5 degree angle of attack case and slightly under-predicts the x-velocity for the -2.5 degree angle of attack case. Near the separation point, there is minimal variation in results for the w and v velocity components of flow for the different models. The QCR modified models tend to predict a higher u velocity further from the wall than the linear counterparts.

Turbulent shear stress was also calculated at the same LDV sensor locations for both angles of attack. Figure 5.16 demonstrates the ability of the WA model to accurately predict the turbulent shear stress on the upstream section of the fuselage. The WA model more accurately predicts the Reynolds stress at the upstream fuselage station. At the upstream station the SA model over-predicts the Reynolds stress. The $k-\omega$ SST model accurately predicts the Reynolds stress near the wall but over-predicts it further outboard for the -2.5 degree case. At the upstream location QCR was shown to improve the prediction of the u'v' component significantly for the WA and $k-\omega$ SST model. The WA-QCR and $k-\omega$ SST QCR models best predicted the Reynolds stress at the upstream location.

Figure 5.17 also demonstrates the ability of the WA model to predict turbulent shear stress near the separation point. The WA model showed the best results of the linear models for the -2.5 degree angle of attack with less under-prediction of the components. All of the models show good agreement for the v'w' component but have difficult predicting the u'w' and u'v' components. It can be seen that the QCR modification improves each model's ability to predict the u'w'

component with the $k - \omega$ SST QCR and SA QCR models showing the best agreement followed by the WA-QCR. At the lower angle of attack, the WA and WA QCR models show improved prediction of the u'v' component close to the wall. All the turbulence models under-predict the u'v' component as shown in Fig. 5.17. This under-prediction is consistent with the findings of Rumsey et al. [30].

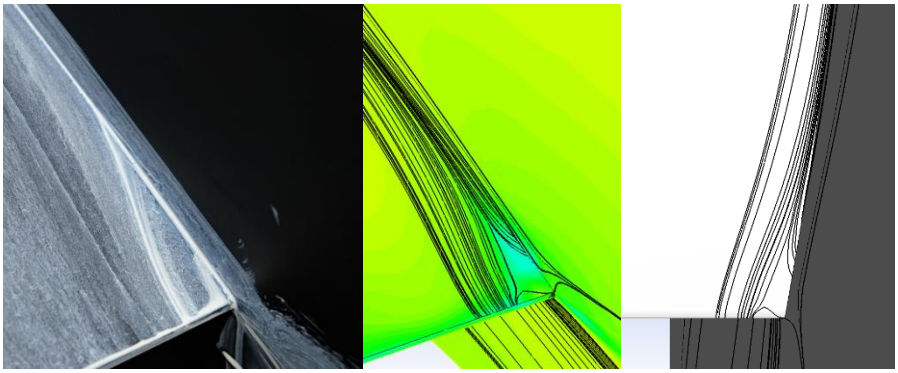

Figure 5.3 Trailing edge separation bubble at α = -2.5°, Oil Flow Photo (left) [28], WA CFD Result (right)

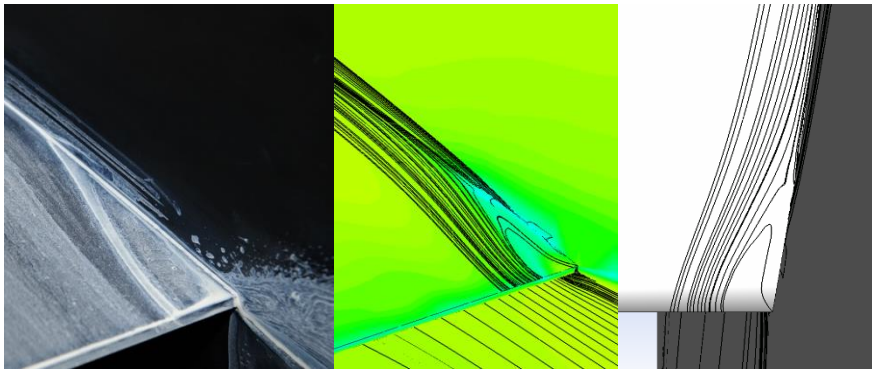

Figure 5.4 Trailing edge separation bubble at α = 0°; Oil Flow Photo (left) [28], WA CFD Result (right)

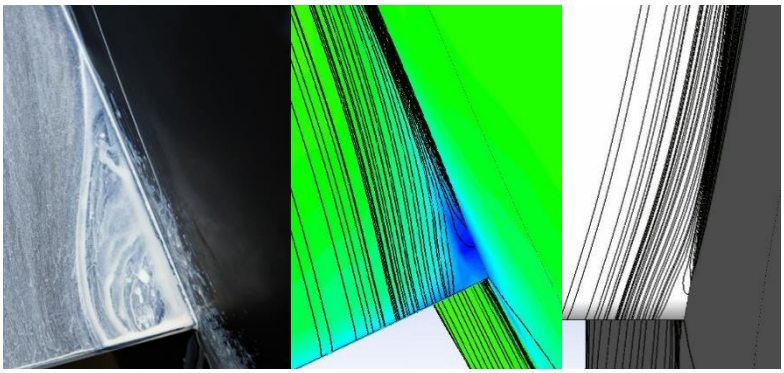

Figure 5.5 Trailing edge separation bubble at α = 5°; Oil Flow Photo (left) [28], WA CFD Result (right)

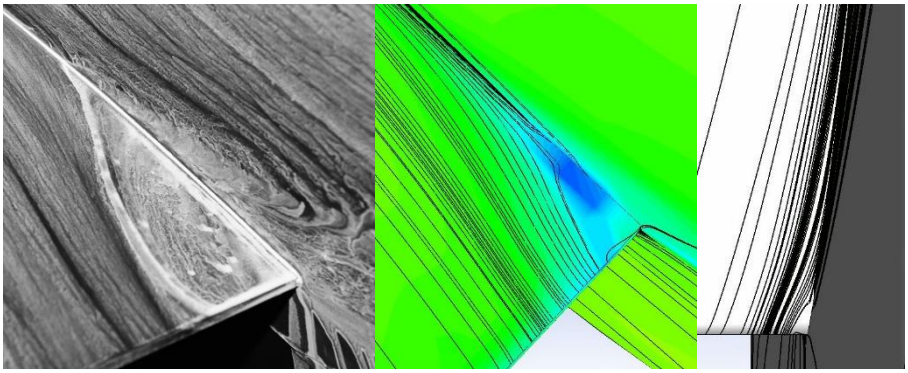

Figure 5.6 Trailing edge separation bubble at α = 7.5°; Oil Flow Photo (left) [28], WA CFD Result (right)

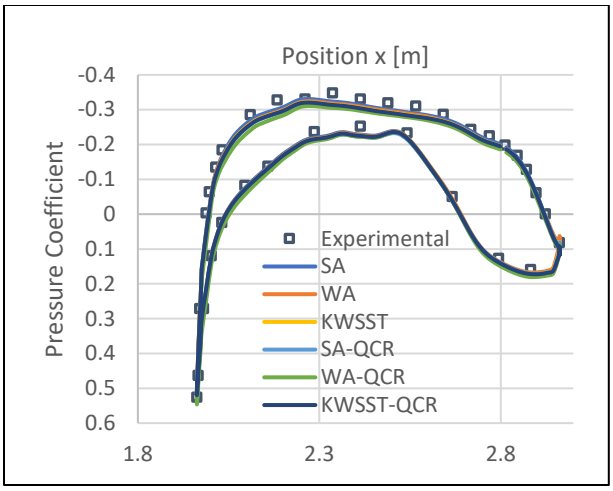

(a) Y = 254 mm

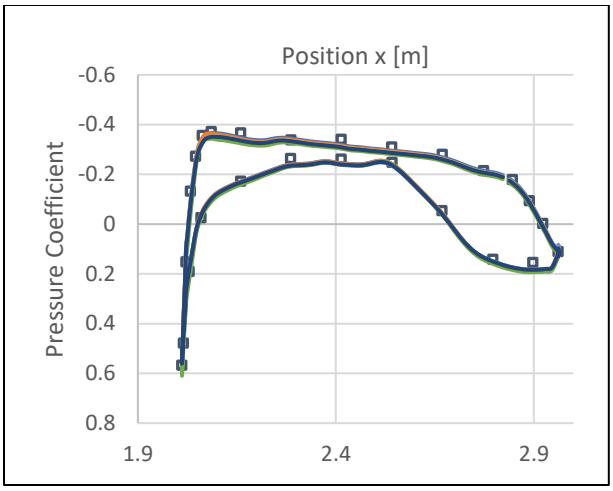

(b) Y = 290.83 mm

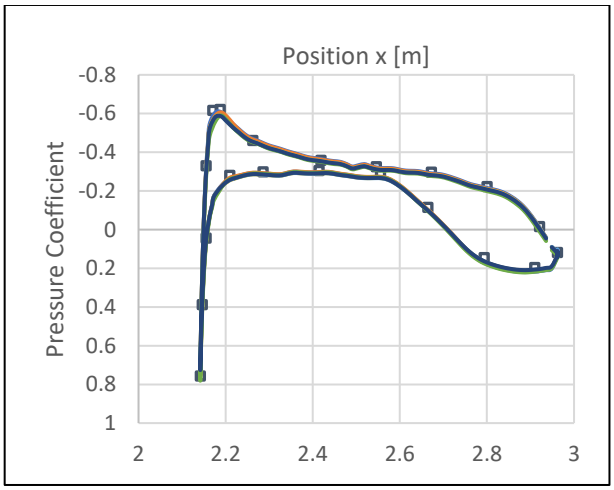

(c) Y = 482.6 mm

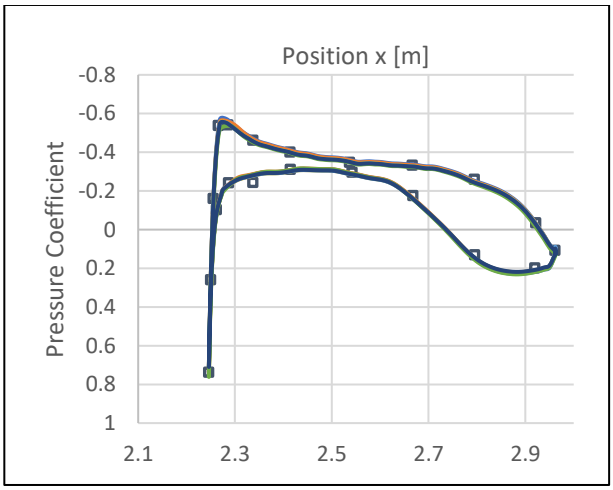

(d) Y = 685.8 mm

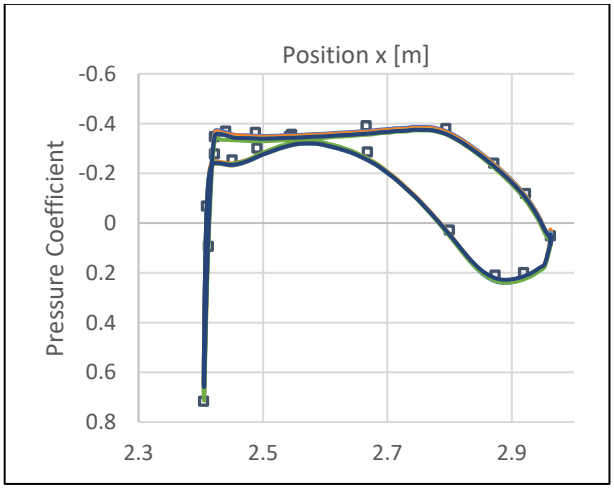

(e) Y = 994.92mm

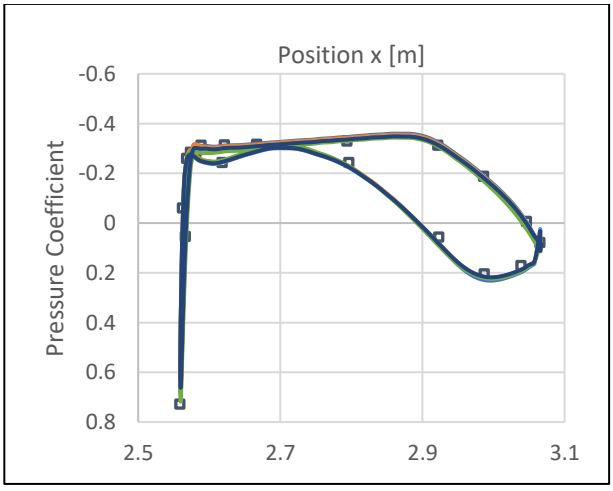

(f) Y = 1295.4 mm

Figure 5.7 Comparison of computed and experimental y-plane wing surface pressure coefficients for α = -2.5°

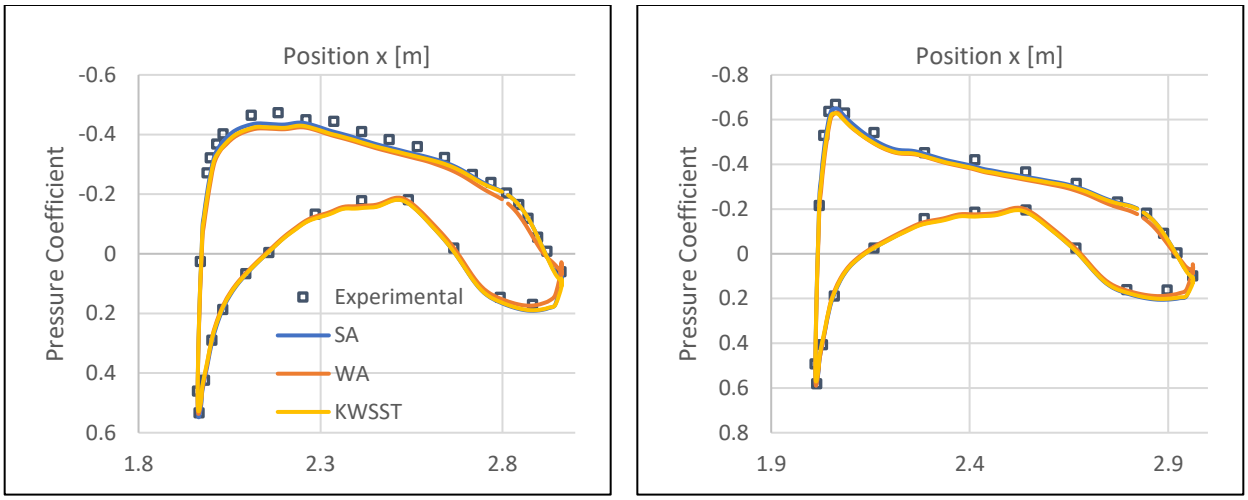

(a) Y = 254 mm

(b) Y = 290.83 mm

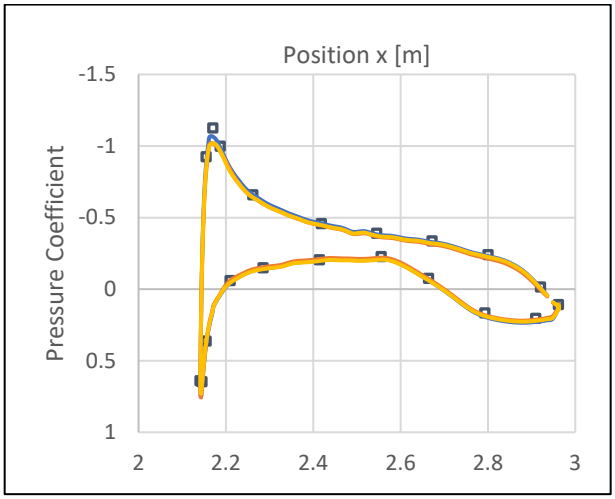

(c) Y = 482.6 mm

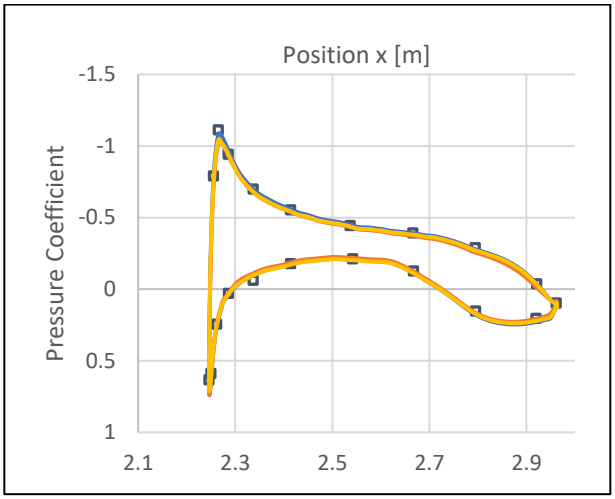

(d) Y = 685.8 mm

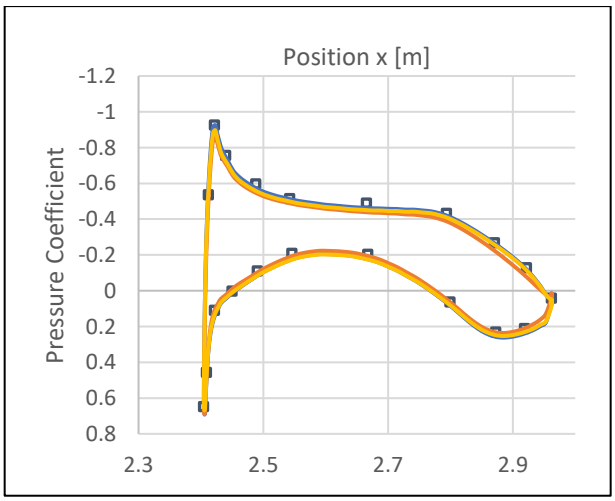

(e) Y = 994.92mm

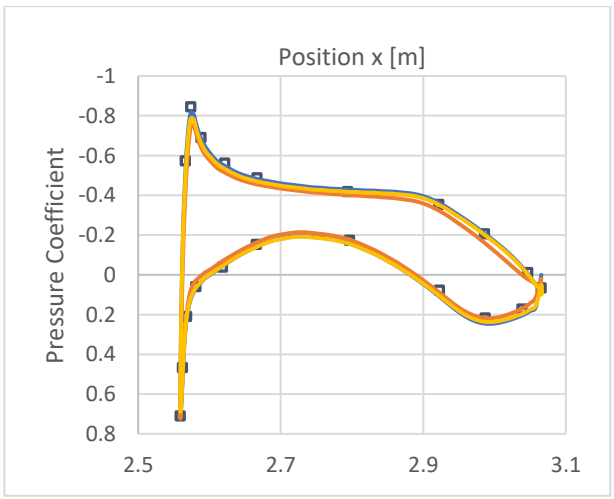

(f) Y = 1295.4 mm

Figure 5.8 Comparison of computed and experimental y-plane wing surface pressure coefficients for α = 0°

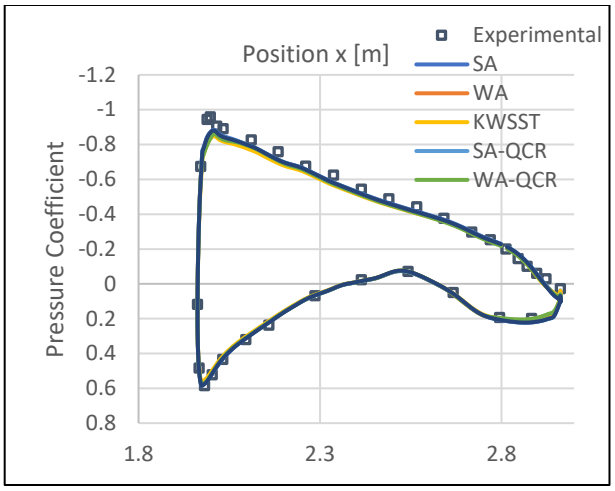

(a) Y = 254 mm

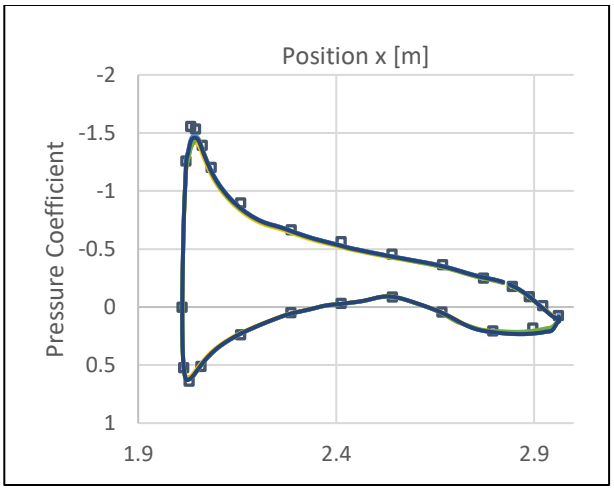

(b) Y = 290.83 mm

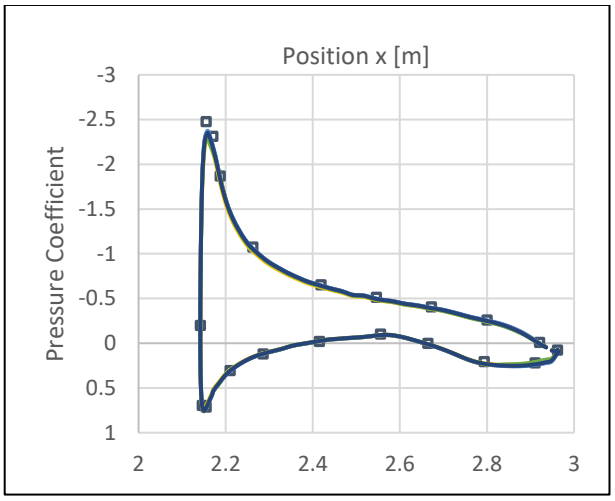

(c) Y = 482.6 mm

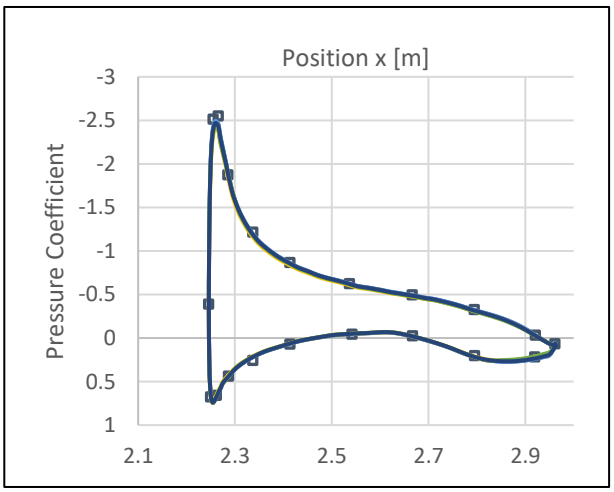

(d) Y = 685.8 mm

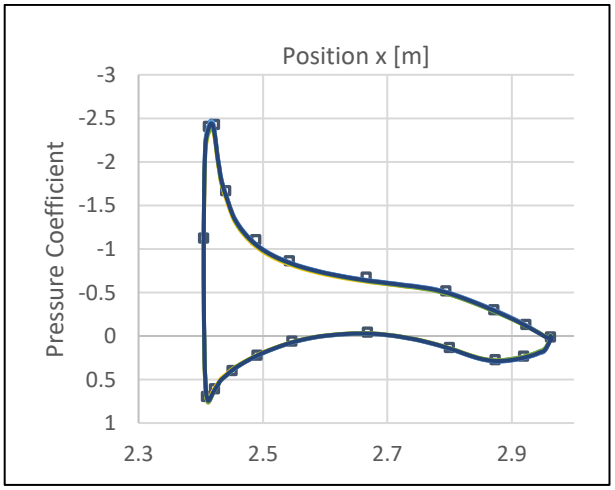

(e) Y = 994.92mm

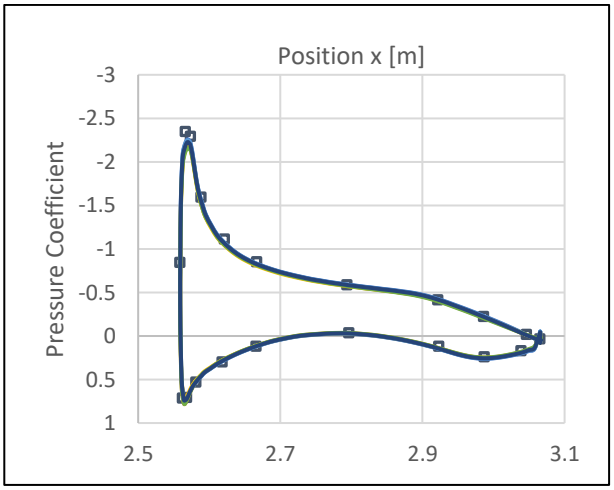

(f) Y = 1295.4 mm

Figure 5.9 Comparison of computed and experimental y-plane wing surface pressure coefficients for α = 5°

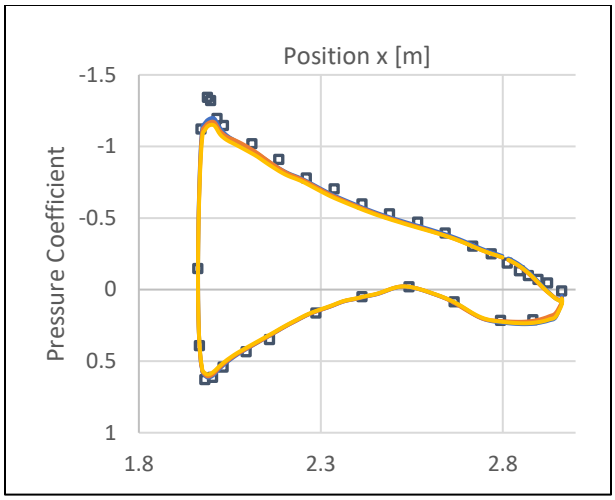

(a) Y = 254 mm

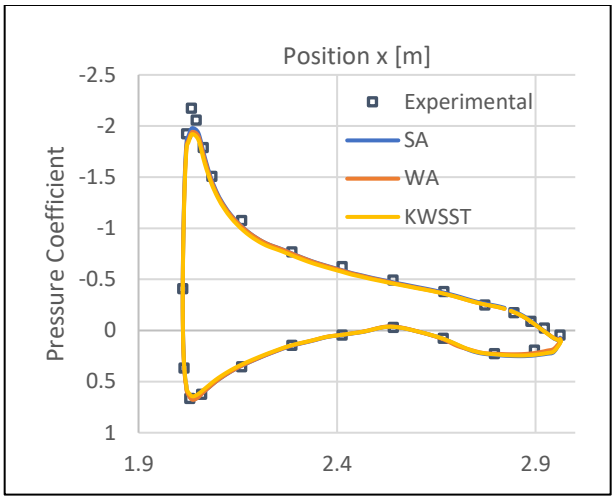

(b) Y = 290.83 mm

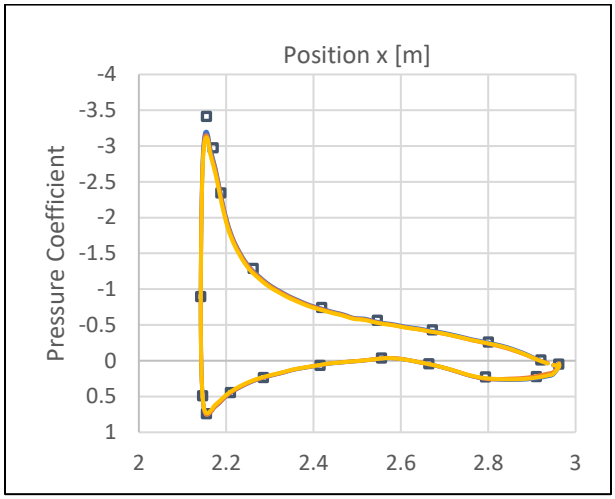

(c) Y = 482.6 mm

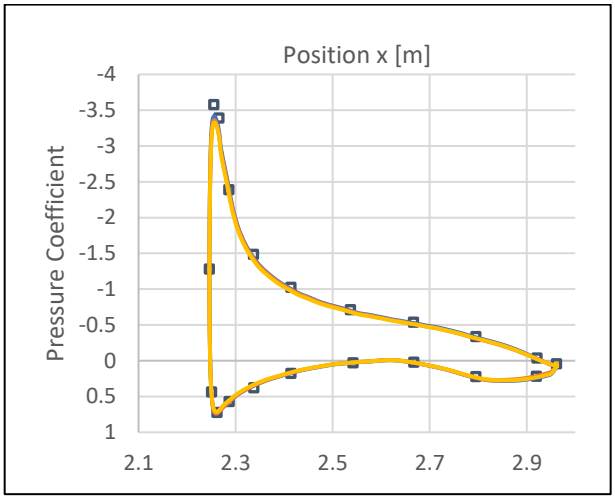

(d) Y = 685.8 mm

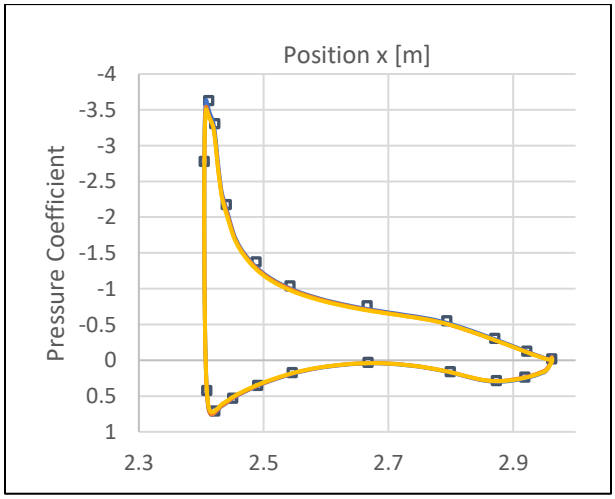

(e) Y = 994.92mm

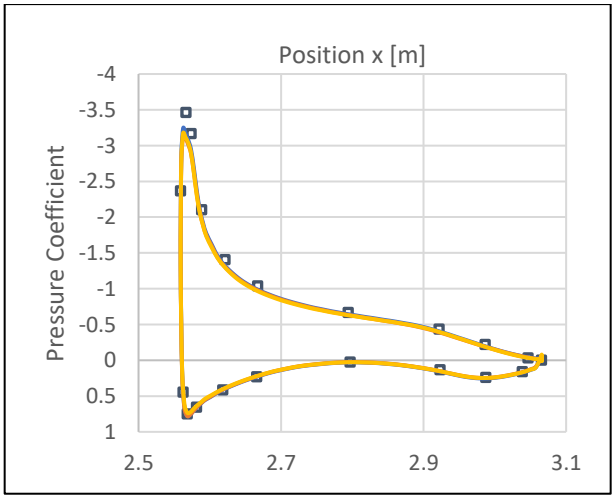

(f) Y = 1295.4 mm

Figure 5.10 Comparison of computed and experimental y-plane wing surface pressure coefficients for α= 7.5°

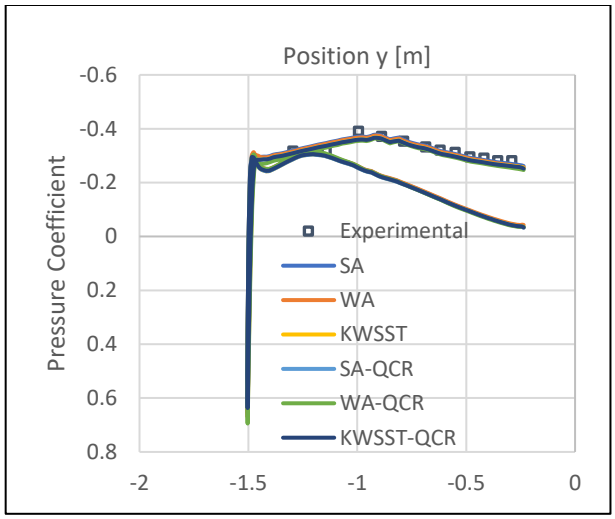

(a) α = 0°, X = 2667 mm

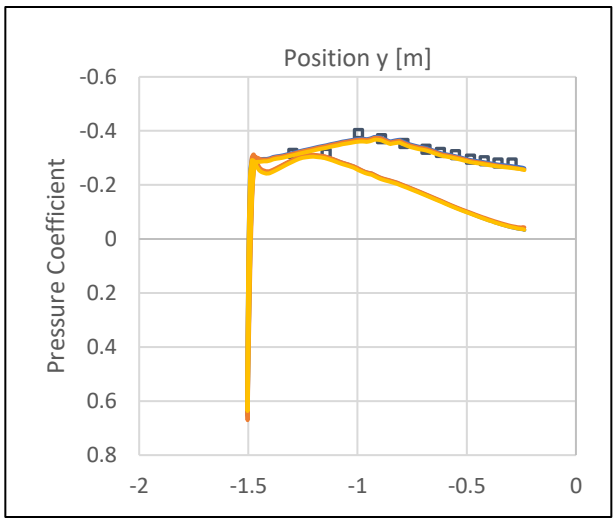

(b) α = -2.5°, X = 2667 mm

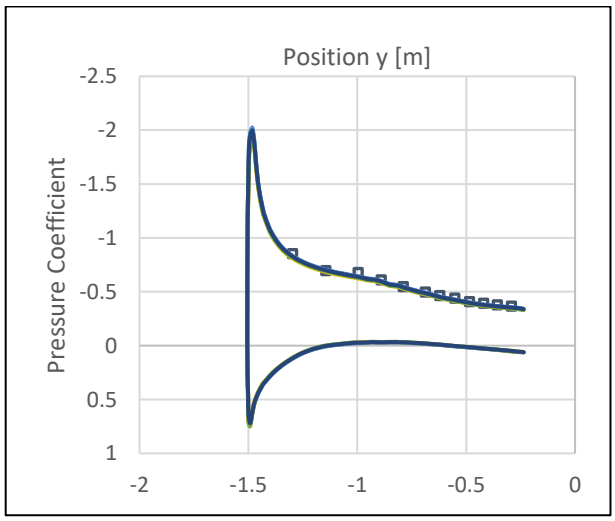

(c) α = 5°, X = 2667 mm

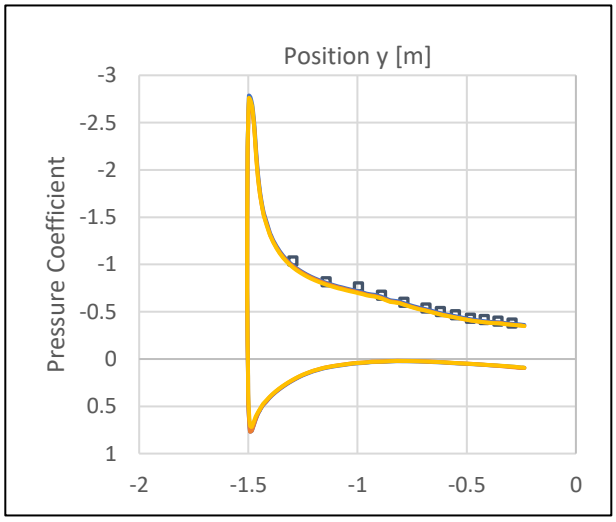

(d) α = 7.5°, X = 2667 mm

Figure 5.11 Comparison of computed and experimental x-plane wing surface pressure coefficients

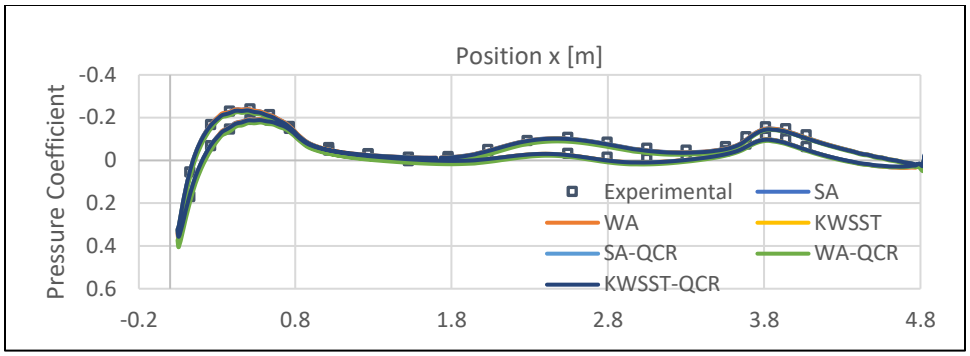

(a) α = -2.5°, Y = 76.2 mm

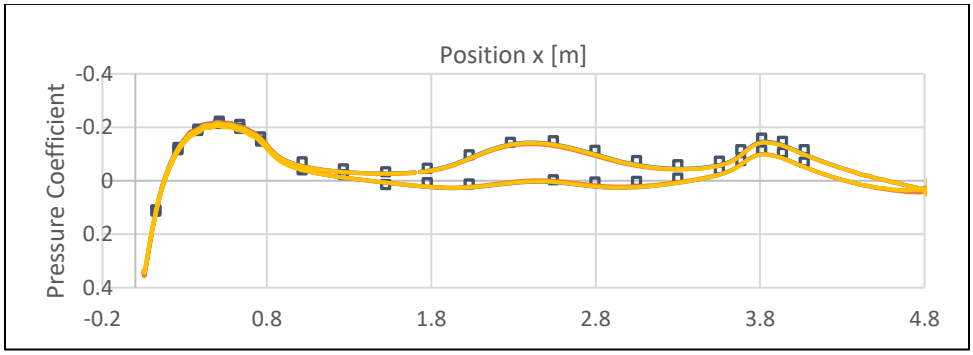

(b) α = 0°, Y = 76.2 mm

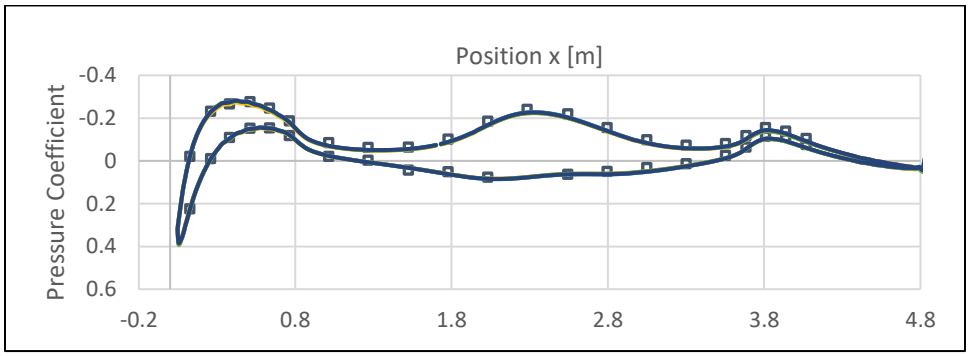

(c) α = 5°, Y = 76.2 mm

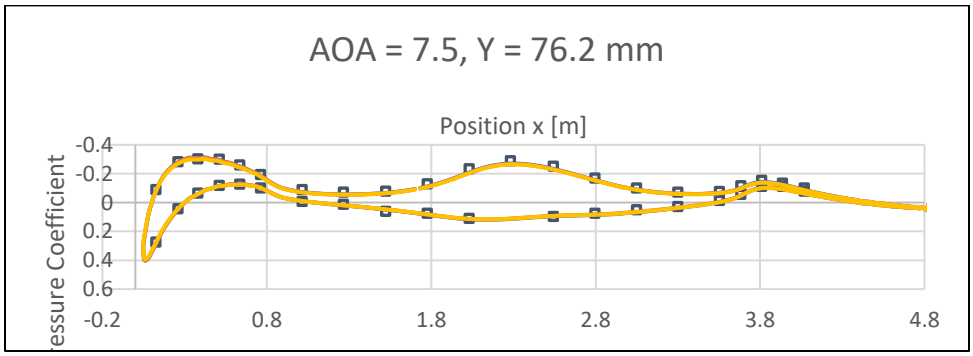

(d) α = 7.5°, Y = 76.2 mm

Figure 5.12 Comparison of computed and experimental y-plane fuselage pressure coefficients

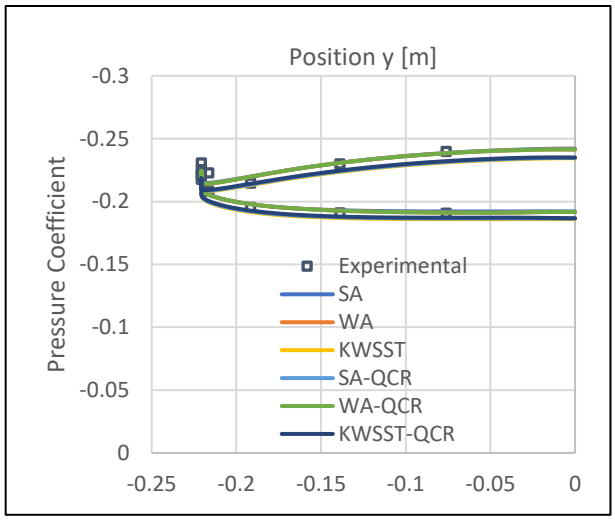

(a) α = -2.5°

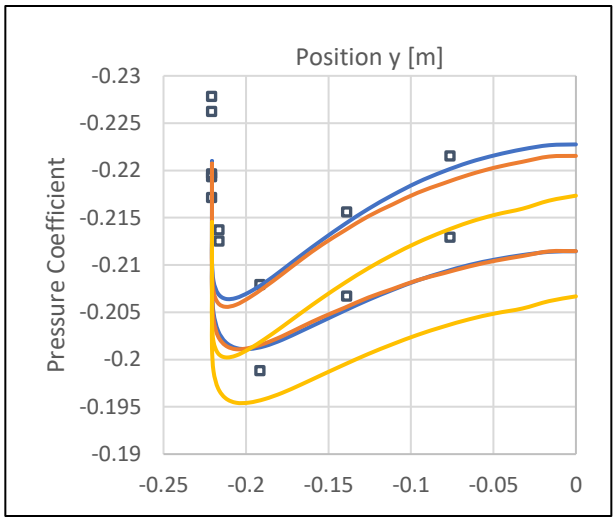

(b) α = 0°

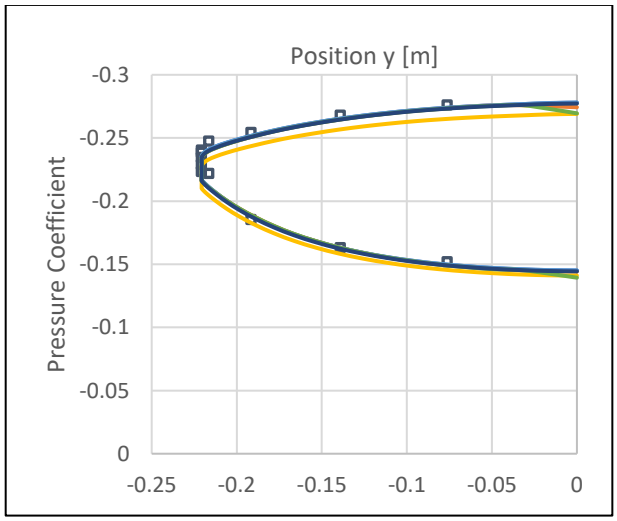

(c) α = 5°

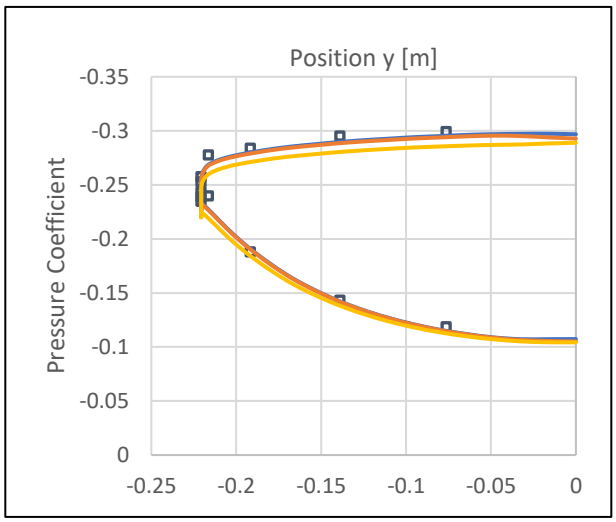

(d) α = 7.5°

Figure 5.13 Comparison of computed and experimental fuselage pressure coefficients at X = 508 mm

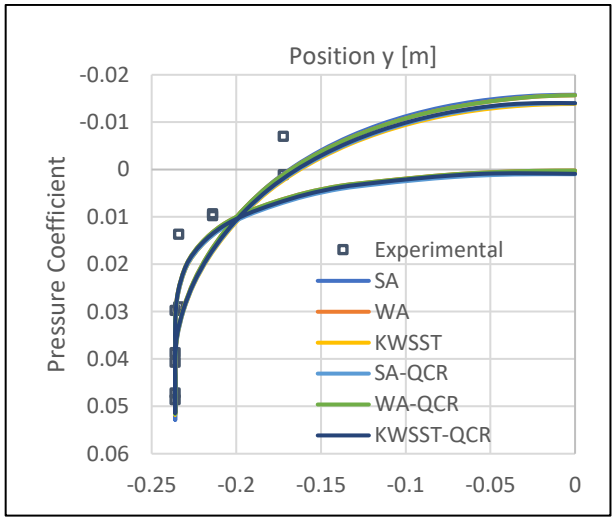

(a) α = -2.5°

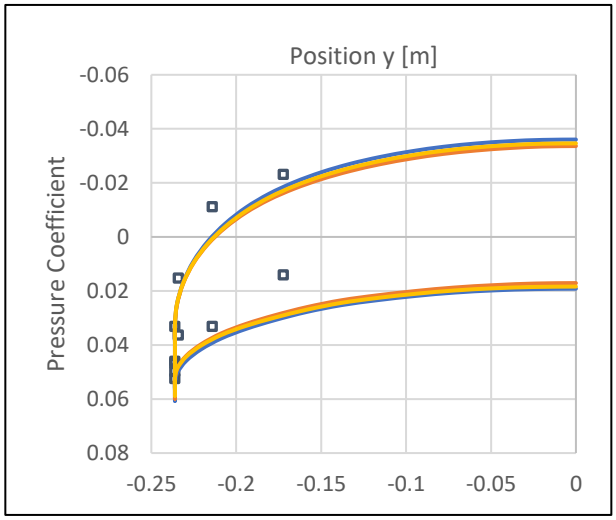

(b) α = 0°

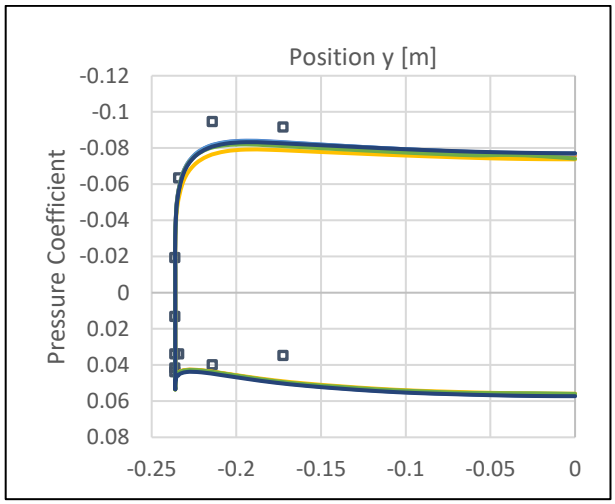

(c) α = 5°

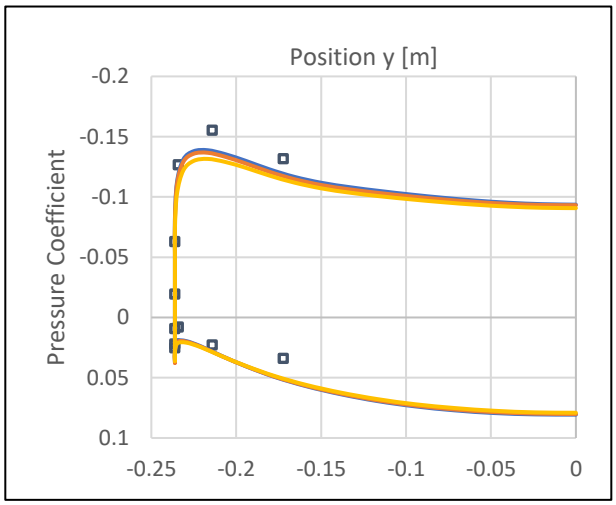

(d) α = 7.5°

Figure 5.14 Comparison of computed and experimental fuselage pressure coefficients at X = 1727 mm

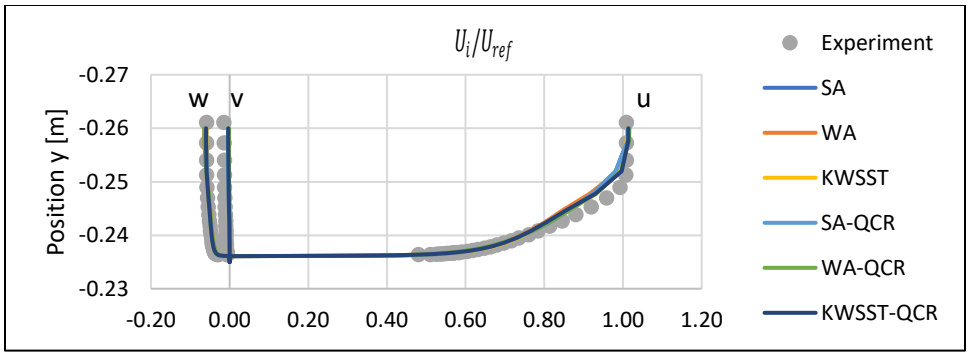

(a) α = -2.5°, X = 1164.4 mm, Z = 0 mm

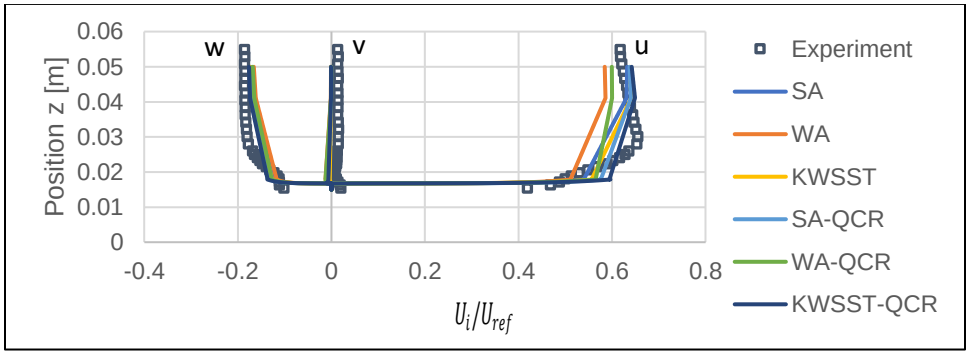

(b) α = -2.5°, X = 2747.6 mm, Y = -237.1 mm

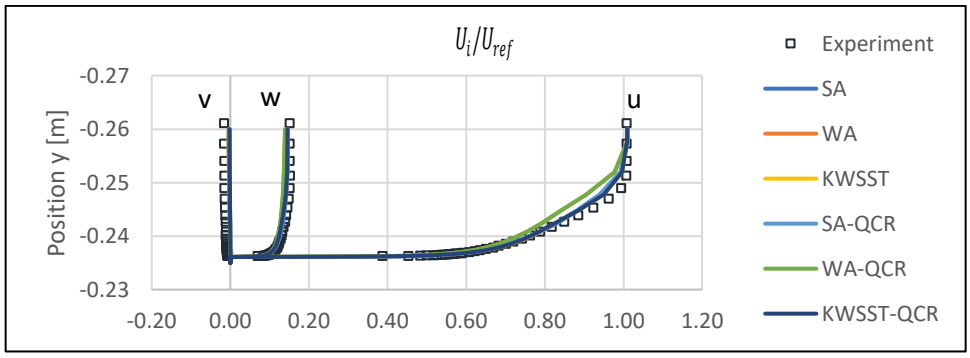

(c) α = 5°, X = 1164.4 mm, Z = 0 mm

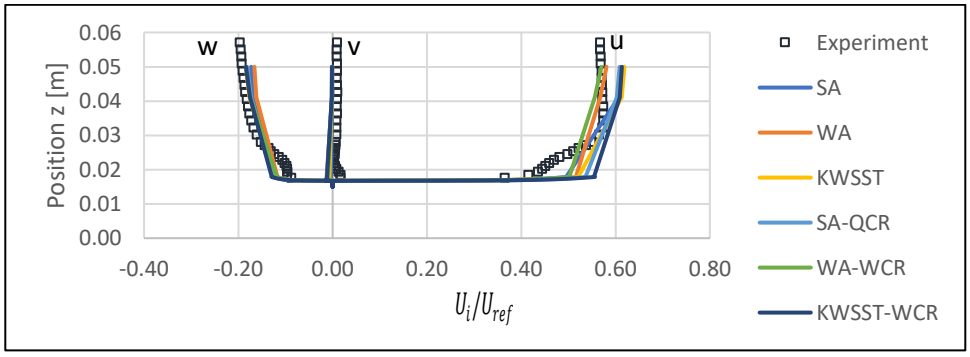

(d) α = 5°, X = 2747.6 mm, Y = -237.1 mm

Figure 5.15 Comparison of computed and experimental velocity profiles

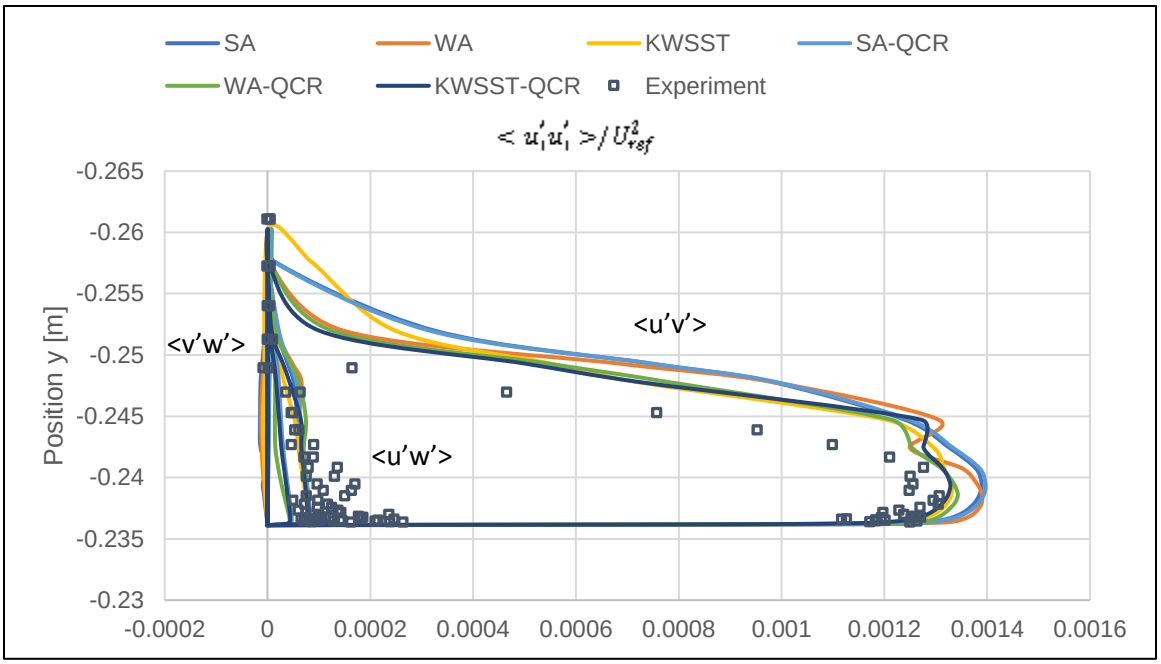

(a) α = -2.5°

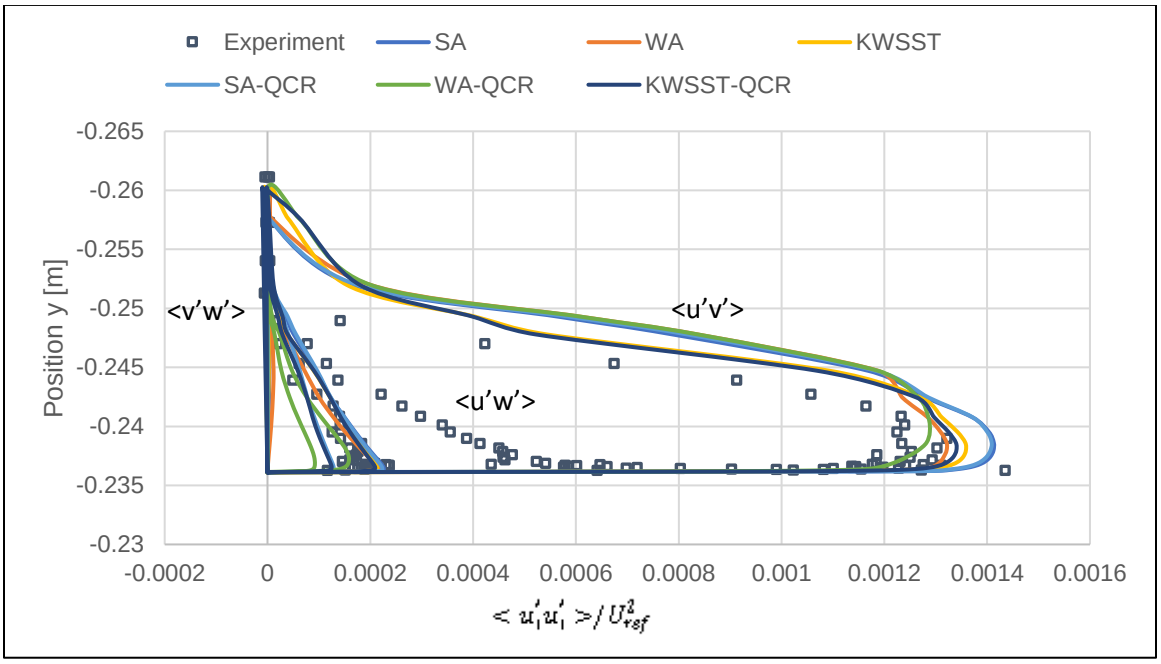

(b) α = 5°

Figure 5.16 Comparison of computed and experimental turbulent shear stress at X = 1164.4 mm, Z = 0 mm

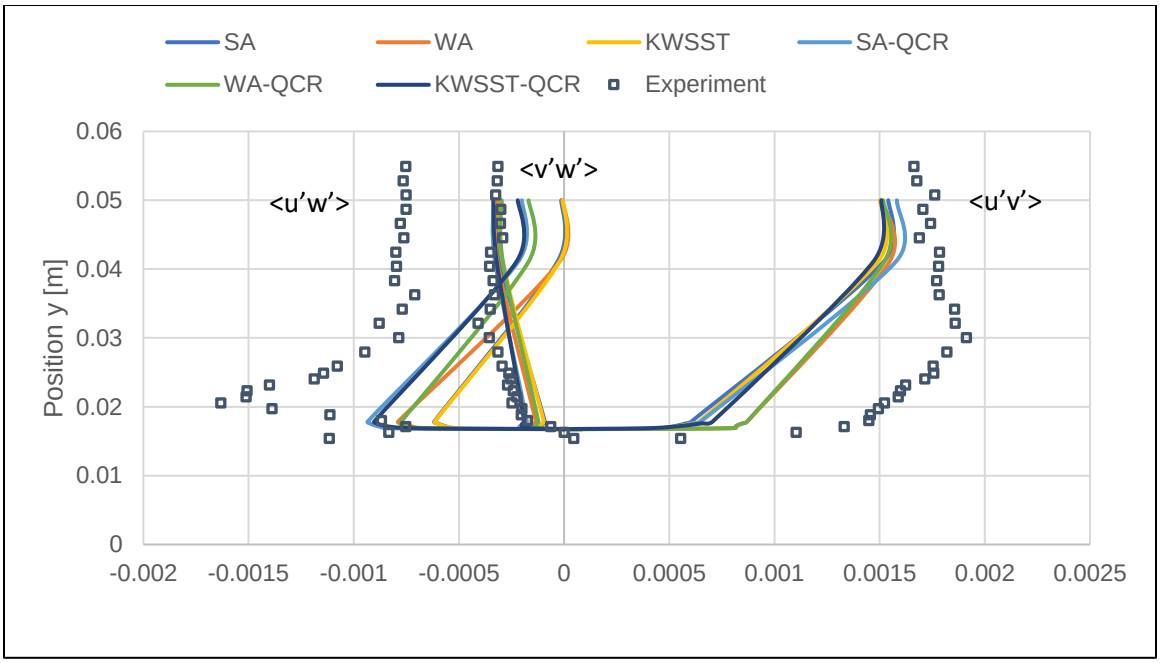

(a) α = -2.5°

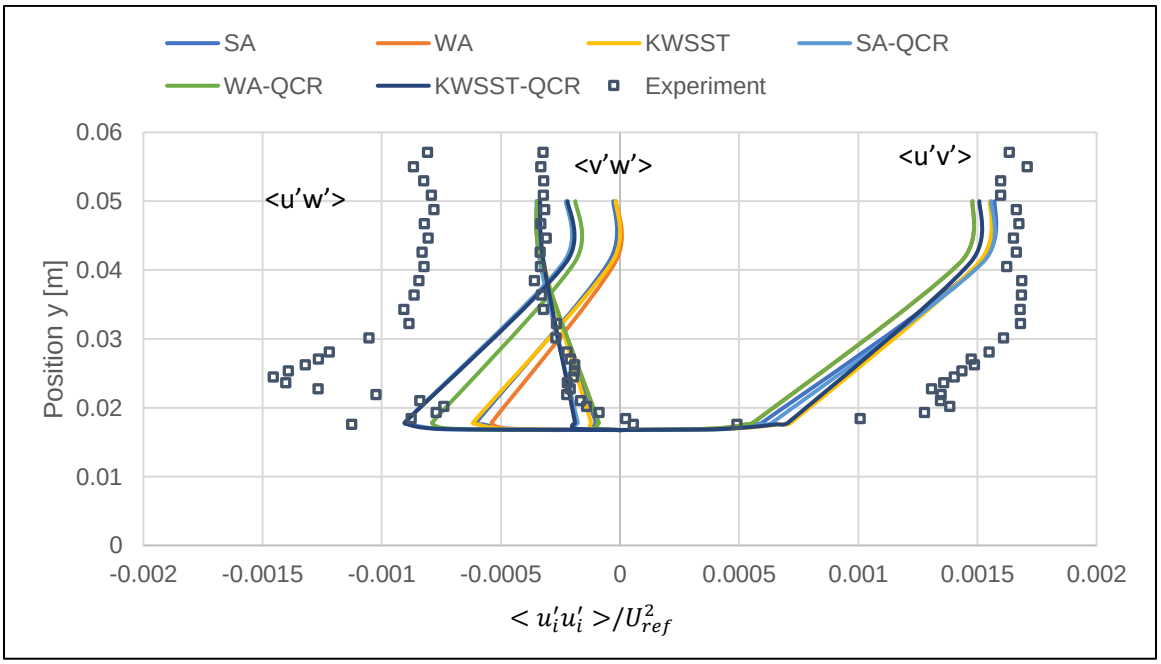

(b) α = 5°

Figure 5.17 Comparison of computed and experimental turbulent shear stress at X = 2747.6 mm, Y = -237.1 mm

5.2.4 Conclusions

Two one equation RANS turbulence models, Spalart-Allmaras (SA) and Wray-Agarwal (WA), and one two-equation model $k-\omega$ SST, were implemented for solution of the Reynolds-Averaged Navier-Stokes (RANS) equations in ANSYS Fluent to evaluate the flow separation characteristics in a wing-body juncture flow region. Each model was implemented both with and without the use of QCR. All models showed good results for pressure coefficient profiles relative to the wind tunnel data. The WA model yields comparable results to the SA model for the prediction of the separation size at the 0, -2.5, 5 and 7.5 degree angle of attack. The $k-\omega$ SST model demonstrated improved separation size prediction over the one-equation models. Each model showed improved Reynolds stress and separation size predictions with the implementation of QCR. The WA and WA-QCR models also demonstrated accuracy in solving velocity and Reynolds stress profiles upstream and near the separation point. The WA models predicted comparable separation lengths and widths and, in some cases, showed better Reynolds stress prediction.

5.3 ONERA M6

5.3.1 Physical Model

The ONERA-M6 test case based on the 1979 AR-138 AGARD Report has become an important and widely used validation case for transonic computational fluid dynamics simulations over a wing. It is also posted on NASA Turbulent Modeling Resource (TMR) website for evaluating the accuracy of various RANS turbulence models. Available wind tunnel pressure coefficient data allows for testing the ability of the numerical methods and turbulence models to accurately simulate the formation of shock waves and shock/turbulent boundary layer interactions at 3.06 and

6.06 degree angles of attack. Flow separation occurs at the higher angle of attack of 6.06 degree. In this study, two turbulence models are employed to simulate the flow field over ONERA-M6 wing. The turbulence models considered are the one equation Spalart-Allmaras (SA) and Wray-Agarwal (WA) model. Computations show that both turbulence models can simulate the flow field with good accuracy against the experimental data.

The ONERA-M6 wing was first introduced in the 1979 AGARD (NATO's Advisory group for Aerospace Research and Development) Report AR-138 titled "Experimental Data Base for Computer Program Assessment." The experimental data tabulated in the report was produced in the ONERA pressurized S2MA wind tunnel with free transition and a boundary layer diverter [31]. The only data reported for the series of wind tunnel experiments was pressure coefficient distributions at seven spanwise sections. Although data was collected for 30 aerodynamic conditions with Mach numbers ranging from 0.70 to 0.93 and angle of attack ranging from 0 to 6 degrees, two cases in particular have been the primary focus of computational fluid dynamic (CFD) research [31]. Both 3.06 and 6.06 degree of angle of attack at Mach 0.84 have been extensively used to validate the three-dimensional separated flow simulations using a variety of CFD solvers in 1980's and 1990's [32-36]. Since then, it has become a common standard CFD validation benchmark case for 3D external transonic flows. The lower angle of attack case demonstrates attached flow with a shock on upper surface of the wing, while the higher angle of attack case demonstrates extended flow separation in the outer portion of the wing towards the wing tip. The data for these two cases is presented as Case 2308 and 2565 respectively in AGARD report. The geometry of the original ONERA M6 wing documented by Schmitt and Charpin has a blunt trailing edge [37]; it is shown in Fig. 5.18.

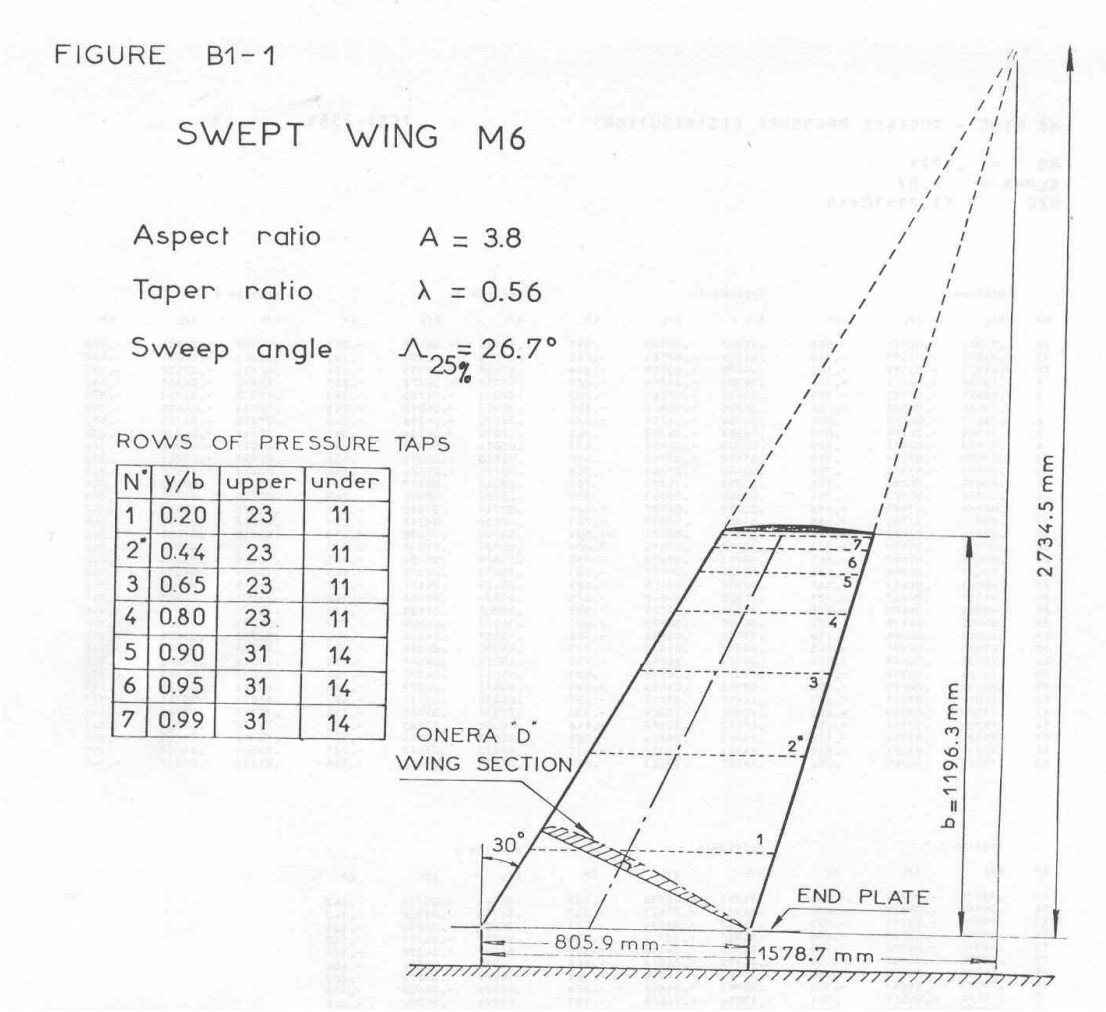

Figure 5.18 Layout of the ONERA M6 wing planform [38]

The ONERA M6 wing test case is a valuable tool for evaluating the ability of current CFD solvers, numerical methods, and turbulence models to accurately model the transonic flow regime. The shock wave formation due to local supersonic flow and boundary layer interaction are of particular interest. As velocity approaches the speed of sound, the compressibility effects increase. Unlike low velocity cases (Mach < 0.3), the density of air cannot be treated as a constant as it varies with respect to pressure and temperature. At the higher 6.06 degree angle of attack turbulent boundary layer separation also occurs toward the tip of the wing.

In recent years, a group at ONERA has created a modified geometry with a sharp trailing edge for the purpose of CFD validation. The geometry with sharp trailing edge has been recommended for the ONERA M6 CFD validation and has been provided at the NASA Turbulence Modeling Resources (TMR) website [36]. The wing used in this study is the ONERA M6 wing with a sharp trailing edge as described in NASA TMR. It is a swept, semi-span wing with no twist and has a symmetric airfoil. The simple geometry lends itself well in mesh generation and CFD validation of complex transonic flow characteristics including shock/boundary layer interaction using various numerical algorithms and turbulence models. Results for the 3.06 degree angle of attack case using a variety of flow solvers including FUN3D, CFL3D and USM3D have been published on NASA TMR [38]. The negative Spalart-Allmaras one equation turbulence model was recently used by NASA to compare the performance of different solvers and effect of grid size on the computations [39]. The results presented in this section were obtained using ANSYS Fluent by solving Reynolds-Averaged Navier Stokes (RANS) equations with two different turbulence models. The two RANS turbulence models tested are the Spalart-Allmaras (SA) and Wray-Agarwal (WA) one equation turbulence models. The WA model is a relatively new model which has been shown to be comparable to both the SA model and the k-omega SST model for a wide variety of flow conditions. Quantitative data consists of drag, lift and pressure coefficients for the purpose of comparison with both the wind tunnel data and existing CFD results with different grid densities and turbulence models.

5.3.2 Numerical Methods

A structured grid was used; it was created around the ONERA M-6 wing as shown in Fig. 5.19. It was created using the ANSYS ICEM software package. A hemispherical computational domain with symmetry plane and the Riemann far-field boundary conditions were employed following the

test case validation guidelines given on NASA TMR [36]. The structured grid was chosen for higher control of inflation layers in the near-wall region. An O-grid was generated and mesh in the near all region was refined such that $y^+ \leq 1$. The first layer height away from the wall of the wing was set at $1.0 * 10^{-6}\, m$ based on the Reynolds number of $14.6 * 10^6$ calculated at the root chord. A geometric growth rate of less than 1.2 was set for the cells in the O-grid. Present 3.06 degree angle of attack results were computed on a mesh with ~4,600,000 cells while the 6.06 degree angle of attack results were computed on a mesh with ~6,400,000 cells.

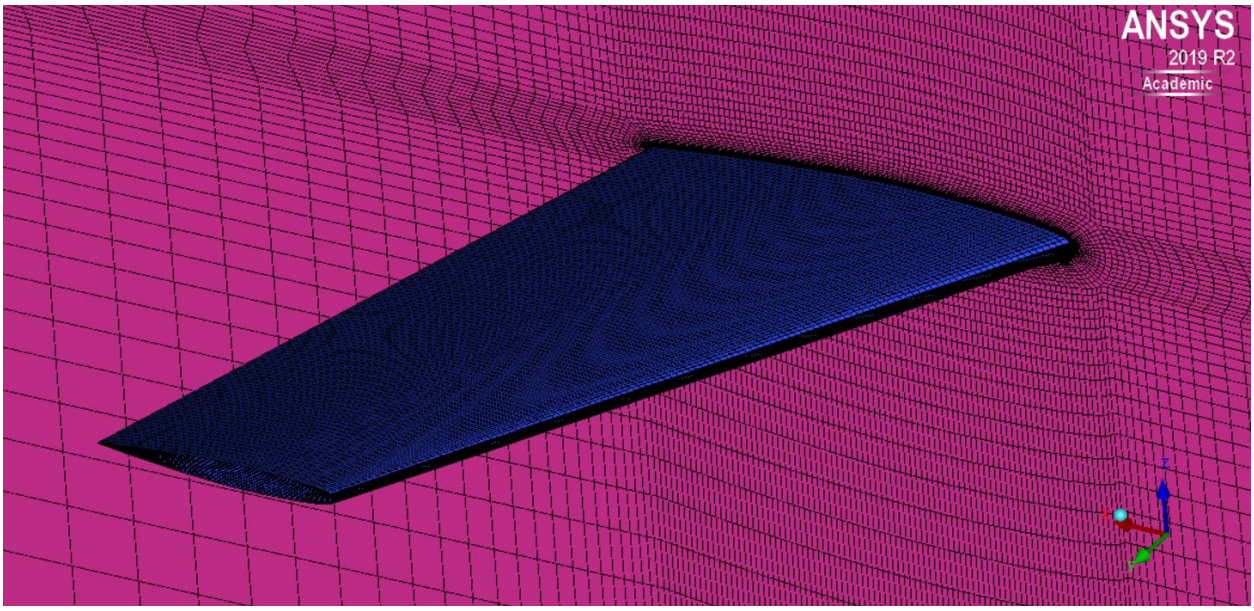

Figure 5.19 Structured mesh around the ONERA-M6

A pressure-based solver was used in CFD simulations. Boundary conditions were set in order to best match the wind tunnel experiments. A Mach number of 0.84 was used corresponding to a velocity at the far-field boundary of 288.12 m/s. It results in Reynolds number based on the mean aerodynamic chord of $11.72 * 10^6$. The ideal gas law was implemented due to compressibility effects in transonic flow. Thermal effects were calculated using energy equations. The viscosity was modeled using the three coefficient form of Sutherlands law based on the local temperature written as:

$$\mu = \mu_o \left(\frac{T}{T_o}\right)^{\frac{3}{2}} \left(\frac{T_o+S}{T+S}\right) \quad (5.1)$$

A least squares cell based method was implemented in order to calculate the pressure gradient. Second order upwind scheme was used for discretization of the convection terms and second-order central differencing was used for viscous terms in a finite-volume framework. The two turbulence models used are the Spalart-Allmaras model and the Wray-Agarwal model.

5.3.3 Results and Discussion

Computations were performed for transonic turbulent flow past ONERA M6 wing at 3.06 and 6.06 angles of attack using both the SA and WA model. Pressure coefficient plots were obtained at seven span-wise locations and were compared with wind tunnel data for the 3.06 degree angle of attack case. The comparison of drag and lift coefficient at α = 3.06 degree using SA, WA and SA-neg [38] models is shown in Table 5.4. It can be seen that the SA model results are slightly closer to the SA-neg model results from NASA-TMR [38]. The most difficult part of the simulation is computation of shock and shock/boundary layer interaction on the upper surface of the wing. Figure 5.22 show the pressure distribution on the wing which shows the shock location on the upper surface from wing root to wing tip. Figure 5.20 shows the computed coefficient of pressure for the 3.06 degree angle of attack case at seven span-wise locations of the wing using both SA and WA model and their comparison with experimental data. The x-locations are nondimensionalized by local chord. The WA model results for the pressure coefficient profiles are more accurate in capturing the shock comparable to those from SA model when compared to experimental data. Overall, both SA and WA model give comparable results. Figure 5.23 shows the computed pressure distribution for the 6.06 degree angle of attack case. Both models currently struggle to accurately model the outboard flow separation towards the tip of the wing. Pressure

coefficient analysis focuses on the inboard 80% of the wingspan for the 6.06 degree angle of attack case. Based on the first two pressure tap spanwise locations, the WA model shows a significant improvement in shock prediction location in comparison to the SA model at the higher angle of attack. At the higher span cross-sections, the SA model predicts shock too late while the WA model tends to predict the shock too early. Overall, the WA model shows better results for shock location prediction at the 6.06 degree angle of attack.

Table 5.4: ONERA M6 drag and lift coefficient predictions for the 3.06 degree angle of attack case

Turbulence Model	Drag Coefficient	Lift Coefficient
Spalart-Allmaras	0.0176	0.264
Wray-Agarwal	0.0178	0.261
Spalart-Allmaras-Neg [38]	~0.017	~0.27

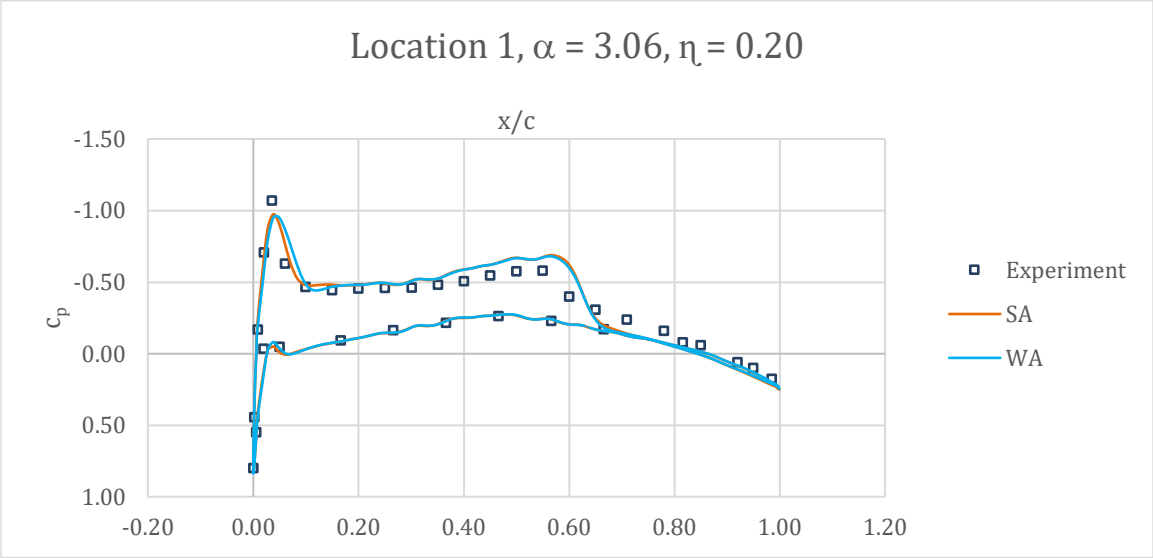

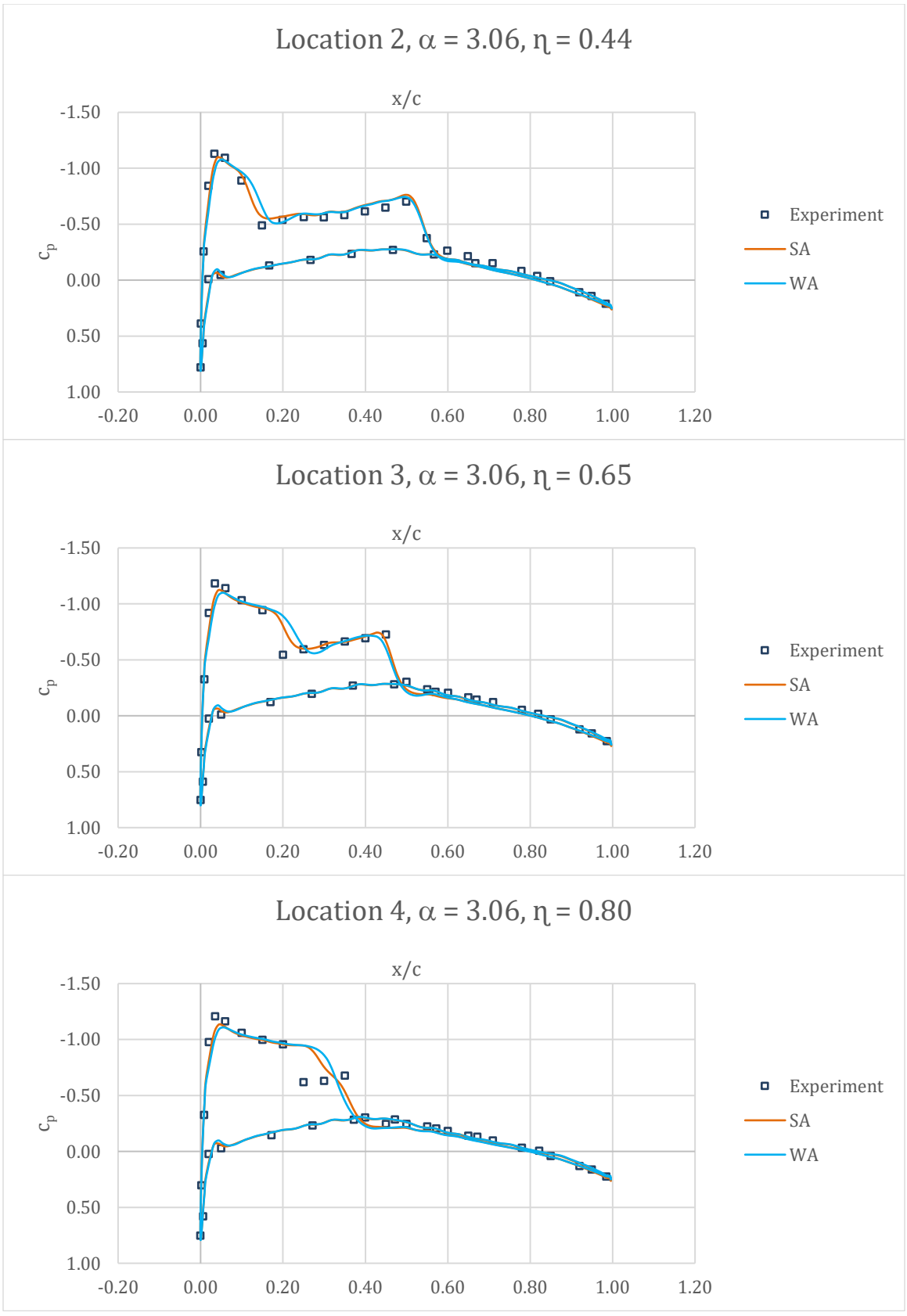
Location 2, α = 3.06, η = 0.44
x/c
-1.50
-1.00
-0.50
0.00
0.50
1.00
c_p
-0.20
0.00
0.20
0.40
0.60
0.80
1.00
1.20
Experiment
SA
WA
Location 3, α = 3.06, η = 0.65
x/c
-1.50
-1.00
-0.50
0.00
0.50
1.00
c_p
-0.20
0.00
0.20
0.40
0.60
0.80
1.00
1.20
Experiment
SA
WA
Location 4, α = 3.06, η = 0.80
x/c
-1.50
-1.00
-0.50
0.00
0.50
1.00
c_p
-0.20
0.00
0.20
0.40
0.60
0.80
1.00
1.20
Experiment
SA
WA

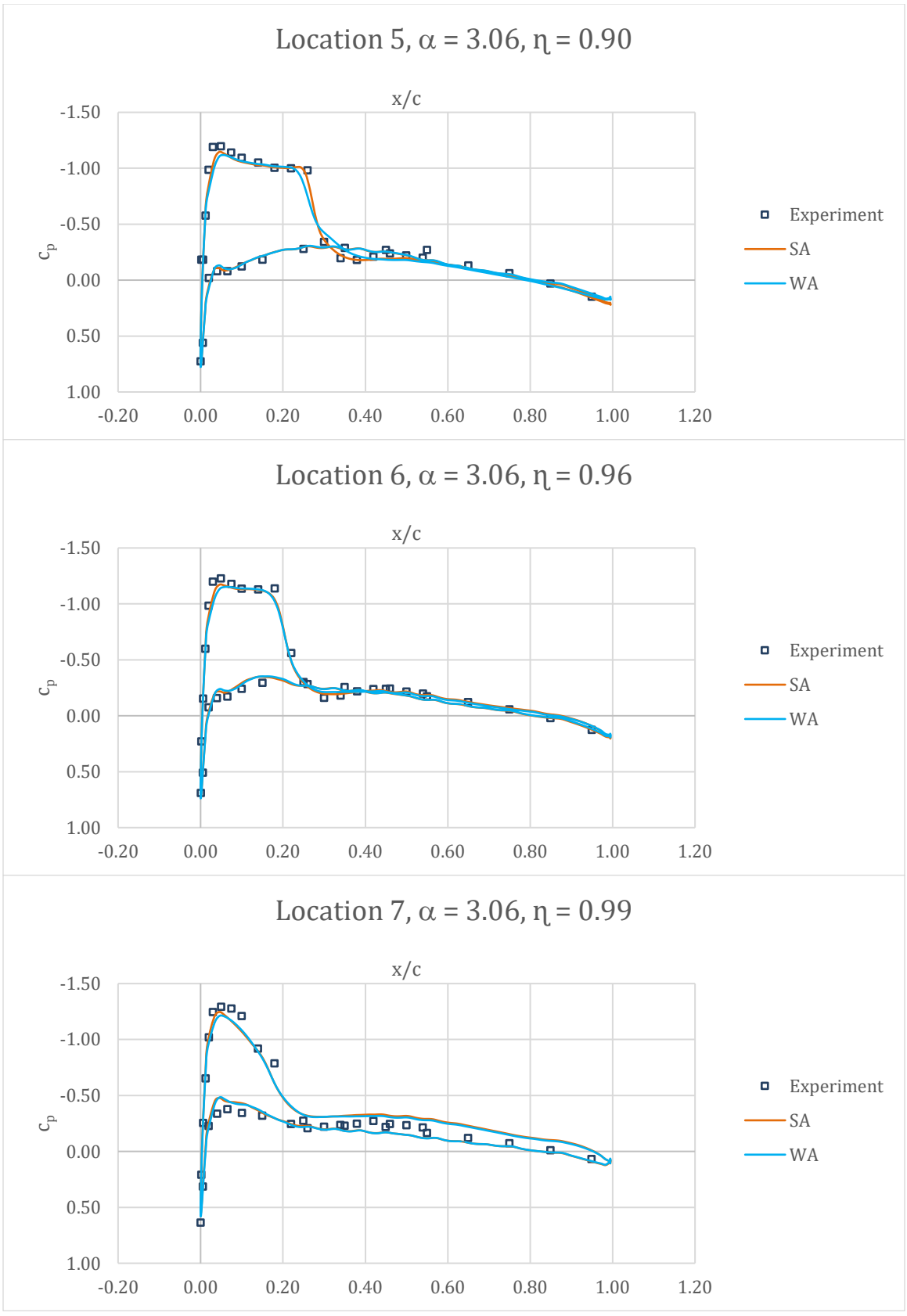

Figure 5.20 Comparison of pressure coefficient profiles at span-wise locations shown in Fig. 5.18 for α =3.06 º

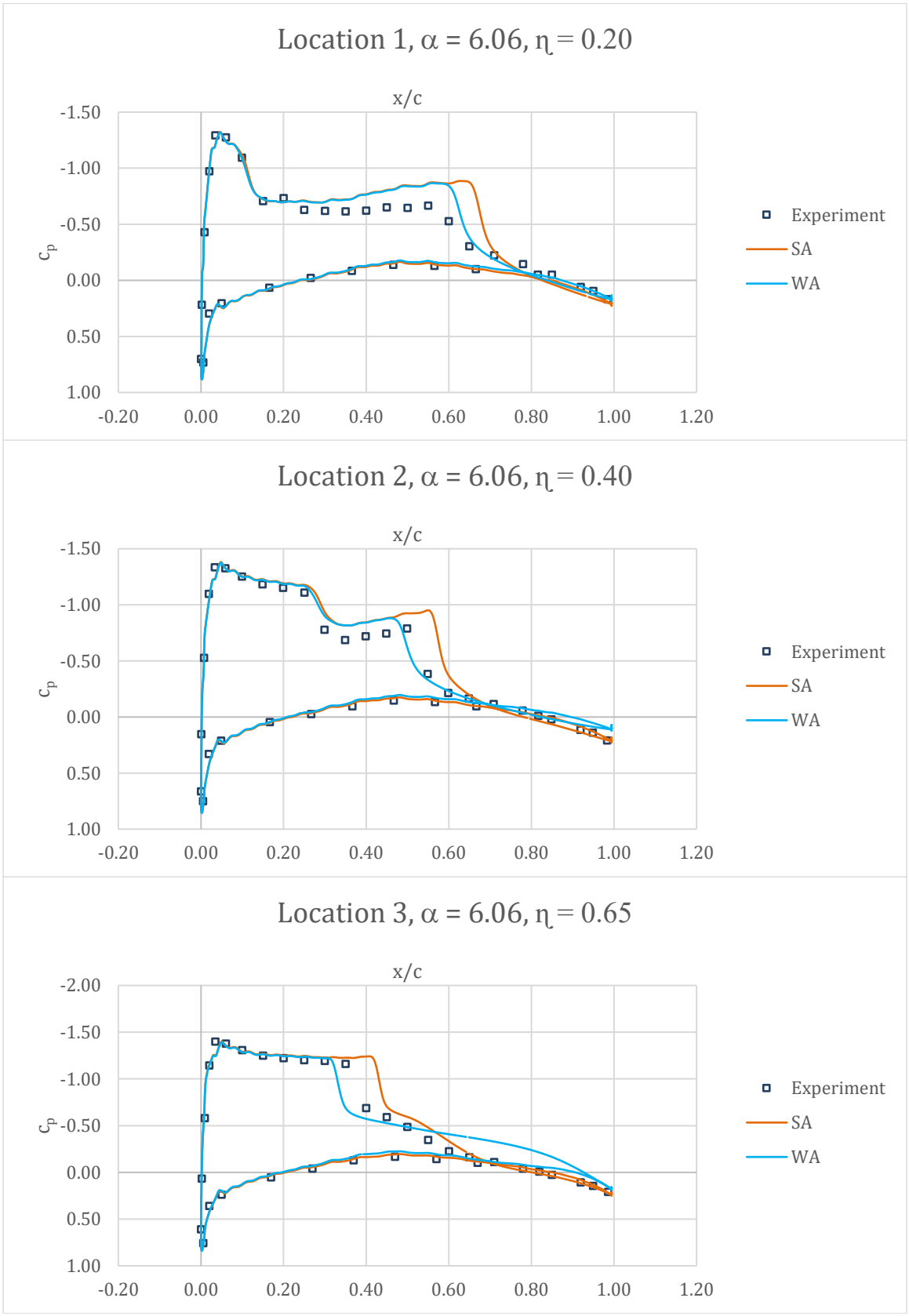
Location 1, α = 6.06, η = 0.20
x/c
-1.50
-1.00
-0.50
0.00
0.50
1.00
cp
-0.20
0.00
0.20
0.40
0.60
0.80
1.00
1.20
Experiment
SA
WA
Location 2, α = 6.06, η = 0.40
x/c
-1.50
-1.00
-0.50
0.00
0.50
1.00
cp
-0.20
0.00
0.20
0.40
0.60
0.80
1.00
1.20
Experiment
SA
WA
Location 3, α = 6.06, η = 0.65
x/c
-2.00
-1.50
-1.00
-0.50
0.00
0.50
1.00
cp
-0.20
0.00
0.20
0.40
0.60
0.80
1.00
1.20
Experiment
SA
WA

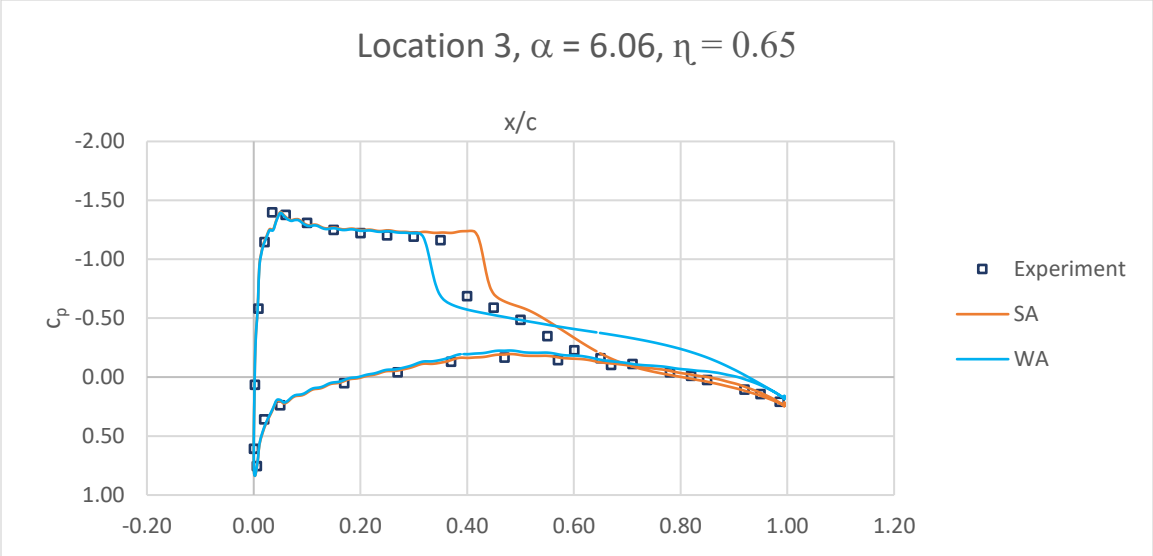

Figure 5.21 Comparison of pressure coefficient profiles at span-wise locations shown in Fig. 5.18 for α =6.06 º

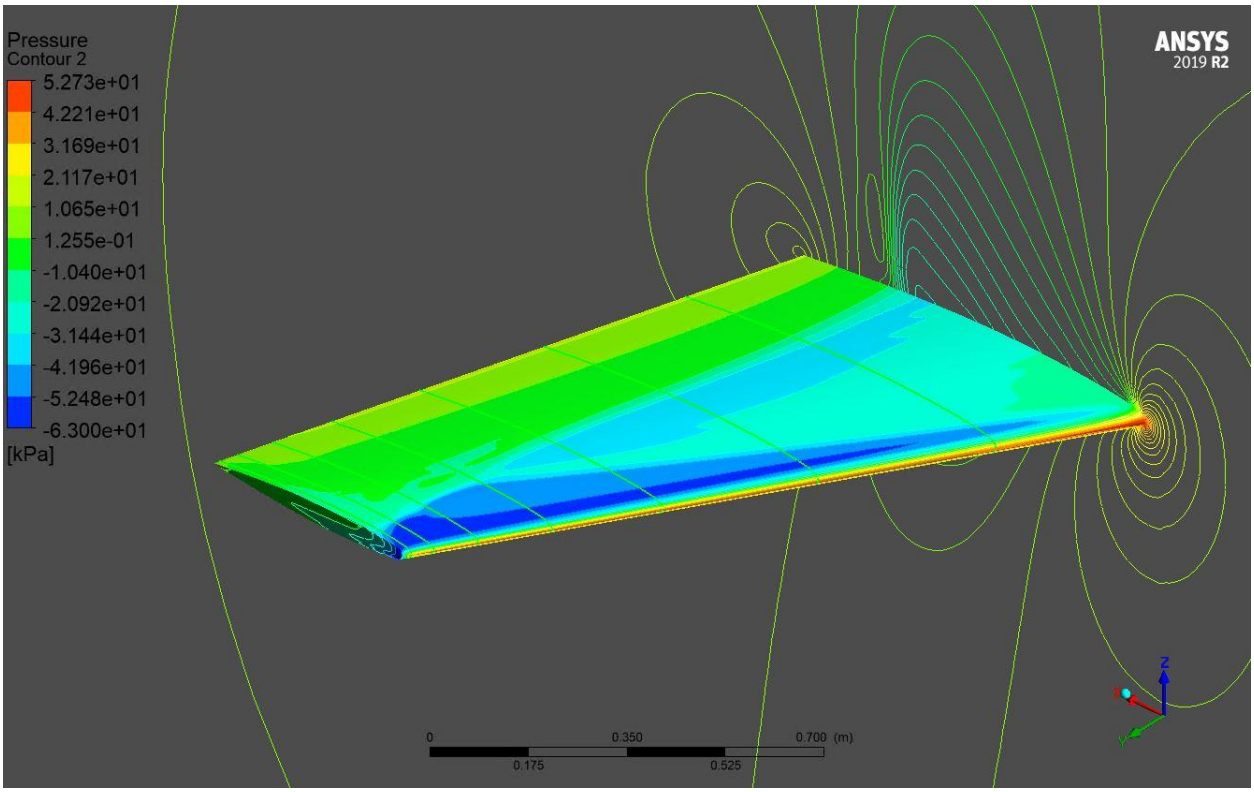

Figure 5.22 Pressure contours on the surface of the ONERA M6 wing, α = 3.06º

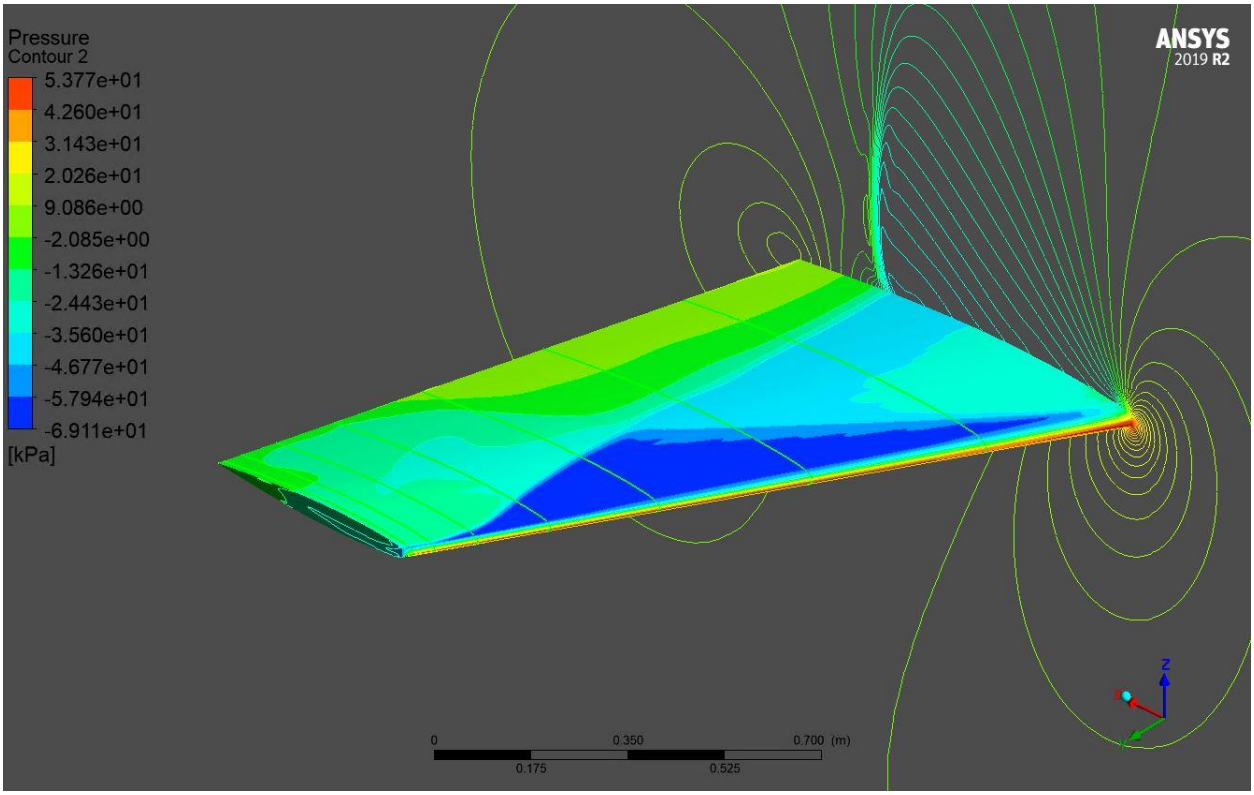

Figure 5.23 Pressure contours on the surface of the ONERA M6 wing, α = 6.06º

5.3.4 Conclusions

Two one-equation turbulence models, namely the SA and WA model are employed to simulate the flow field over an ONERA-M6 wing at Mach 0.84 and Reynolds number based on the mean aerodynamic chord of $11.72 * 10^6$ at angles of attack of 3.06 and 6.06 degree. Computations show that both turbulence models can simulate the flow field with good accuracy against the experimental data; however, the WA model is slightly more accurate in capturing the shock location and overall pressure distribution. Further analysis of numerical methods is necessary to capture shock location in the case of extended flow separation towards the tip of the wing for α = 6.06º.

Chapter 6: Co-Flow Jet

This chapter describes the application and numerical simulation of Active Flow Control (AFC) by a Co-Flow Jet (CFJ) to airfoils and wings to improve their aerodynamic performance.

6.1 Baseline RAE 2822

6.1.1 Physical Model

The RAE 2822 airfoil is used as the baseline airfoil for the development of the Co-Flow Jet technology. The RAE 2822 is a supercritical airfoil characterized by a lower profile surface along the suction side that minimizes shockwaves and drag. It has become a standard test case for turbulence modeling validation and active flow control development due to a wealth of experimental data tabulated in AGARD Report AR 138 [40]. The geometry and parameters of the RAE 2822 for experimental case 9 are shown in Fig. 6.1 and Table 6.1.

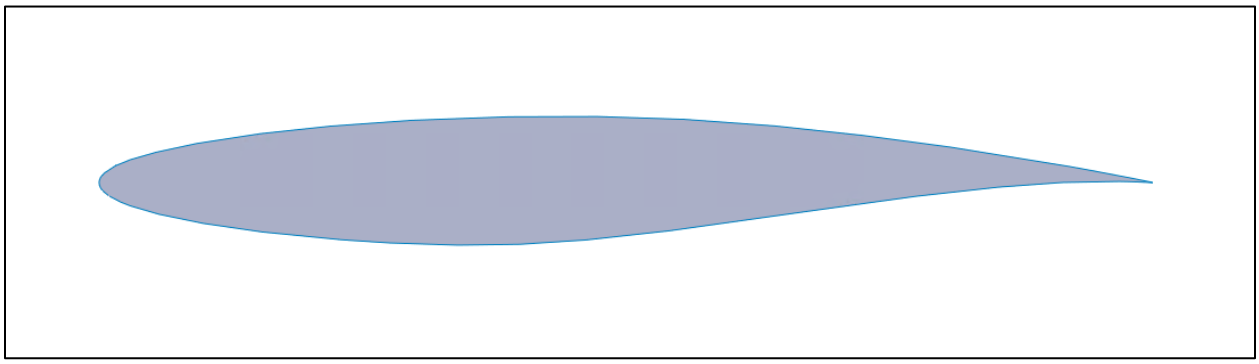

Figure 6.1 RAE 2822 airfoil geometry

Table 6.1 RAE 2822 airfoil geometry parameters

	RAE 2822
Max Thickness	12.1% at 37.9% chord
Max Camber	1.3% at 75.7% chord
Chord Length	2 ft
Angle of Attack	3.19°

In this work, experimental case 9 is simulated. It is a subcritical transonic flow case with minimal separation downstream of the shock position. A parametric study was setup in order to run simulations of the RAE2822 airfoil sweeping through angles of attack ranging from 0 to 5°. A circular 2D domain was generated with a far-field radius of 20 chord lengths about the airfoil. A freestream Mach number of 0.73 was chosen corresponding to Reynolds number of approximately $6.5 * 10^6$.

6.1.2 Numerical Methods

The compressible RANS equations are solved using a pressure based solver and the SA turbulence model. The ideal gas law is used to calculate density while Sutherland's law is used to calculate the viscosity. The pressure velocity relationship is defined by the coupled scheme. Second order discretization is used for all of the spatial terms. The Green-Gauss node based discretization scheme is used. An unstructured grid is generated as shown in Fig. 6.2. The grid parameters are provided in Table 6.2.

Table 6.2 RAE 2822 airfoil mesh parameters

	Mesh
Cells	70805
Y^+	<1.0
Initial Wall Spacing (m)	$1.0 * 10^{-6}$

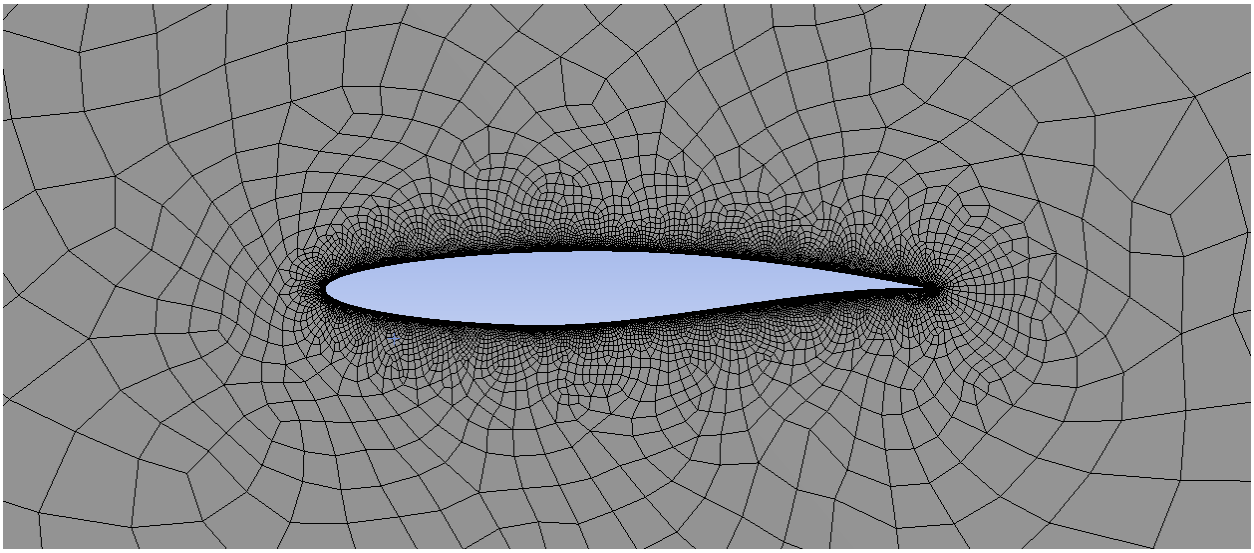

Figure 6.2 Unstructured grid around the RAE 2822 airfoil

6.1.3 Results and Discussion

Simulation results for the 3.19° angle of attack are compared to wind tunnel data. As shown in Table 6.3, the simulation overpredicts the lift and drag of the RAE 2822 relative to the experimental data. This is in part due to the limitations of RANS models to handle shock wave/ boundary layer interaction. The deviation from the experiment is consistent with the computational results of Ge-Cheng Zha and several other research groups [7][41][42].

Table 6.3 RAE 2822 airfoil aerodynamic coefficient comparison

	Lift Coefficient	Drag Coefficient
Wind Tunnel [7]	0.803	0.0168
Spalart-Allmaras	0.820	0.0225
Spalart-Allmaras (Zha et al.) [7]	0.820	0.0232

Figure 6.3 shows the computed coefficient of pressure for the 3.19 degree angle of attack case using the SA model and its comparison with the experimental data. The x-locations are nondimensionalized by the chord length. From the pressure coefficient profile, it can be seen that the simulation accurately predicts the shock location on the upper suction surface of the wing. The shock wave can be further visualized in the Mach contours shown in Fig. 6.4. With a freestream

Mach number of 0.73, the RAE 2822 has a peak Mach number in the supersonic region of 1.258. It can also be noted that flow returns to subsonic after the shock wave on the supercritical airfoil.

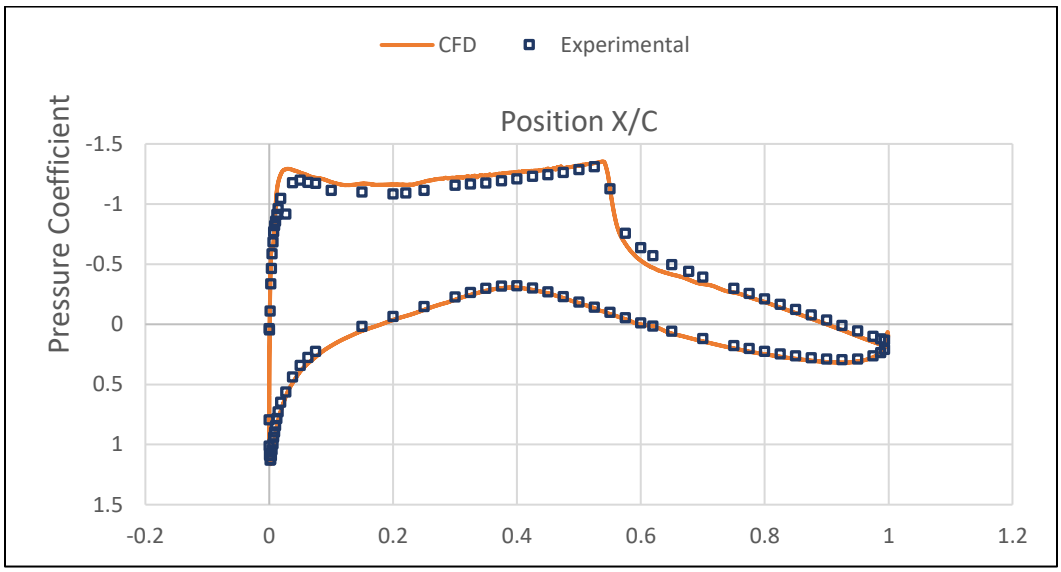

Figure 6.3 Computed RAE 2822 airfoil pressure coefficient profile compared to experimental data [7]

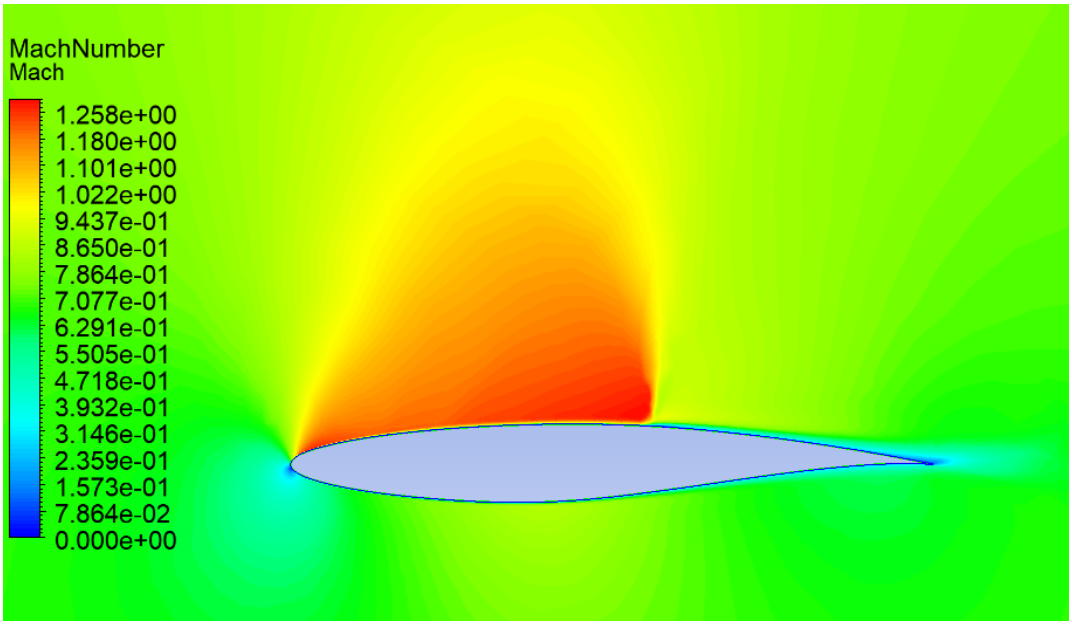

Figure 6.4 RAE 2822 airfoil Mach contours plot for α = -3.19°

Drag and lift coefficient results for the range of angles of attack are calculated to and compared to published CFD results. It can be seen from Figs. 6.5 and 6.6 that the simulation results match

closely with those of Zha et al. for both the lift and drag with minor deviations at the higher angles of attack.

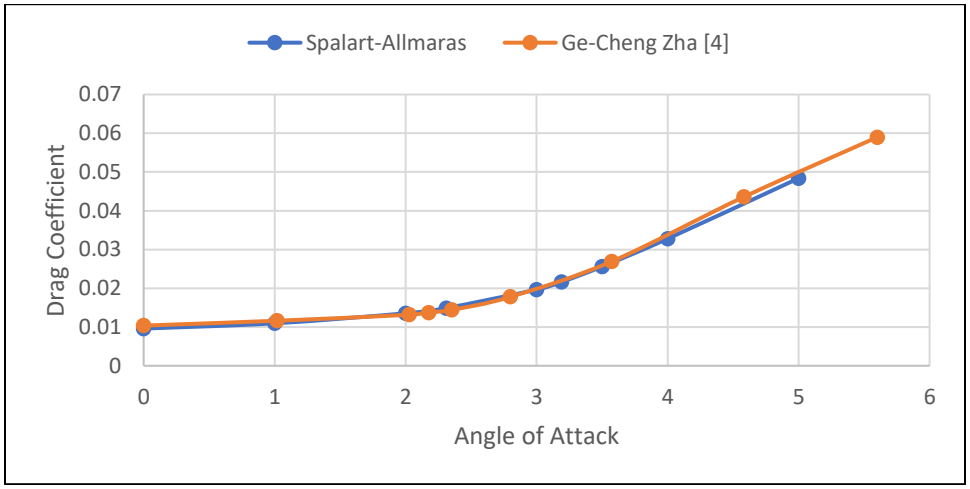

Figure 6.5 RAE 2822 drag coefficient variation with angle of attack.

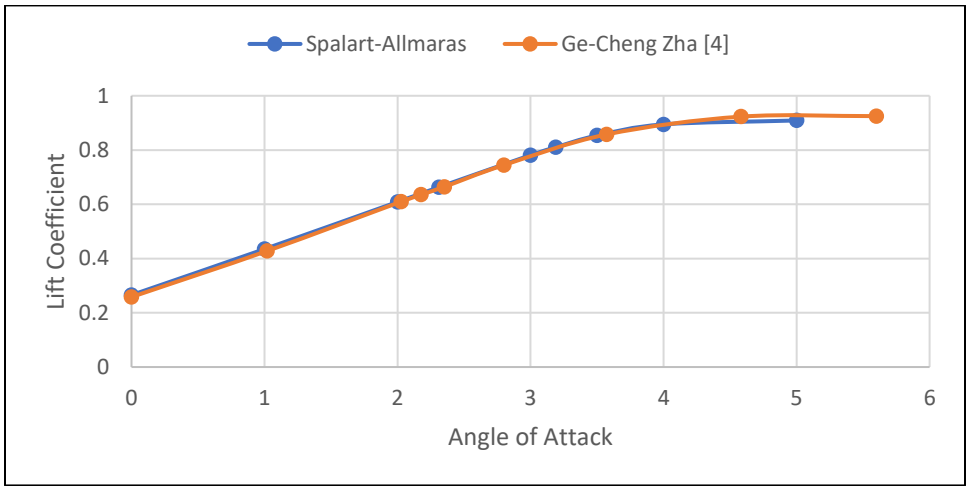

Figure 6.6 RAE 2822 lift coefficient variation with angle of attack.

6.1.4 Conclusion

The Spalart-Allmaras turbulence model was used to compute the flow around the RAE 2822 supercritical airfoil in transonic flow. The CFD analysis slightly overpredicted lift and significantly overpredicted drag relative to the experimental results. The simulation successfully predicted the location of the shockwave along the suction surface of the airfoil. The lift and drag are however

consistent with the work of other research groups and the discrepancy in matching the experimental data is due to difficulties in modeling the shock/ boundary layer interaction in the simulation. Further improvements in numerical methods and turbulence modeling are necessary to match wind tunnel results more accurately for complex transonic flow cases.

6.2 Baseline Co-Flow Jet

6.2.1 Physical Model

The baseline airfoil geometry simulated is the RAE 2822 with the addition of the leading edge injection slot and the trailing edge suction slot. For the initial validation case the injection slot location is at 3% of the chord length and the injection slot location is at 70% of the chord length. A separate case was simulated with the injection slot located at 12% of the chord length. This was done to evaluate the viability of moving the injection slot further from the leading edge to avoid potential redesign of wing front spar structures. For each case, both slots have a width of 0.6% of the chord. There is no shear surface translation, and the injection slot is designed to be tangent to the suction surface. The purpose of this model is to validate the boundary conditions and mesh methods for the CFJ against other CFD results prior to scaling and implementing the CFJ into the 2D TTBW airfoil and full 3D TTBW.

6.2.2 Numerical Methods

The numerical methods and flow conditions for the CFJ simulation match those of the RAE 2822 airfoil with the exception of the slot geometry and boundary conditions. The injection and suction slots are modeled as a pressure inlet and a pressure outlet respectively. The initial pressure was calculated corresponding to a momentum coefficient of 0.005. The equation for the momentum coefficient can be written as:

$$C_\mu = \frac{\dot{m}V_j}{\frac{1}{2}\rho_\infty V_\infty^2 S} \tag{6.1}$$

An unstructured grid was generated as shown in figure 6.7. The addition of the slot geometry resulted in a mesh size of approximately 108,000 elements. The injection and suction slots were modeled as a separate region to keep the mesh around the airfoil consistent with the case without CFJ. This also allowed for further refinement of the mesh around the slot openings.

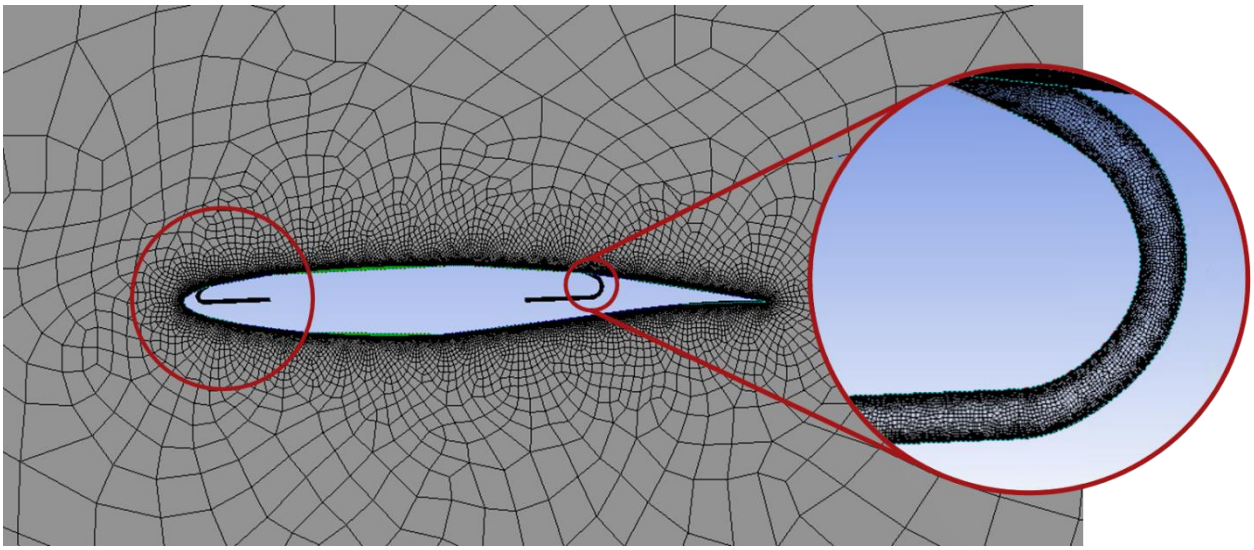

Figure 6.7 Unstructured grid around the CFJ-RAE 2822 airfoil

After running the simulations, additional post-processing was needed to account for the reactionary forces caused by the momentum exchange and pressure difference at the injection and suction slots. These forces can be obtained through control volume analysis [7]. The lift and drag due to the jet momentum can be written as:

$$R_x = \left(\dot{m}_j V_{j1} + p_{j1}A_{j1}\right)cos(\theta_1 - \alpha) - \left(\dot{m}_j V_{j2} + p_{j2}A_{j2}\right)cos(\theta_2 + \alpha) \tag{6.2}$$

$$R_y = \left(\dot{m}_j V_{j1} + p_{j1}A_{j1}\right)sin(\theta_1 - \alpha) + \left(\dot{m}_j V_{j2} + p_{j2}A_{j2}\right)sin(\theta_2 + \alpha) \tag{6.3}$$

where x and y represent the directions of lift and drag, subscripts 1 and 2 refer to the injection and suction slot, θ_i is the angle between the injection or suction slot surface and the line normal to the

airfoil chord and α is the angle of attack. The total lift and drag on the CFJ airfoil can then be written as:

$$D = F_x - R_x \tag{6.4}$$

$$L = F_y - R_y \tag{6.5}$$

where F_x and F_y are the drag and lift forces obtained through the surface integral of pressure and shear stress. The lift and drag coefficients can then be calculated with the total lift and drag accounting for the jet reactionary forces. The energy consumption of the co-flow jet is accounted for by converting the power consumption into a corresponding drag force as follows:

$$\left(\frac{L}{D}\right)_C = \frac{L}{D+\frac{P}{V_\infty}} = \frac{C_L}{C_D+P_C} \tag{6.6}$$

where C_L and C_D are the lift and drag coefficients respectively.

6.2.3 Results and Discussion

Mach contours of the CFJ-RAE 2822 at the 3.19° angle of attack are shown in Fig. 6.8. The addition of the CFJ generates a higher supersonic Mach number than the baseline RAE 2822 and induces greater expansion on the suction surface. The peak shock wave Mach number is greater than 1.3 which presents a risk of high entropy and wave drag rise. It has been shown that suction surface translation can reduce this peak Mach number to an acceptable value [7].

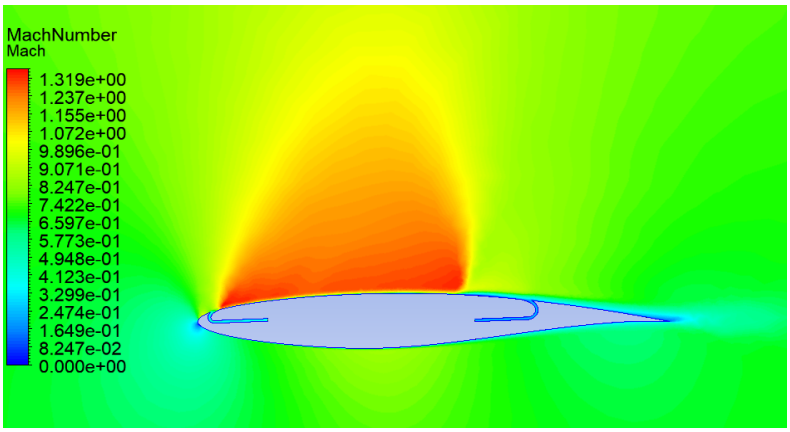

Figure 6.8 CFJ-RAE 2822 airfoil Mach contours plot α = -3.19°

Simulation results for the CFJ-RAE 2822 are compared with the CFD results of Zha et. al [7]. The lift and drag coefficient comparison is shown in Figs. 6.9 and 6.10. The computed lift and drag coefficients match closely with the published results. Although both simulations use the SA turbulence model, the results by Zha et. Al [7] employed higher order discretization methods, namely the 5th order weighted essentially non-oscillatory (WENO) scheme with a low diffusion Riemann solver for inviscid fluxes and a 4^{th} order central differencing scheme for the viscous terms. It can be seen from Fig. 6.10 that there is a significant increase in drag when the injection slot is shifted back to the 12% position. The 3% location is used for the rest of this work. Physical implementation of the CFJ into a TTBW will require a balance between aerodynamic performance and structural requirements.

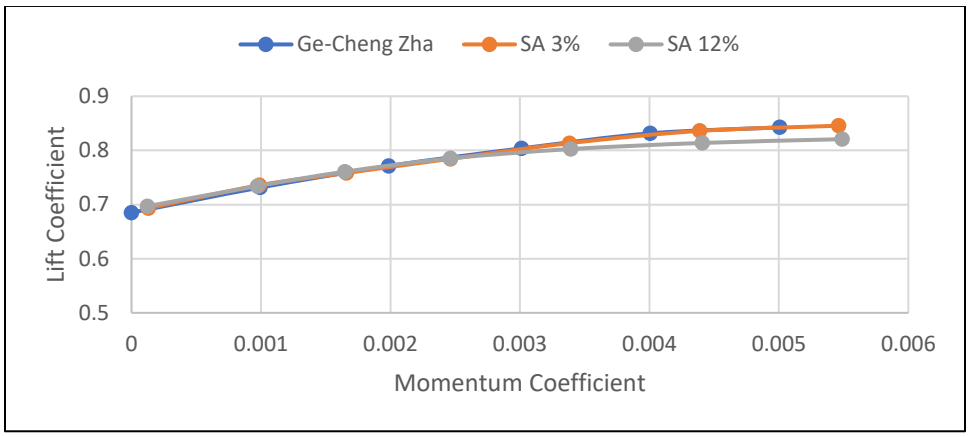

Figure 6.9 CFJ-RAE 2822 airfoil lift coefficient variation with momentum coefficient

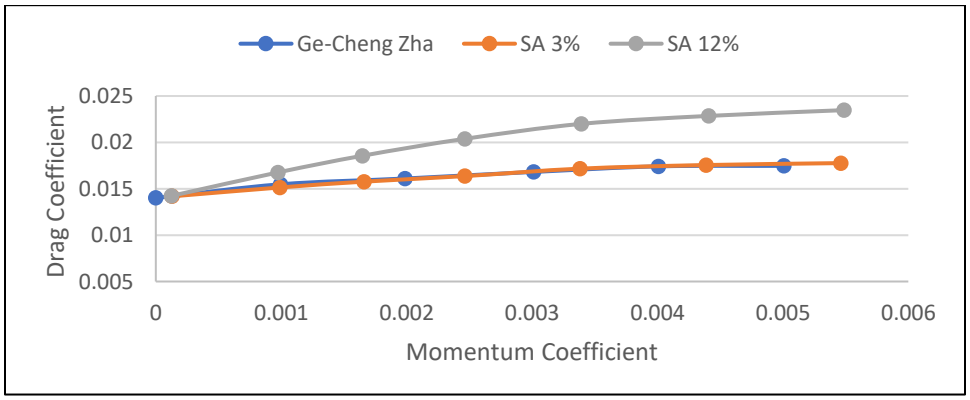

Figure 6.10 CFJ-RAE 2822 airfoil drag coefficient variation with momentum coefficient.

It can be seen from Fig. 6.11. that the simulation results match the scale of the published power coefficient values but do to not fully match the trend. The simulation methodology used yields a reasonable energy estimate which can be used to predict the feasibility of further CFJ designs Furthermore, when the injection slot is shifted away from the leading edge, the power coefficient increases due to a change in pressure ratio. From an energy perspective, it is ideal to keep the injection slot located at the suction peak closer to the leading edge. Fig. 6.12 shows the CFJ-RAE 2822 airfoil corrected lift-to-drag ratio variation with momentum coefficient.

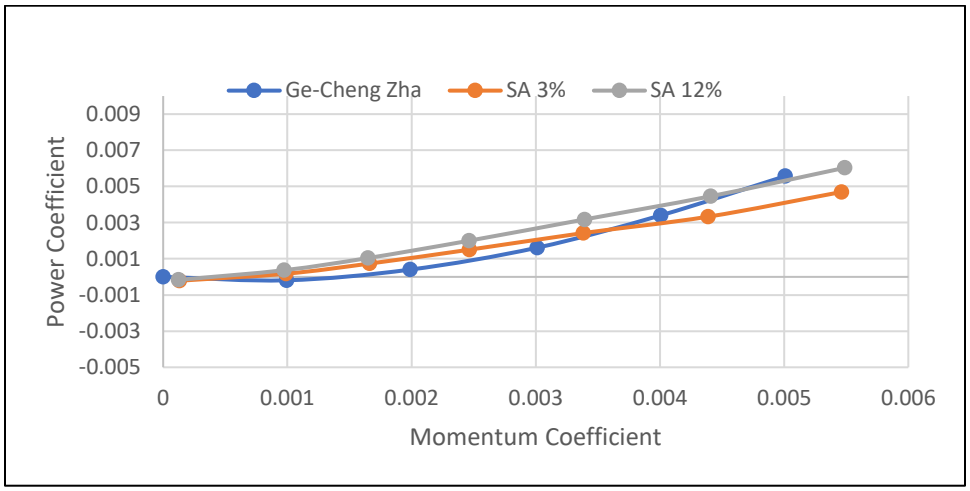

Figure 6.11 CFJ-RAE 2822 airfoil power coefficient variation with momentum coefficient

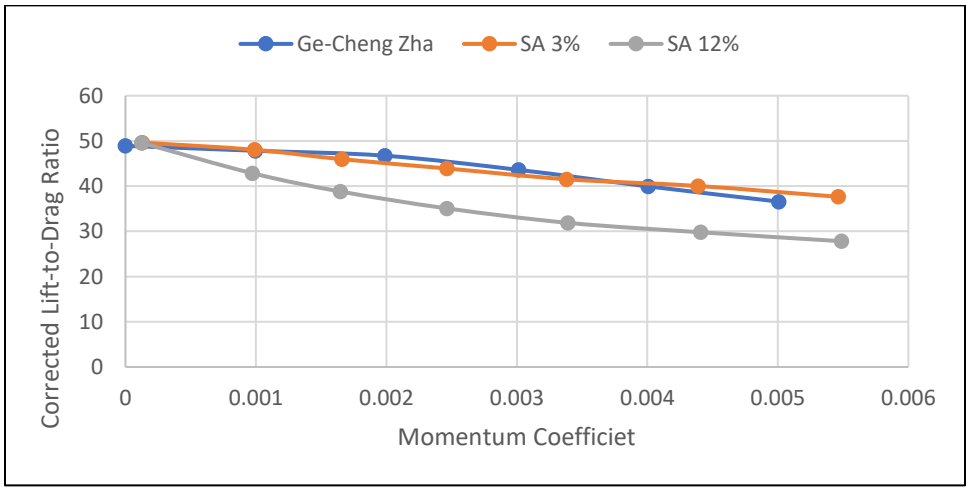

Figure 6.12 CFJ-RAE 2822 airfoil corrected lift-to-drag ratio variation with momentum coefficient

6.2.4 Conclusions

This test case validates the numerical methods, boundary conditions and mesh methods implemented in ANSYS Fluent to simulate a CFJ airfoil. The simulation results closely match the lift and drag curves of Zha et al. [7] and yield a reasonable power estimation. The methodologies are thus viable to be implemented in other configurations for further work. It is also shown that translation of the slot further from the leading edge suction peak results in higher drag and power consumption.

6.3 Scaled RAE 2822

6.3.1 Physical Model

After the validation test cases, the RAE2822 airfoil is then scaled from a chord length of 2 ft to the crank chord of 9.6 ft) of the SUGAR IV TTBW. The simulation boundary conditions are adjusted to the average pressure and temperature conditions for a cruise altitude of 35,000 feet. A circular 2D domain was generated with a far-field radius of 20 chord lengths about the airfoil. Similar to the 2ft chord test case, a parametric study is setup in order to run simulations of the scaled RAE2822 airfoil sweeping through angles of attack ranging from 0 to 5°. This sweep was performed at the cruise Mach speed for the Sugar IV and Sugar III, 0.8 and 0.745 respectively. This test case was run in order to provide a baseline for the scaled CFJ airfoil and evaluate the effect of geometric and boundary conditions changes on the optimal angle of attack.

6.3.2 Numerical Method

The numerical methods used is the same as described in subsection 6.1.2. The compressible RANS equations are solved using a pressure based solver and the SA turbulence model. The ideal gas law is used to calculate density while Sutherland's law is used to calculate the viscosity. The pressure

velocity relationship is defined by the coupled scheme. Second order discretization is used for all of the spatial terms. The Green-Gauss node based discretization scheme is used. A grid independence study is performed to ensure that the simulation results are not affected by the quality of the grid. Three unstructured grids are generated using the same meshing techniques as described in subsection 6.1.2 with the inflation layers scaled to the flow conditions. Table 6.4 shows the properties of the three grids. The y+ value is varied from 1 to 4/9 and the mesh density is increased in order to evaluate its effect on the CFD simulation results.

Table 6.4 Scaled RAE 2822 airfoil grid independence study

Grid	Cells	y+	First Layer Height [m]
Coarse	251,292	1	1.73e-6
Medium	455,194	2/3	1.15e-6
Fine	764,385	4/9	7.69e-7

Figures 6.13 and 6.14 show the computed lift and drag coefficients respectively for each grid size. It can be seen that the computed aerodynamic coefficients have very little variation with respect to the grid density and inflation layer sizing. This process is implemented throughout the simulations along with evaluation of the skewness and orthogonality quality in order to minimize the grid sensitivity.

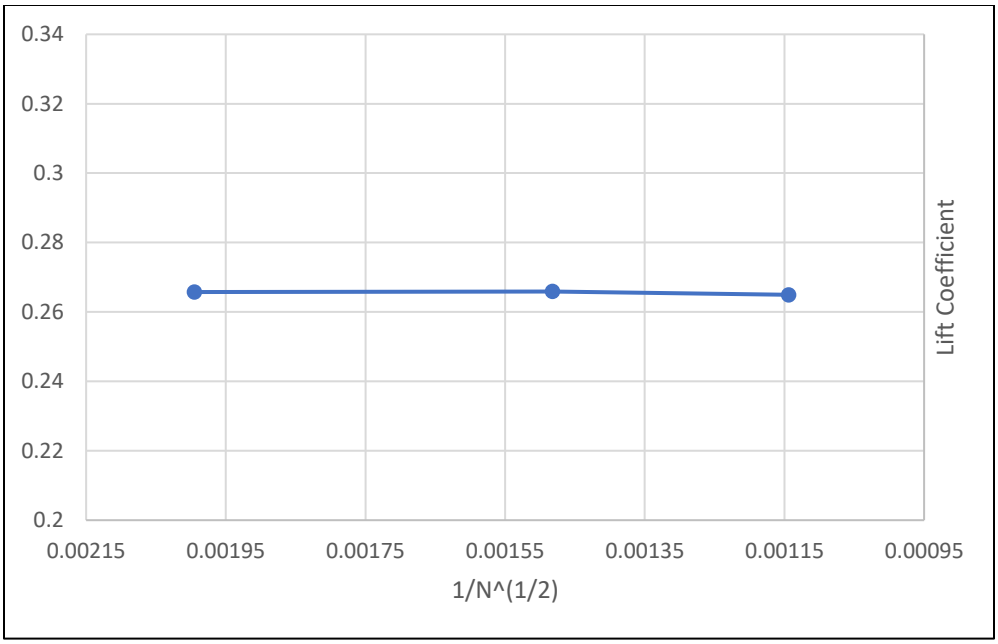

Figure 6.13 Scaled RAE 2822 airfoil lift coefficient variation with mesh density

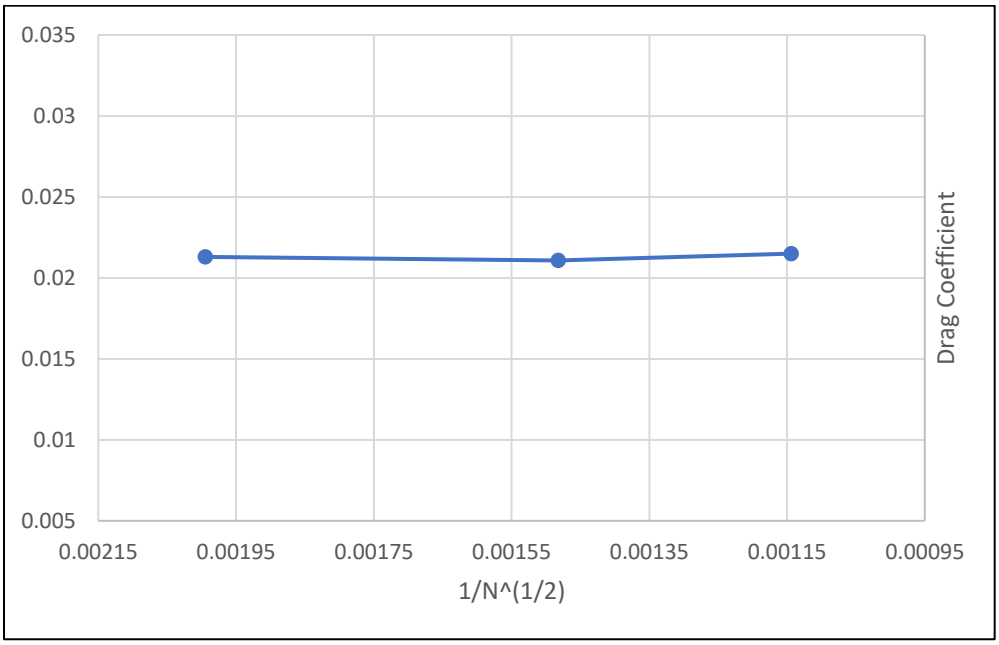

Figure 6.14 Scaled RAE 2822 airfoil drag coefficient variation with mesh density

6.3.3 Results and Discussion

Results for the scaled RAE2822 airfoil are compared between the two transonic Mach numbers of 0.745 and 0.8. These results are also plotted against the simulation results for the 2ft chord baseline

test case run at Mach 0.73. The lift coefficient at different angles of attack is shown in Figure 6.9. It can be seen that the scaled RAE2822 airfoil has a higher lift coefficient for the Mach 0.745 case than at Mach 0.8. The scaled airfoil at Mach 0.745 has comparable lift and drag coefficient curves to the baseline Mach 0.73 case as shown in Figs. 6.15 and 6.16. The scaled airfoil produces greater lift and drag, but these coefficients are also affected by the larger reference area, greater freestream speed and lower density air at higher altitudes. The scaled airfoil at Mach 0.8 also reflects a significant increase in total drag in comparison to the scaled airfoil at Mach 0.745 due an increase in the wave drag component. The improved aerodynamic performance for the scaled RAE2822 airfoil at Mach 0.745 is reflected in the higher lift to drag ratio shown in Figs. 6.17 and 6.18.

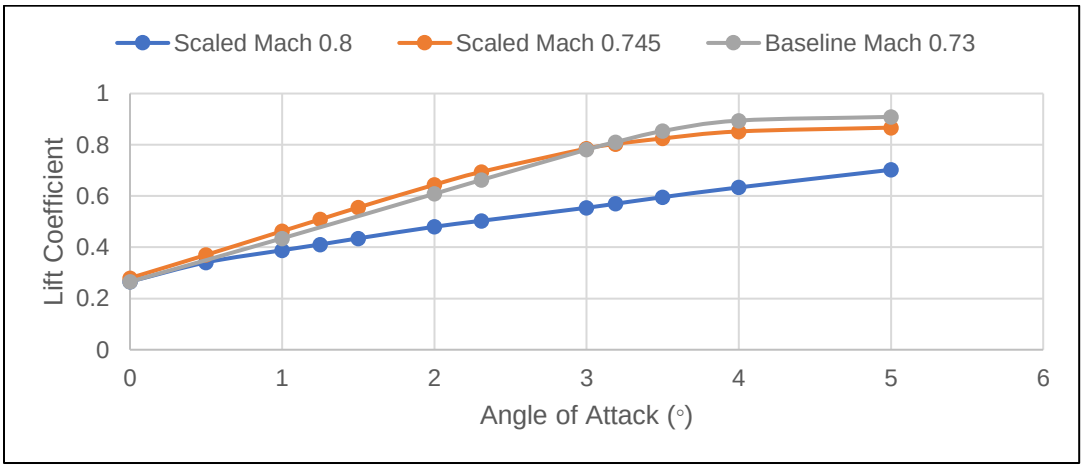

Figure 6.15 Scaled RAE 2822 airfoil lift coefficient variation with momentum coefficient

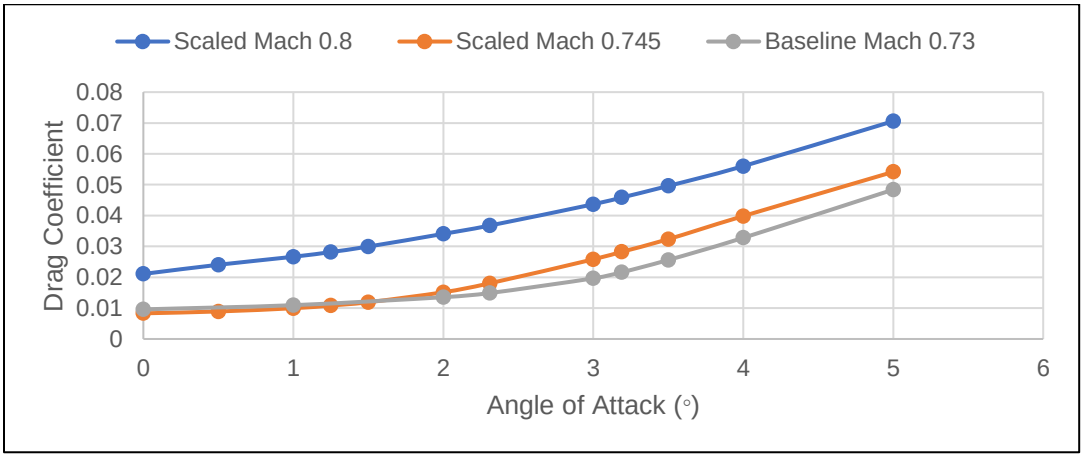

Figure 6.16 Scaled RAE 2822 airfoil drag coefficient variation with momentum coefficient

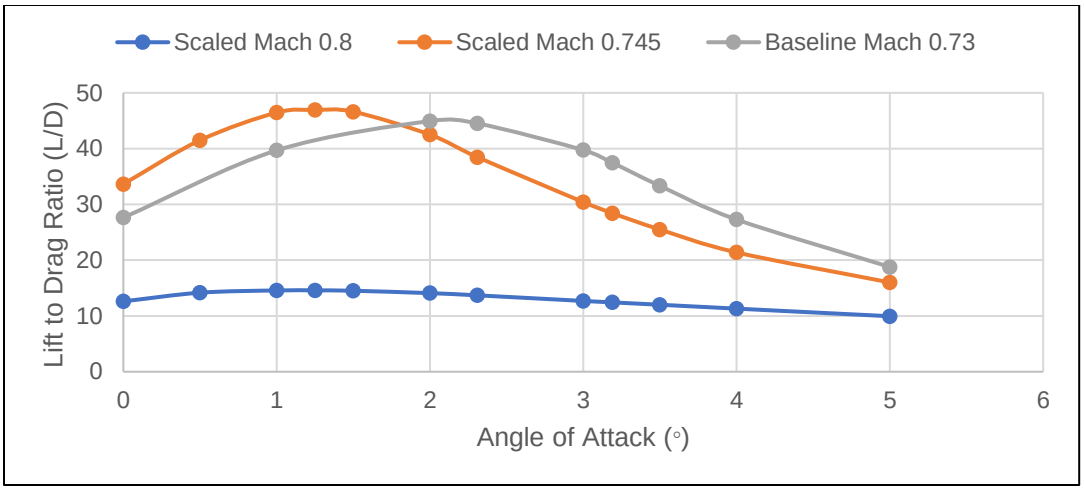

Figure 6.17 Scaled RAE 2822 airfoil lift-to-drag ratio variation with momentum coefficient

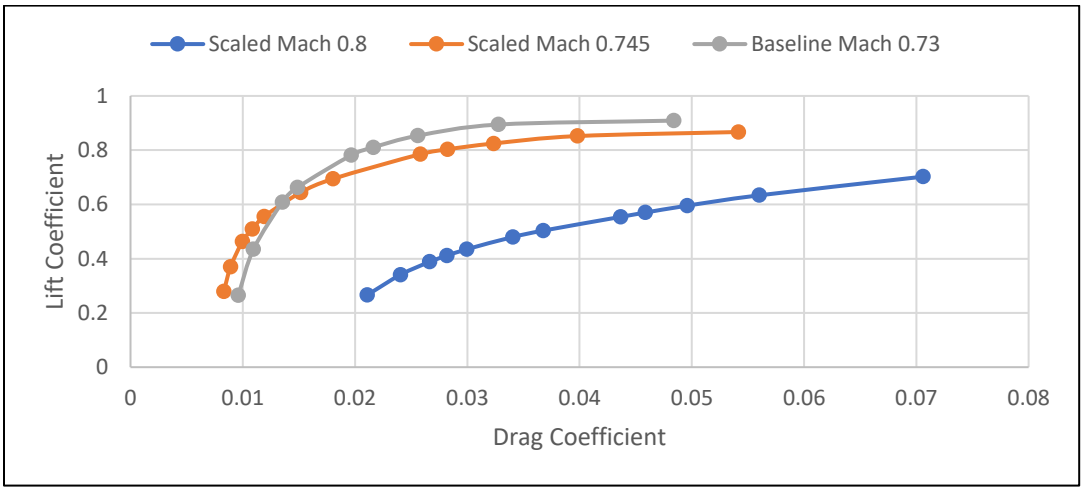

Figure 6.18 Scaled RAE 2822 airfoil variation in lift and drag coefficients

6.3.4 Conclusions

The scaled RAE2822 airfoil at 35,000 ft and a cruise Mach number of 0.745 is able to achieve a comparable lift to drag ratio to the smaller AGARD case 9 model. An increase in cruise speed to the higher Mach number of 0.8 utilized for the Sugar IV results in decreased performance for the RAE2822 airfoil due to an increase in wave drag. In order to improve the performance of the scaled airfoil, the scaled CFJ airfoil must achieve a lift-to-drag ratio of at least 47.

6.4 Scaled Co-Flow Jet

6.4.1 Physical Model

After establishing a baseline for the scaled RAE2822 airfoil at the 35,000 ft altitude cruise conditions, the CFJ is implemented into the crank chord scaled airfoil. Based on the optimization results of Zha et al. [7], the width of the suction slot width is increased to 1.2% of the chord length and the suction slot location is shifted to 75% of the chord length to reduce the chance of choking the suction slot. If the shock location shifts too far downstream close to the suction slot, it can become choked leading to a reduction in aerodynamic performance and energy efficiency. Current simulations methods also reflect a reduction in convergence when the injection slot becomes choked due to the presence of high Mach numbers over the speed of sound near the outlet boundary condition. Additionally, the suction surface translation is set to 0.1% in order to improve the performance of the CFJ for the RAE2822 airfoil by reducing wave drag [7].

6.4.2 Numerical Method

A parametric study is run sweeping through a range of mass flow conditions for the injection inlet and suction outlet. This sweep is performed at the cruise Mach speed for the Sugar IV and Sugar III, 0.8 and 0.745 respectively. Both freestream velocities are simulated at an angle of attack of 2.31°. The Mach 0.745 case is also run at a lower angle of attack of 1.5 to evaluate the CFJ performance for a weaker shock condition. With the exception of the slot inlet and outlet boundary conditions, all other numerical methods are consistent with those described in subsection 6.3.2. The grid for the scaled CFJ is shown in Figure 6.19.

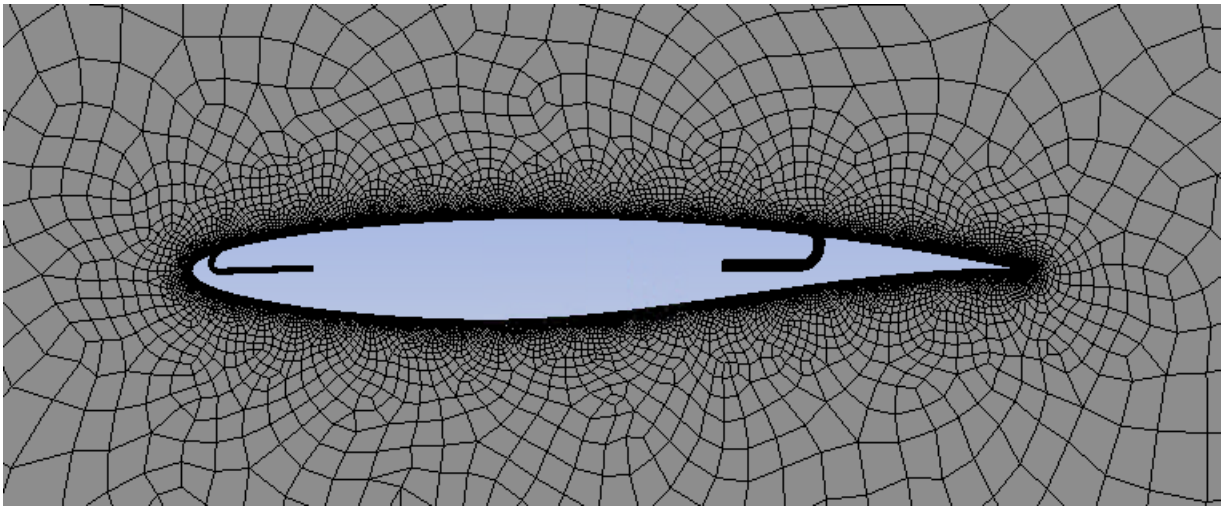

Figure 6.19 Unstructured grid around the scaled CFJ-RAE 2822 airfoil

6.4.3 Results and Discussion

Results for the Mach 0.8 runs at the higher 2.31 angle of attack are only shown for lower momentum coefficients. This is because at higher momentum coefficients the suction slot becomes choked as a result of the shock shifting downstream towards the trailing edge. This is not the case for the lower Mach number cases. For the scaled airfoil, CFJ improved the lift for all three cases as shown in Fig. 6.20. Second, for the smaller angle of attack CFJ produces thrust while maintaining a weak shock wave. This is reflected in decreasing drag as the momentum coefficient increases in Fig. 6.21. It can be seen from Fig. 6.23 that CFJ has the potential to significantly increase the aerodynamic performance of an airfoil for a transonic truss-braced wing at a low angle of attack.

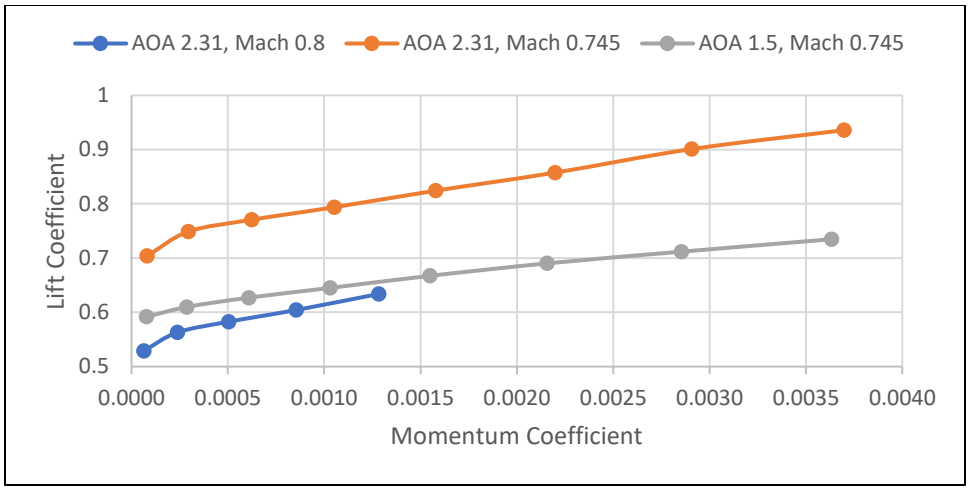

Figure 6.20 Scaled CFJ-RAE 2822 lift coefficient variation with momentum coefficient

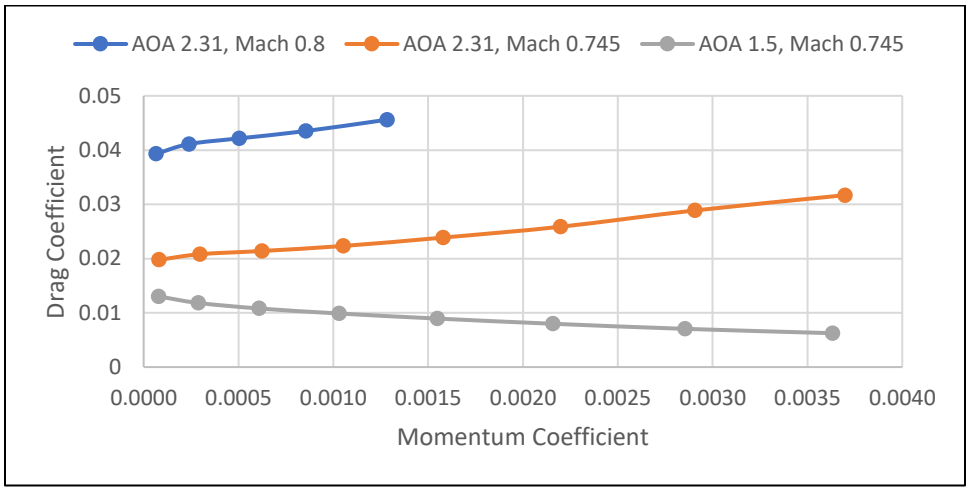

Figure 6.21 Scaled CFJ-RAE 2822 drag coefficient variation with momentum coefficient.

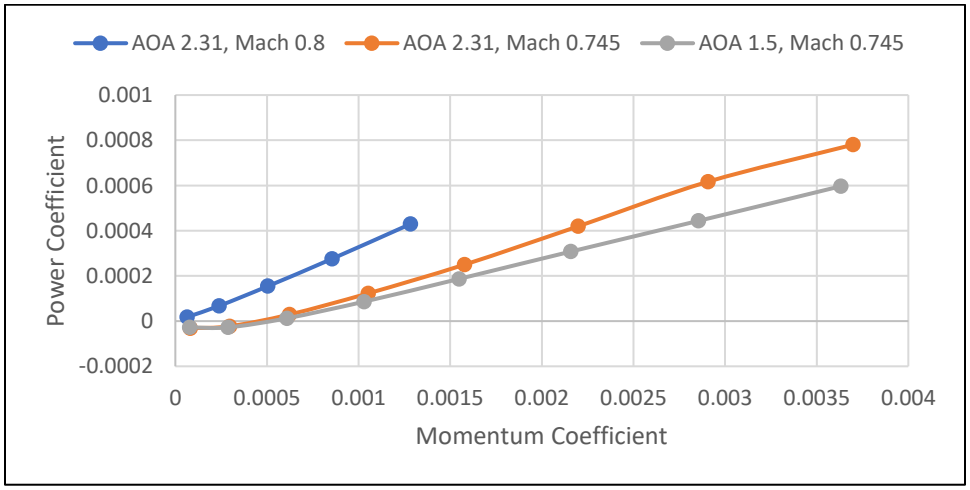

Figure 6.22 Scaled CFJ-RAE 2822 power coefficient variation with momentum coefficient

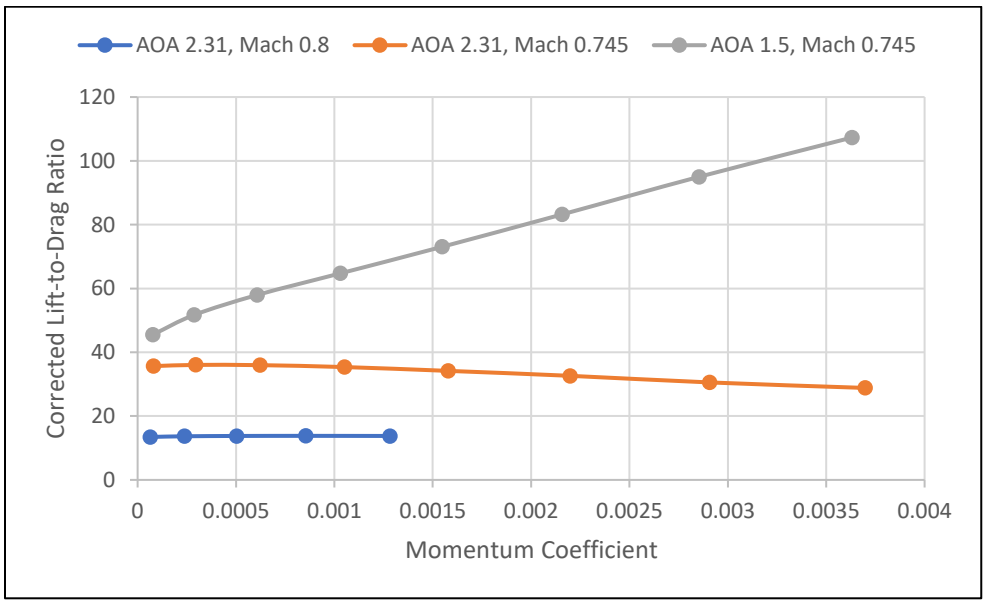

Figure 6.23 Scaled CFJ-RAE 2822 corrected lift to drag ratio variation with momentum coefficient.

6.3.4 Conclusions

Numerical methods and boundary conditions were validated through comparison to published RAE2822 airfoil data both with and without co-flow jets. The increase in airfoil size for usage in a TTBW as well as variation in Mach number affects the shock formation on the suction surface of the airfoil. The scaled airfoil with CFJ shows improvement in the corrected lift-to-drag ratio for the 1.5° angle of attack case at Mach 0.745. Optimization of the co-flow jet geometry for the scaled airfoil has the potential to further improve the aerodynamic and energy efficiency for implementation into a 3D TTBW.

6.5 CFJ-TTBW 3D

6.5.1 Physical Model

The baseline and scaled RAE 2822 airfoils both with and without CFJ were simulated in 2D in order to test the initial viability for the CFJ to be implemented into a 3D TTBW. After completing

validation of the RAE2822 airfoil with and without the addition of co-flow jets in two-dimensions, a three-dimensional model of a transonic truss brace wing based on the SUGAR IV planform was created using the RAE2822 airfoil. A full 3D model of a TTBW based on the Sugar IV is modeled using Solidworks. Although the model has a similar planform to the Sugar IV, the cross-sections are different as a result of using the RAE 2822 airfoil. Two models were created to establish a benchmark and evaluate the effect of the truss on the main wing. The first model is the main high mounted wing without a supporting truss, and the second is with the addition of the truss. The root of the truss has a greater thickness as required in order to house the aircraft landing gear. The two wing models without CFJ are simulated at Mach 0.745 and Mach 0.8 with external conditions matching those of a 35,000 ft altitude cruise at angles of attack ranging from 0 to 5 degrees.

The CFJ-TTBW geometry with the addition of the spanwise injection and suction slots is shown in Fig. 6.24. The slot geometry parameters (width, length and angle) were kept consistent with the scaled CFJ two-dimension test case with the exception of the shear suction translation. The shear suction translation was removed in order to simplify the 3D geometry for meshing and simulation. The slot length is set such that the slot does not overlap with the wing tip fold required for airport gateway clearance. Although the chord of the wing varies from the root to the crank, the slot geometry is curved to maintain the percentage distance from the leading and trailing edges of the wing. The final model adds in the LH2-767 fuselage as shown in Fig. 6.25. CFD- RANS simulation was performed on a LH2-767 fuselage with TTBW and CFJ. The mesh complexity was reduced by removing the tail since the main focus is the interaction of the wing and the fuselage.

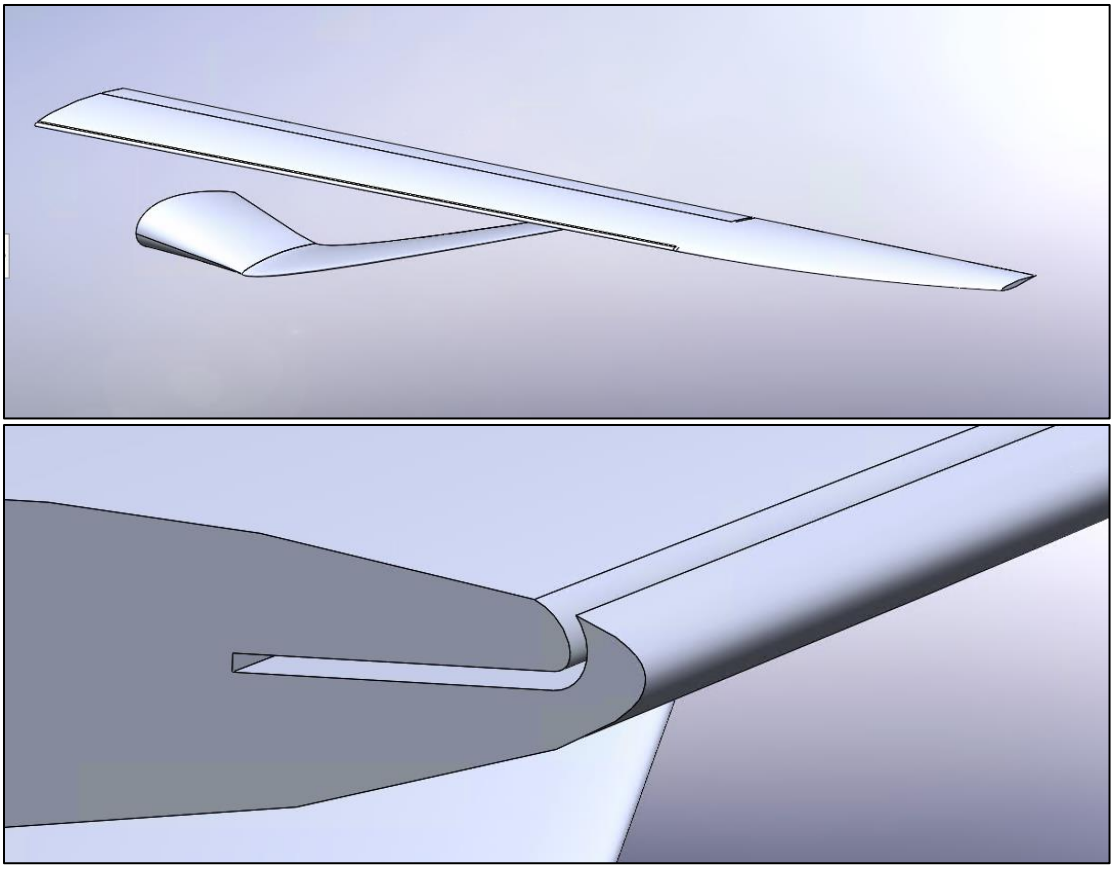

Figure 6.24 Close up of the transonic truss-braced wing with co-flow jet geometry and injection slot

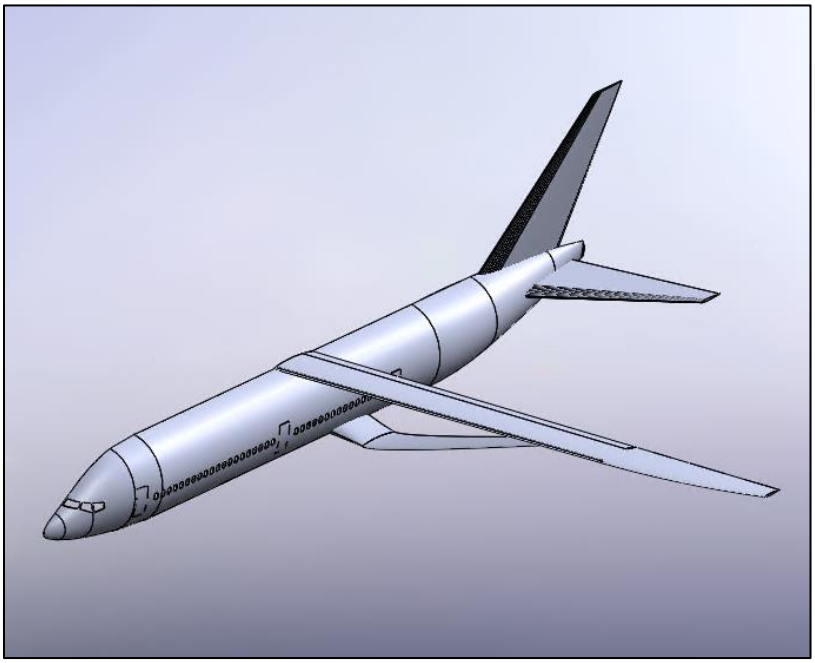

Figure 6.25 LH2-767 CFJ-TTBW aircraft model geometry

6.5.2 Numerical Methods

Unstructured tetrahedral meshes were used for all of the 3D simulations in order to reduce the mesh time requirement. A hemispherical domain was implemented around the models to create a fluid domain. Numerical methods were kept consistent with the 2D validation cases. The grid for the high wing is show in Fig. 6.26 utilizing ~9.4 million elements. The grid for the baseline TTBW is shown in Fig. 6.27 utilizing ~12 million elements to model the more complex geometry. The full aircraft model mesh is shown in Fig. 6.28 with ~25 million elements. Preliminary results are included for the full aircraft model; however, additional grid independence studies are necessary for further analysis.

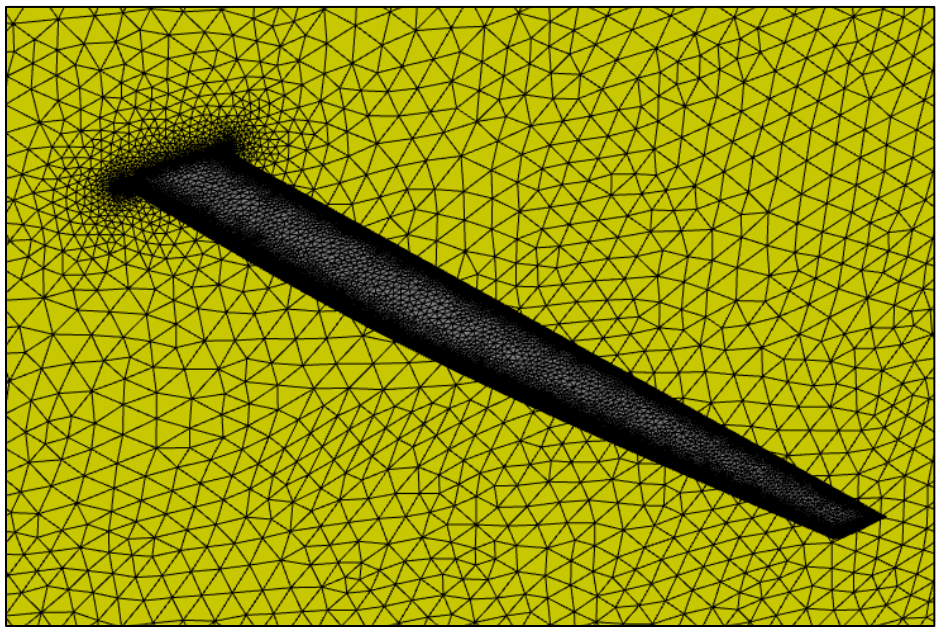

Figure 6.26 Unstructured grid around the high wing configuration

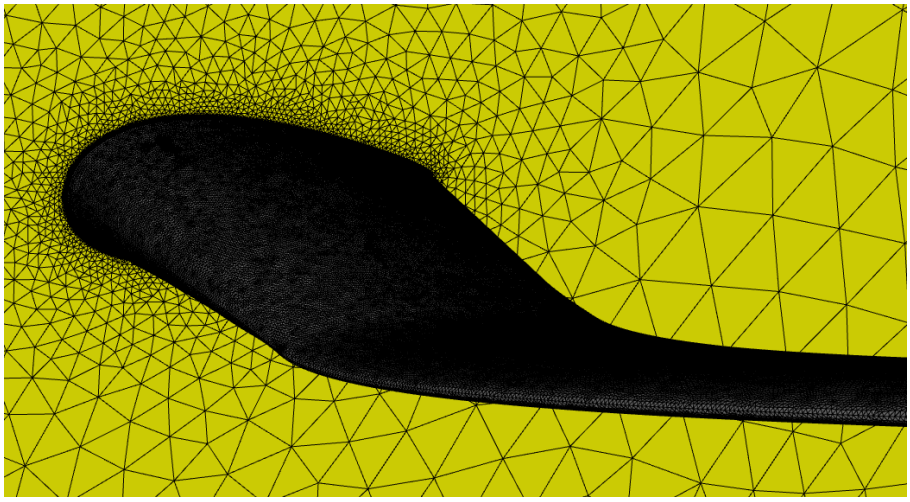

Figure 6.27 Close up view of the unstructured mesh around of the TTBW

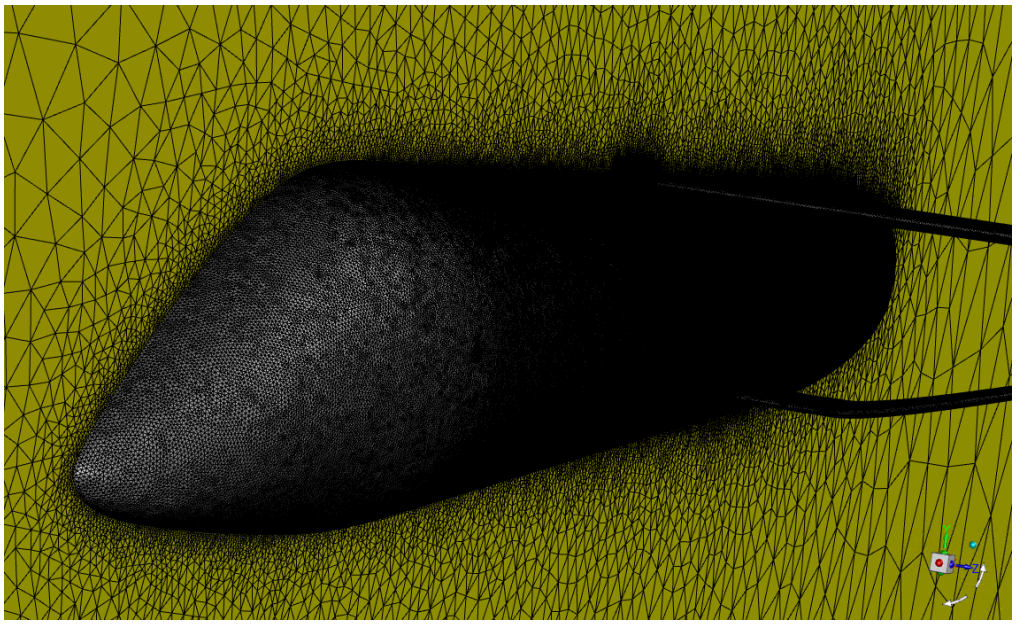

Figure 6.28 Unstructured grid around the LH2-767 CFJ-TTBW aircraft model

6.5.3 Results and Discussion

Figure 6.29 shows the lift to drag ratio for the high wing and transonic truss-braced wing configurations simulated at Mach 0.8 and 0. 745.The high wing configuration without the truss achieves the best lift-to-drag ratio but is not structurally feasible for the target design span. It can be seen that the truss has a significant effect on the lift to drag ratio of the transonic truss braced

wing. Further optimization of the truss as an aerodynamic component in conjunction with the main wing is needed to improve the overall performance of the RAE 2822 TTBW.

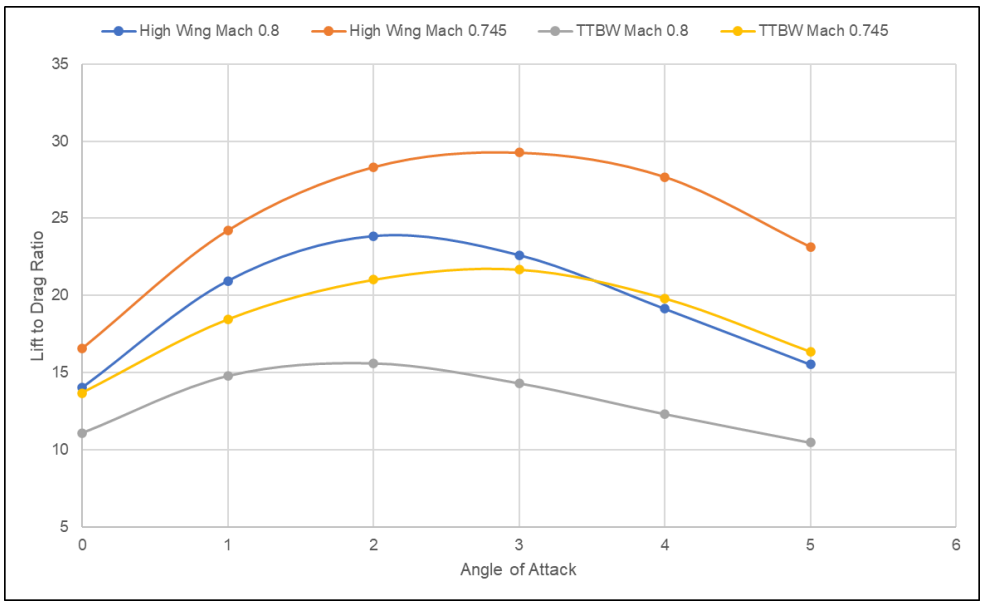

Figure 6.29 Lift-to-drag ratio of the RAE 2822-TTBW with and without the truss

The TTBW at a cruise speed of Mach 0.745 is chosen as the case to implement the co-flow jets. The simulations were run at an angle of attack of 1.5 degrees in order to achieve the better performance using the CFJ. The lift-to-drag ratio for the CFJ-TTBW with respect to the CFJ momentum coefficient is shown in Fig. 6.30. It can be noted that the lift-to-drag ratio steadily increases for the tested range of momentum coefficients. This curve is compared to the lift-to-drag ratio with respect to the angle of attack for the TTBW without CFJ. At the higher momentum coefficients, the CFJ-TTBW achieves a higher lift-to-drag ratio than any of the baseline RAE2822 TTBW simulations. The RAE 2822 TTBW achieves a lift to drag ratio of 21.68 but with the addition of CFJ, this is increased to 26.76. This shows that CFJ can increase the aerodynamic efficiency of a TTBW. Since the CFJ has improved performance at lower angles of attack, further studies are needed to optimize the angle of attack and momentum coefficient necessary to generate sufficient lift. There is a tradeoff since lowering the angle of attack reduces lift but also reduces

drag and allows the CFJ to improve lift and reduce drag further. The energy expenditure for the CFJ-TTBW is shown in Fig. 6.31. Although the system requires a large number of kilowatts, reaching over 60kW for the highest momentum coefficient case, to achieve benefits during cruise, this is not out of the range of modern integrated drive generators and is well within the range of the total electrical power of modern airliners.

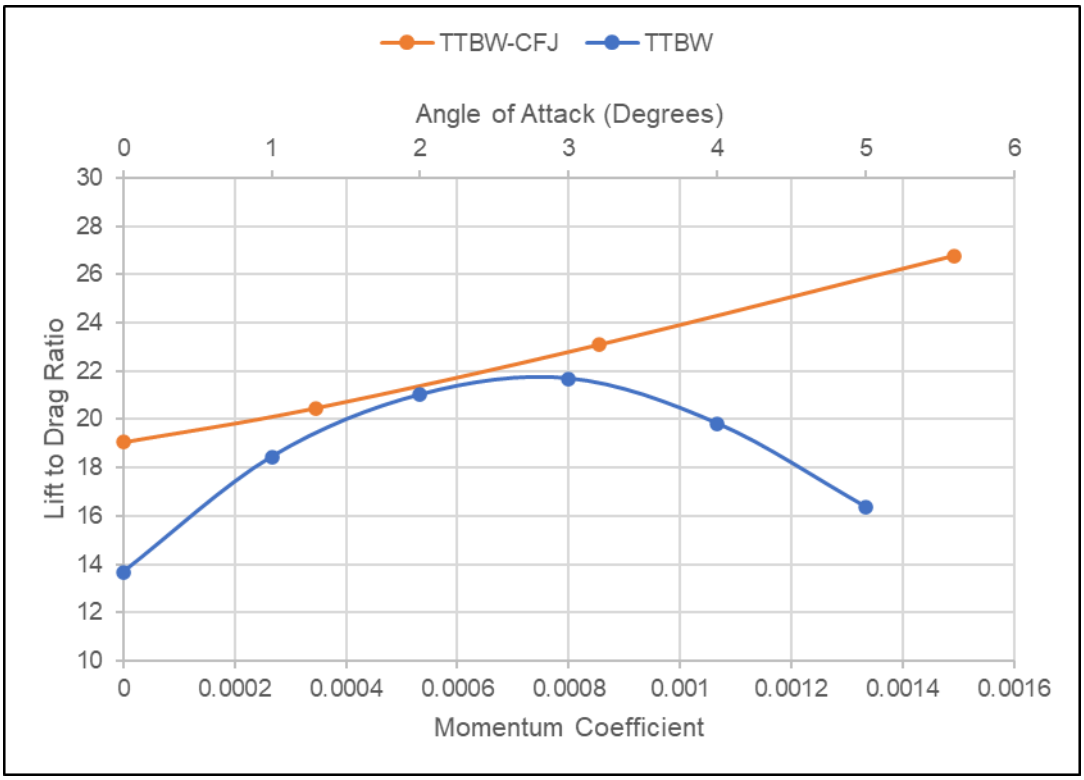

Figure 6.30 Performance comparison of the TTBW with and without CFJ

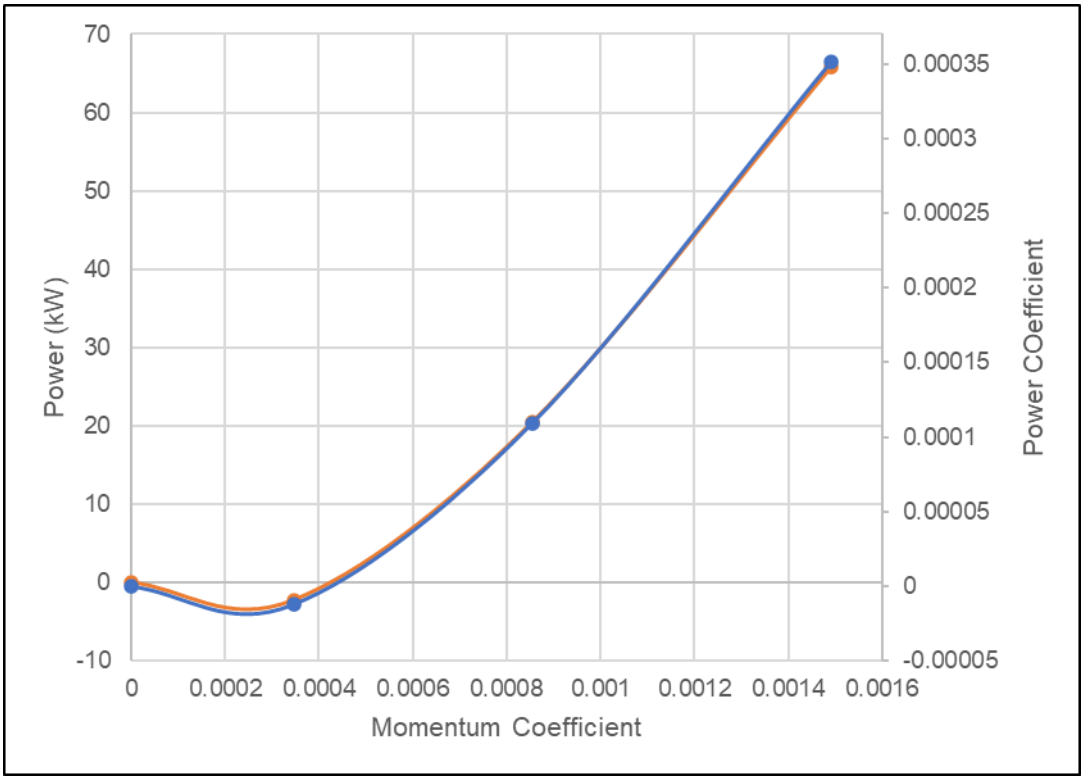

Figure 6.31 Energy expenditure for the CFJ-TTBW

The pressure contours are shown in Fig. 6.32 for the LH2-767 with TTBW and CFJ using the preliminary coarse mesh. This shows the potential of the CFJ-TTBW to be integrated into the full airliner configurations for future research and optimization.

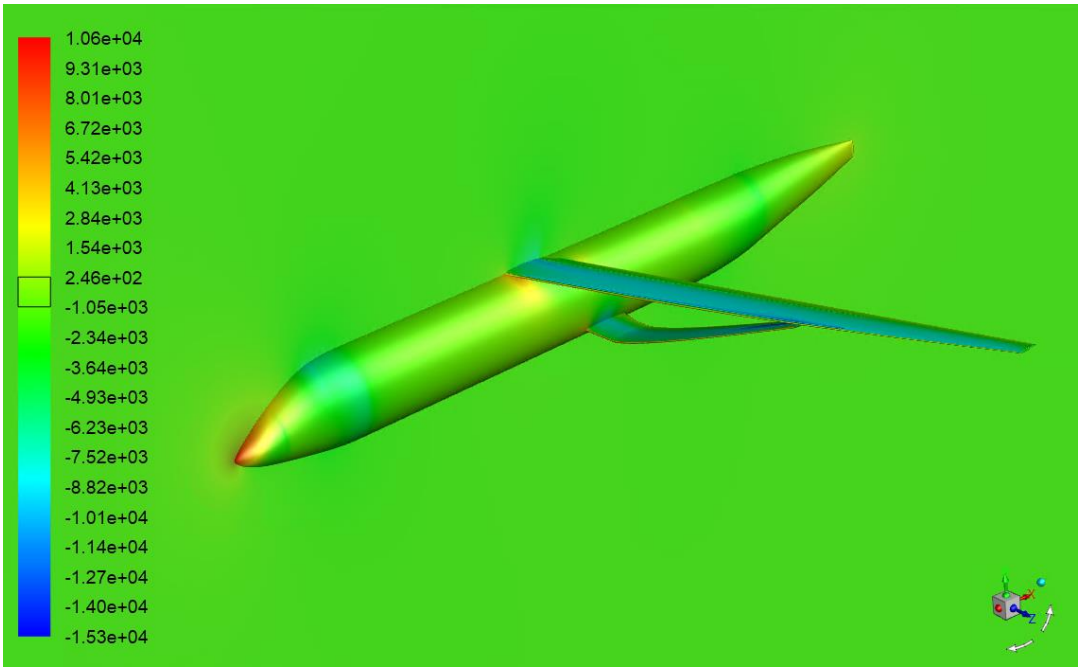

Figure 6.32 Pressure contours on LH2-767 CFJ-TTBW using CFD RANS with SA model

6.5.4 Conclusions

Four 3D configuration were simulated to evaluate the potential of co-flow jets to improve the performance of a transonic truss braced wing. Overall, the truss required to support the high span of the TTBW reduced the lift-to-drag ratio. The transonic truss-braced wing model at a cruise speed of Mach 0.745 was chosen to implement the CFJ since it achieved the best baseline lift-to-drag ratio while maintaining structural requirements. The implementation of CFJ improves the lift-to-drag ratio of the wing and truss assembly from 21.68 to 26.76. Additionally, the amount of power required to achieve the aerodynamic improvements using the co-flow jet is reasonable based on the power available onboard of modern airliners.

Chapter 7: Summary and Future Work

7.1 Summary

The progression of a sustainable transonic truss-braced wing aircraft using liquid hydrogen fuel and active flow control is achieved through the implementation of a variety of computational tools. It is shown that a transonic truss braced wing configuration with internal fuel tanks has the potential to reduce emissions and improve aerodynamic performance in comparison to traditional cantilever wing and external fuel tanks. Numerical methods are validated through the testing of the turbulence models on a variety of geometries in both 2D and 3D and comparing the calculations with the wind tunnel data and published simulation results. The ability of the turbulence models to calculate complex 3D flows with separation and shock waves is evaluated through simulations of the NASA Wing-body juncture flow and ONERA M6 wing model respectively. Numerical methods and boundary conditions for the implementation of co-flow jets are validated in 2D before scaling the RAE 2822 airfoil with and without CFJ to the crank chord of the SUGAR IV TTBW. Lastly it is shown that the implementation of CFJ technology into TTBW airliners has the potential to further improve the aerodynamic performance. At low angles of attack, the CFJ significantly improved the lift-to-drag ratio of the RAE 2822 TTBW cruising at an altitude of 35,000 ft. at Mach 0.745.

7.2 Future Work

7.2.1 Liquid Hydrogen

The development of liquid hydrogen technologies is crucial to reduce the environmental impact of the aviation sector. The materials and structures of the liquid hydrogen tanks along with the cryogenic system require significant research and testing for usage in commercial aircraft. Liquid

hydrogen storage inside of fuselage has many implications for both the aircraft structure and safety. Bulkheads are necessary to separate the passengers from the liquid hydrogen. A system will need to be designed in order to detect any possible leaks in the hydrogen fuel tanks and fuel lines along with a system to vent the dangerous fumes outboard and away from the passengers. Additionally, the complex fuel lines are necessary to deliver the liquid hydrogen from the internal tanks to the wing mounted engines. This will require further flow analysis along with complex routing throughout the fuselage. The inclusion of internal tanks requires further aerodynamic optimization of the fuselage with a consideration of the tank placement in order to minimize the drag after increasing the fuel volume relative to traditional Jet A. Although there are many challenges to the implementation of liquid hydrogen, it is a viable fuel source that has potential to drastically reduce the emission caused by the commercial aviation sector.

7.2.2 CFJ-TTBW

This work has demonstrated the viability of the co-flow jet to improve the performance of a transonic truss-braced wing. This opens up a large design space for future research and wing development. The implementation of CFJ into other supercritical airfoils would provide further insight into optimization considerations and the effect of airfoil shape on CFJ performance. Even further, the development of the new airfoils in tangent with CFJ slot parameters (location, width and angle) designed specifically for commercial cruise conditions has the potential to yield even high aerodynamic performance. Along with this, the planform optimization of the 3D truss braced wing with CFJ is necessary to analyze the effect of taper, dihedral and twist on the performance of the co-flow jets. Current research treats the injection and suction slots as one continuous slot implementing a constant momentum coefficient. Future research could focus on breaking up this boundary condition and optimizing the momentum coefficient for each section of the wing. This

work focused on the cruise condition since improving the performance at cruise has the largest impact on emissions reduction. Future work is also needed to test the CFJ-TTBW during the other segments of flight including takeoff, climb descent and landing. The CFJ could potentially be used to reduce the need for high lift surfaces required during takeoff. In order to implement CFJ on larger aircraft, further research will be required to analyze the structural implications on the wing. Future development of the LH2 767 with CFJ-TTBW could also focus on the implementation of open rotor turbofans that would further reduce the fuel burn.

References

[1] Lee, D. S., Fahey, D. W., Skowron, A., Allen, M. R., Burkhardt, U., Chen, Q., and Gettelman, A., "The Contribution of Global Aviation to Anthropogenic Climate Forcing for 2000 to 2018," Atmospheric Environment, 117834, 2020.

[2] IPCC, 2018: Summary for Policymakers - "Global Warming of 1.5 Deg. C: An IPCC Special Report on the Impacts of Global Warming of 1.5 Deg. C above Pre-Industrial Levels and Related Global Greenhouse Gas Emission Pathways, in the Context of Strengthening the Global Response to the Threat of Climate Change, Sustainable Development and Efforts to Eradicate Poverty"

[3] "737 Airplane Characteristics for Airport Planning D6-58325-6 Rev C." Boeing Commercial Airplanes, Oct. 2021.

[4] Droney, C. K., Harrison, N. A., and Gatlin, G. M., "Subsonic Ultra-Green Aircraft Research: Transonic Truss-Braced Wing Technical Maturation" Available: https://www.icas.org/ICAS_ARCHIVE/ICAS2018/data/papers/ICAS2018_0597_paper.pdf.

[5] N. A. Harrison, M. D. Beyar, E. D. Dickey, K. Hoffman, G. M. Gatlin, and S. A. Vike, "Development of an efficient Mach = 0.80 Transonic Truss-Braced Wing Aircraft." (Online available:https://www.aiaa.org/docs/default-source/default-document-library/publications/developmentofanefficientmach080transonictruss-bracedwingaircraft.pdf.[accessed: 31-May-2022].

[6] L. P. Melton and C. S. Yao. Active Control of Separation from the Flap of a Supercritical Airfoil. AIAA Journal, 44:34–41, 2006.

[7] Liu, Z., and Zha, G.-C., "Transonic Airfoil Performance Enhancement Using Co-Flow Jet Active Flow Control - AIAA aviation forum" Available: https://arc.aiaa.org/doi/10.2514/6.2016-3472.

[8] "Ultra-high efficiency Coflow jet airfoil and the transformative aircraft" Available: http://coflowjet.com/wp-content/uploads/2018/02/CFJ__Slides_Feb2018b.pdf.

[9] Ren, Y., and Zha, G.-C., "Design of injection jet span profile for co-flow jet airfoil" Available: https://acfdlab.miami.edu/publications/aiaa-2019-0589.pdf.

[10] Menter, F. R., "Two-Equation Eddy-Viscosity Turbulence Models for Engineering Applications", AIAA Journal, Vol. 32, No. 8, 1994, pp. 1598-1605. https://doi.org/10.2514/3.12149.

[11] "NASA Langley Research Center Turbulence Modeling Resource," http://turbmodels.larc.nasa.gov [retrieved October 2018]

[12] Spalart, P. and Allmaras. S., "A One-Equation Turbulence Model for Aerodynamic Flows," AIAA Paper 1992-439, 30th Aerospace Sciences Meeting and Exhibit, Reno, NV, 1992, https://doi.org/10.2514/6.1992-439.

[13] Han, X., Rahman, M. M., and Agarwal, R. K., "Development and Application of a Wall Distance Free Wray-Agarwal Turbulence Model," Paper No. 2018-0593, AIAA SciTech Forum, Kissimmee, FL, 8-12 January 2018.

[14] Spalart, P. R., "Strategies for Turbulence Modelling and Simulation," International Journal of Heat and Fluid Flow, Vol. 21, 2000, pp. 252-263.

[15] Hoerner, S. F., *Fluid-dynamic drag: Practical Information on Aerodynamic Drag and Hydrodynamic Resistance*. Bakersfield, CA: Hoerner Fluid Dynamics, 1992.

[16] Landweber, L. and Gertler, M., *Mathematical Formulation of Bodies of Revolution*, Washington: Navy Dept., David W. Taylor Model Basin, 1950.

[17] Raymer, D. P., *Aircraft Design: A Conceptual Approach*, Sixth Edition, American Institute of Aeronautics and Astronautics, Reston VA, Copyright 2018 by Daniel Raymer.

[18] Roskam, J., *Aircraft Design, Part 5 - Component Weight Estimation*, DAR Corporation, Lawrence, KS, Copyright 1982 by Jan Roskam.

[19] Torenbeek, E., *Advanced Aircraft Design - Conceptual Design, Analysis and Optimization of Subsonic Civil Airplanes*, John Wiley & Sons, West Sussex, United Kingdom, Copyright 2013 by Egbert Torenbeek.

[20] Wells, D., Horvath, B., and McCullers, L., "The Flight Optimization System Weights Estimation Method," NASA Langley Research Center.

[21] Bradley, M. and Droney, C., "Subsonic Ultra Green Aircraft Research: Phase I Final Report," NASA CR2011-216847, 2011.

[22] Kegerise, M. A., Neuhart, D.H., Hannon, J.A., and Rumsey, C. L., "An Experimental Investigation of a Wing-Fuselage Junction Model in the NASA Langley 14- by 22-Foot Subsonic Wind Tunnel, " AIAA Paper 2019-0077, AIAA SciTech Forum, San Diego, CA, 7-11 January 2019.

[23] Rumsey, C. L., Carlson, J.-R., and Ahmad, N., "FUN3D Juncture Flow Computations Compared with Experimental Data," AIAA Paper 2019-0079, AIAA SciTech Forum, San Diego, CA, 7-11 January 2019, doi: https://doi.org/10.2514/6.2019-0079

[24] Lee, H. C. and Pulliam, T. H., "Overflow Juncture Flow Computations Compared with Experimental Data," AIAA Paper 2019-0080, AIAA SciTech Forum, San Diego, CA, 7-11 January 2019, doi: https://doi.org/10.2514/6.2019-0080.

[25] Nagapetyan, H. J., "Development and Application of Quadratic Constitutive Relation and Transitional Crossflow Effects in the Wray-Agarwal Turbulence model," Washington University in St. Louis Open Scholarship Report, Aug. 2018.

[26]

[27] Abe, H., Mizobuchi, Y., and Matsuo, Y., "Effect of a Quadratic Constitutive Relation on Juncture Flow Computations," AIAA 2020-2752, AIAA Aviation 2020 Forum, 2020, doi.org/10.2514/6.2020-2752.

[28] Fluent Documentation available at https://www.sharcnet.ca/Software/Ansys/17.0/en-us/help/ai_sinfo/flu_intro.html.

[29] "NASA Langley Research Center Turbulence Modeling Resource," http://turbmodels.larc.nasa.gov [retrieved October 2018]

[30]

[31] Wood, S., Rumsey, C., and Ahmad, N., "High-Fidelity CFD Workshop 2021: RANS SA-[neg]-QCR2000 Juncture Flow Model Case," available at https://turbmodels.larc.nasa.gov/Highfidelitycfd2021/SAnegQCR2000_juncture_flow_HW_2021.pdf.

[32] Rumsey, C. L., Ahmad, N. N., Carlson, J.-R., Kegerise, M. A., Neuhart, D., Hannon, J., Jenkins, L. N., Yao, C.-S., Balakumar, P., Gildersleeve, S., Bartram, S., Pulliam, T. H., Olsen, M. E., and Spalart, P., "CFD Comparisons with Updated NASA Juncture Flow Data," AIAA SciTech 2021 Forum, 2021.

[33] Destarac, D. and Dumont, A., "ONERA M6 Wing Test-Case, Original and TMR," Sep. 2016.

[34] Vatas, V.N., "Accurate Numerical Solutions for Transonic Viscous Flow over Finite Wings", Journal of Aircraft, Vol. 24, No. 6, June 1987, pp. 377-385.

[35] Abid, R., Vatsa, V. N., Johnson, D. A., and Wedan, B.W., "Prediction of Sepatared Transonic Wing Flows with a Non-Equilibrium Algebraic Model", AIAA Paper 89-0558, AIAA 27th Aerospace Sciences Meeting, Reno, NV, January 9-12, 1989.

[36] Radespiel, R., Rossow, C., and Swanson, R.C., "An Efficient Cell-Vertex Multigrid Scheme for the Three-Dimensional Navier-Stokes Equations," AIAA Paper 89-1953, AIAA 9th Computational Fluid Dynamics Conference, Buffalo, NY, June 14-16, 1989.

[37] Rumsey, C. L. and Vatsa, V.N., "Comparison of the Predictive Capabilities of Several Turbulence Models", Viscous Flow over Finite Wings," Journal of Aircraft, Vol. 32, No. 3, May-June 1995, pp. 510 -514.

[38] "3D ONERA M6 Wing Validation for Turbulence Model Numerical Analysis," NASA Langley Research Center Turbulence Model Resource website https://turbmodels.larc.nasa.gov/onerawingnumerics_val.html. (Retrieved 23 June 2020)

[39] Schmitt, V. and Charpin, F., “Pressure Distributions on the ONERA-M6-Wing at Transonic Mach Numbers,” Experimental Data Base for Computer Program Assessment, AGARD Advisory Report AR-138, May 1979.

[40] “3D ONERA M6 Wing Validation for Turbulence Model Numerical Analysis - SA-neg Model Results,” NASA Langley Research Center Turbulence Model Resource website https://turbmodels.larc.nasa.gov/onerawingnumerics_val_sa.html.

[41] Spalart, P. and Allmaras. S., "A One-Equation Turbulence Model for Aerodynamic Flows,"AIAA Paper 1992-439, 30th Aerospace Sciences Meeting and Exhibit, Reno, NV, 1992, https://doi.org/10.2514/6.1992-439.

[42] “AGARD-AR-138,” *Abbott Aerospace Canada Ltd* Available: https://www.abbottaerospace.com/downloads/agard-r-138/.

[43] CD-dapco. Validation of STAR-CCM+ for External Aerodynamics in the Aerospace Industry

[44] H. Namgoong. AIRFOIL OPTIMIZATION FOR MORPHING AIRCRAFT. PhD Thesis, Purdue University, 2005.

[45] “Adjoint shape optimization for Aerospace Webinar (2021)” Available: https://www.nas.nasa.gov/assets/pdf/ams/2021/AMS_20210408_Kelecy.pdf.

[46] June, J. C., Thomas, R. H., and Guo, Y., “NASA Technical Reports Server (NTRS)” Available: https://ntrs.nasa.gov/api/citations/20220008607/downloads/AIAA%202022%20TTBW%20Presentation%2006%2008.pdf.